EFFECTS OF DISTRIBUTIONS OF ENERGY OF TRANSFER RATES ON SPECTRAL HOLE BURNING IN PHOTOSYNTHETIC PIGMENT-PROTEIN COMPLEXES

SOMAYA AHMOUDA

A THESIS

IN

THE DEPARTMENT

OF

PHYSICS

PRESENTED IN PARTIAL FULFILLMENT OF THE REQUIREMENTS
FOR THE DEGREE OF MASTER OF SCIENCE (PHYSICS) AT
CONCORDIA UNIVERSITY
MONTREAL, QUEBEC, CANADA

AUGUST 2010

Your file Votre référence
ISBN: 978-0-494-71090-6
Our file Notre référence
ISBN: 978-0-494-71090-6

ABSTRACT

SOMAYA AHMOUDA

EFFECTS OF THE DISTRIBUTIONS OF ENERGY TRANSFER RATES ON SPECTRAL HOLE BURNING IN PHOTOSYNTHETIC PIGMENT-PROTEIN COMPLEXES

To perform photosynthesis, plants, algae and bacteria possess well organized and closely coupled photosynthetic pigment-protein complexes. Information on energy transfer in photosynthetic complexes is important to understand their functioning and possibly to design new and improved photovoltaic devices. The information on energy transfer processes contained in the narrow zero-phonon lines at low temperatures is hidden under the inhomogeneous broadening. Thus, it has been proven difficult to analyze the spectroscopic properties of these complexes in sufficient detail by conventional spectroscopy methods. In this context the high resolution spectroscopy techniques such as Spectral Hole Burning are powerful tools designed to get around the inhomogeneous broadening. Spectral Hole Burning involves selective excitation by a laser which removes molecules with the zero-phonon transitions resonant with this laser. This thesis focuses on the effects of the distributions of the energy transfer rates (homogeneous line widths) on the evolution of spectral holes. These distributions are a consequence of the static disorder in the photosynthetic pigment-protein complexes. The qualitative effects of different types of the line width distributions on the evolution of spectral holes have been and explored by numerical simulations, an example of analysis of the original experimental data has been presented as well.

ACKNOWLEDGMENTS

Special thank to my mother, Gurfa, and father, Ahsain, for their great help and encouragement. Also, I would like to thank my brothers and sisters for their continued support. I would like to especially thank my husband, Giuma, for his continuous support and understanding.

First and foremost, I would like to sincerely thank my supervisor Dr. Valter Zazubovits for his guidance, help and support during the course of my thesis research. He is the person with whom you like to work, not only because he possesses the distinguished scientific talent and knowledge, but also because he has highly respectable virtue.

I must acknowledge to Libyan Education program for the financial support during the completion of my Master Degree.

Finally, I would like to thank the Canada Foundation for Innovation and NSERC for their financial support.

TABLE OF CONTENTS

LIST OF FIGURES

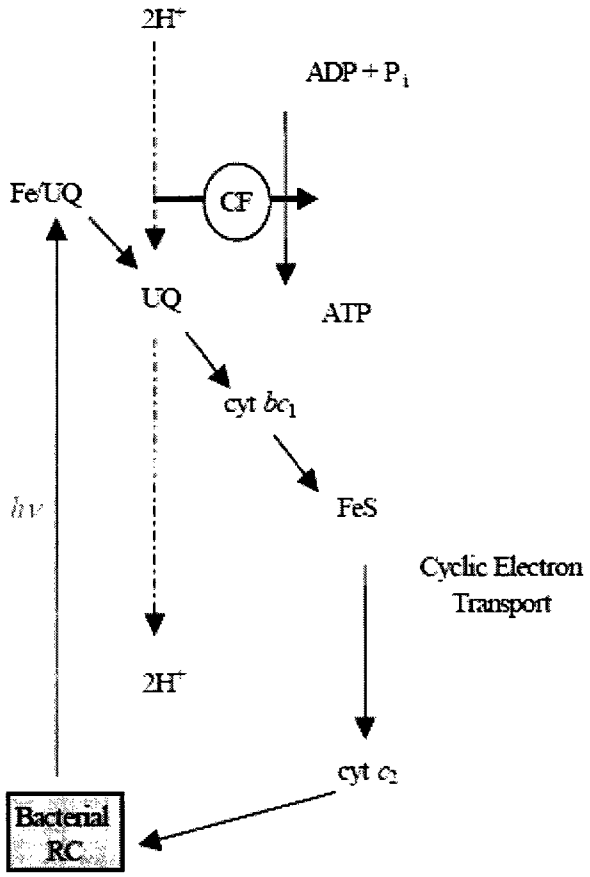

Figure 1.1. Schematic of cyclic phosphorylation in purple bacteria . After the bacterial RC is excited by light (hν), primary electron transfer to an iron-ubiquinone complex (Fe/UQ) occurs. The electron leaves the RC through transfer to a ubiquinone (UQ) and travels to cyctochromes bc_1 (cyt bc_1), to cytochromes c_2 (cyt c_2), and finally back to reduce the RC, completing the electron transfer cycle. In the meantime, the electron transfer across the bacterial membrane through UQ creates a proton gradient driving ATP synthesis. From [5]

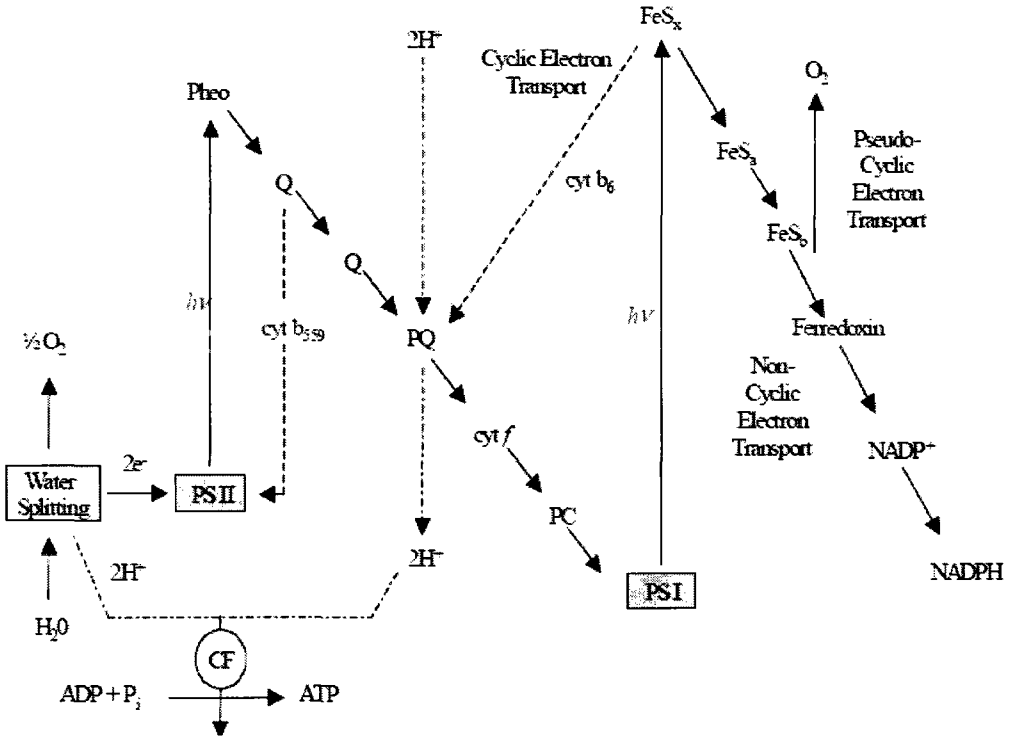

Figure 1.2. Schematic of non-cyclic phosphorylation in cyanobacteria and plants. Primary electron transfer to pheophytin (Pheo) occurs when the PS II RC is excited by light (hv) and the electron is then passed down to quinones (Q), a plastiquinone (PQ), cytochrome f (cyt f), and to plastocyanin (PC). After excitation, the Photosystem I (PS I) RC transfers an electron to a series of iron-sulfur complexes (FeS_x, FeS_a, FeS_b) and PS I is reduced by PC. This is followed by a reduction of FeS_b by NADP reductase (NADP+), which leads to the synthesis of NADPH and is used in the Calvin cycle. H_2O (generating O_2) and cytochrome b559 (cyt b559) reduces the PS II RC. Electron transfer across the thylakoid membrane creates a proton gradient, which drives ATP synthesis. If the organism is too low in NADPH to synthesize sugars, cyclic phosphorylation takes place. Then electron transfer from FeS_x to cytochrome b_6 (cyt b_6) takes place, ensuring that the PS I RC is reduced. From [5]

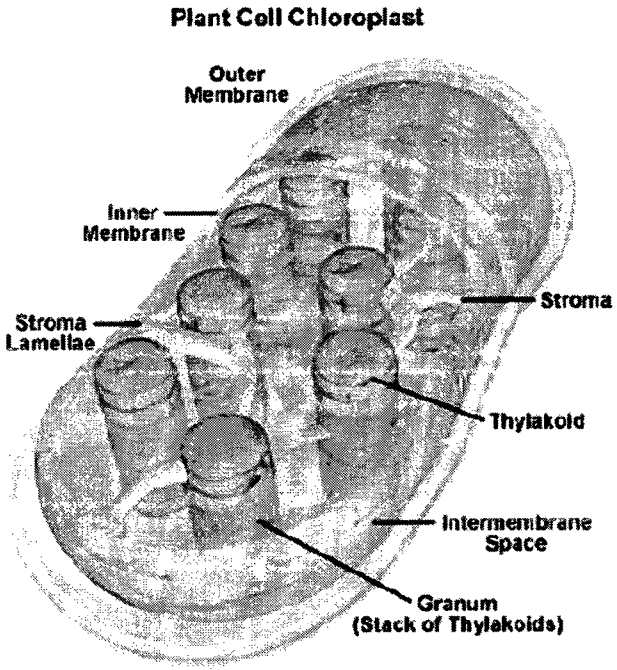

Figure 1.3: The structure of a chloroplast. From http:// micro.magnet.fsu.edu

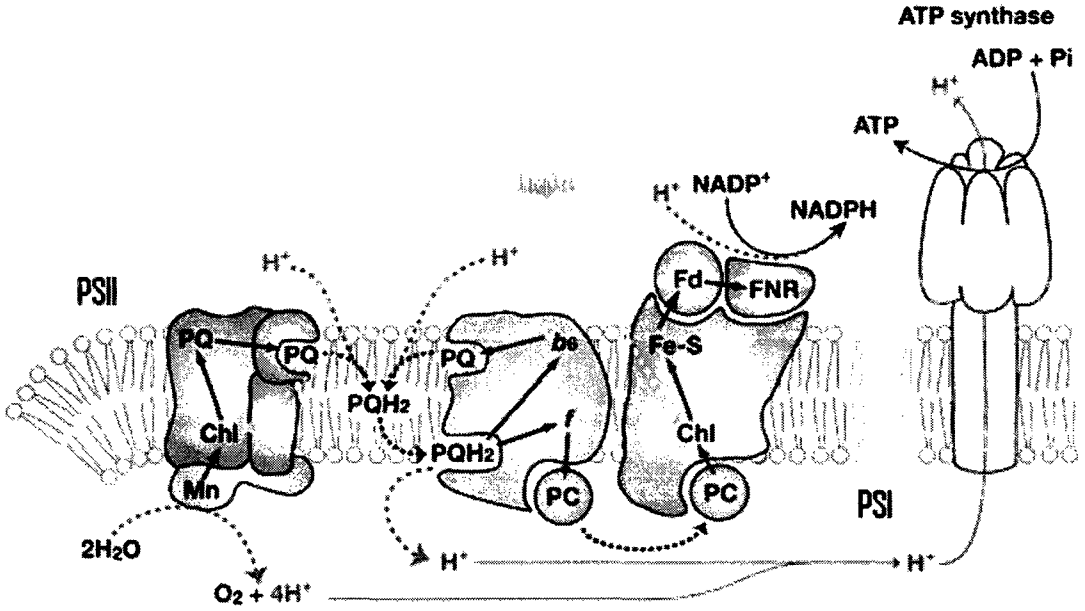

Figure 1.4: The electron transport system of oxygenic photosynthesis consists of three membrane spanning protein complexes, i.e., PS II, Cytochrome b_6f (Cyt b_6f) and PS I. PS II complexes oxidize water with light energy. When PS II is excited by four photons, the complex draws four electrons out of two molecules of water, and one oxygen molecule evolves. Such oxygen evolution occurs in the special subunit of PS II complex, "oxygen evolving subunit," containing four manganese atoms. An electron out of water is carried to a fat-soluble electron carrier, plastoquinone (PQ), in PS II (electron flow is indicated by blue arrows). The PQ in receipt of the two electrons gets two protons (H+) near by the membrane surface (the reduced PQ is shown as PQH_2), and carries protons and electrons to Cyt b_6f complex (the uptake and release of protons are indicated by red broken lines). Cyt b_6f complex carries the electrons to plastocyanin (PC), a water-soluble copper-protein. PC transfers the electrons from Cyt b_6f complex to Photosystem I (PS I). Another Chlorophyll-containing complex that runs on light is PS I, which pumps an electron to ferredoxin (Fd). Finally, the electrons are delivered to NADP+ via ferredoxin-NADP+ redactase (FNR) effecting NADPH. While electrons are delivered among three complexes, the proton gradient forms between the membrane. The difference of proton concentrate will be a motivating force for production of ATPs by ATP synthase. Image by Satoshi Hanada.

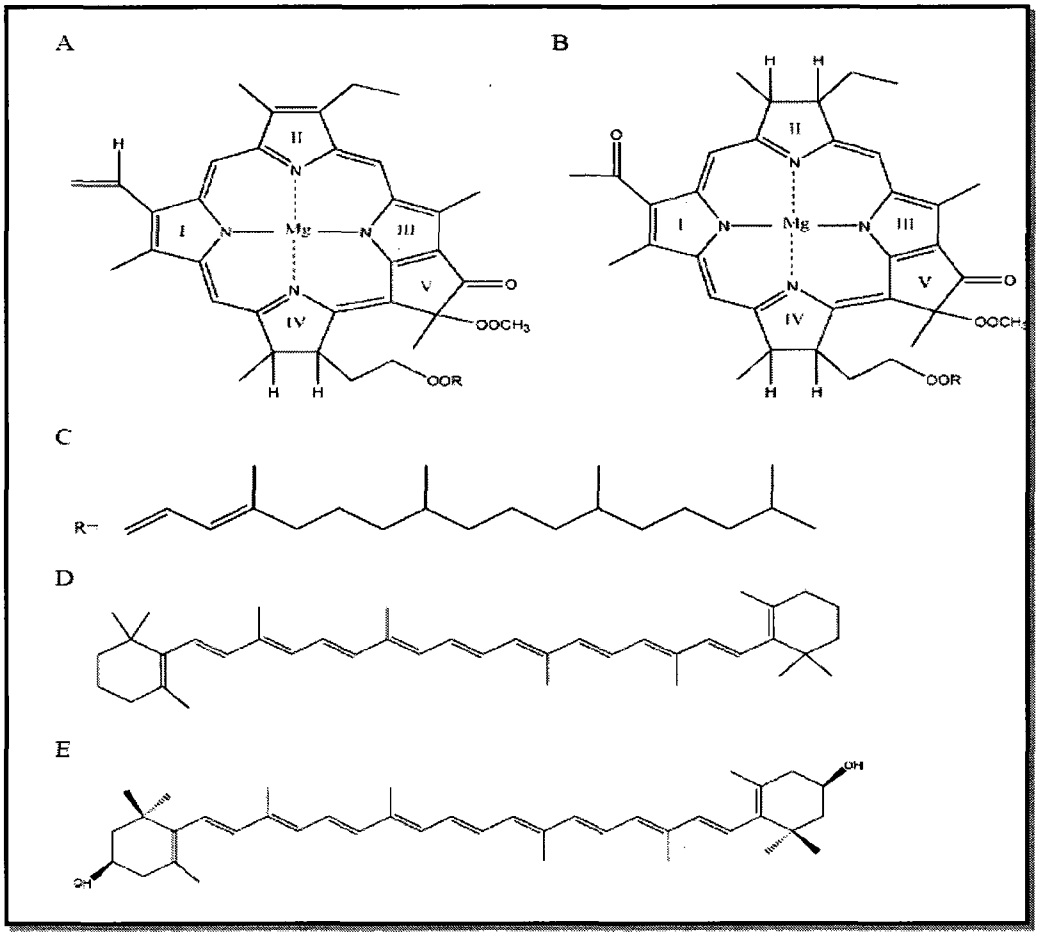

Figure 1.5: Chemical structures of (A) chlorophyll and (B) bacteriochlorophyll, with (C) being the phytyl tail; (D) beta-carotene, a carotenoid of photosystem II (PS II) which is responsible for quenching singlet states and preventing oxidation to the PS II RC, and (E) zeaxanthin, a xanthophyll which is an oxidized hydroxy derivative of beta-carotene, that is responsible for quenching reactive oxygen species in cyanobacterial and plant photosynthetic organisms. The Roman numbers I to V label the Chl and BChl rings according to the IUPAC nomenclature system. The structures of pheophytin and bacteriopheophytin respectively are identical to chlorophyll and bacteriochlorophyll, except that the central Mg atom is replaced with H atoms bonded to rings I and III.

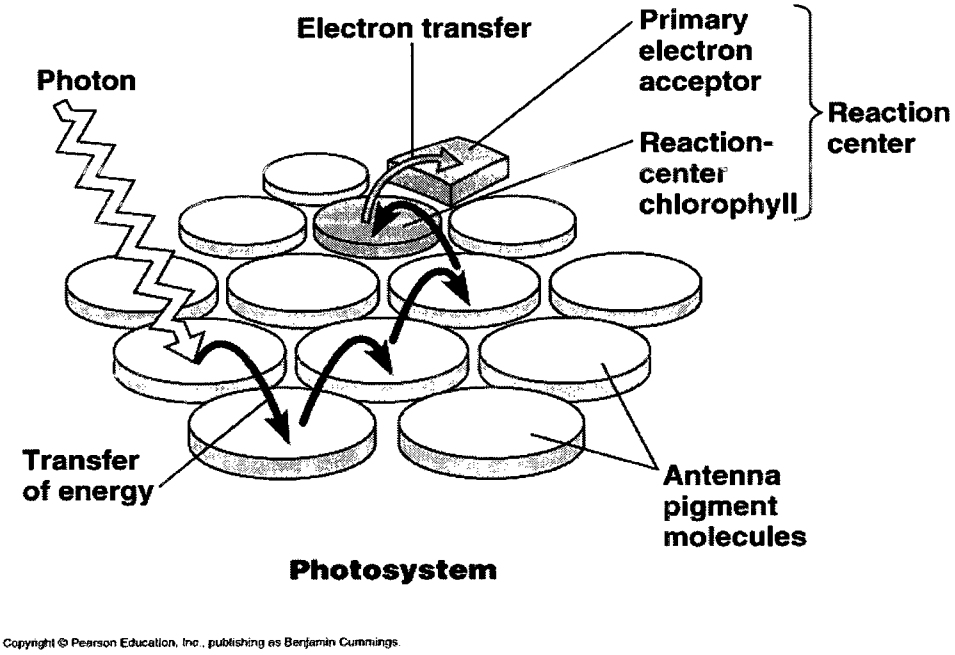

Figure 1.6. Schematic of light harvesting, energy transfer through antenna pigment molecules and transfer to the reaction center, where primary electron transfer (e.g. charge separation) is initiated. © Imperial College London.

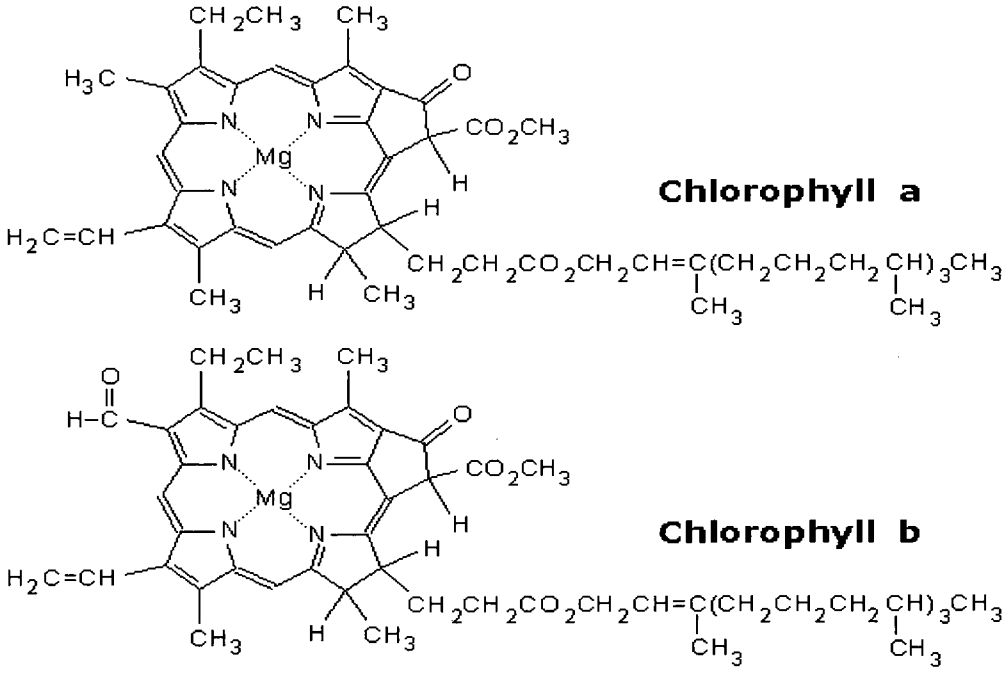

Figure 1.7: Chlorophylls *a* and *b* chemical structures. The size of the ring is about 1 nm, it is a planar molecule. A Mg atom in the center of the planar part is coordinated to four N-atoms. Each nitrogen is part of a substructural element of the molecule that comes from pyrrole, a cyclic compound with a nitrogen atom in a five-member ring with four carbons. From http://www.food-info.net/uk/colour/chlorophyll.htm

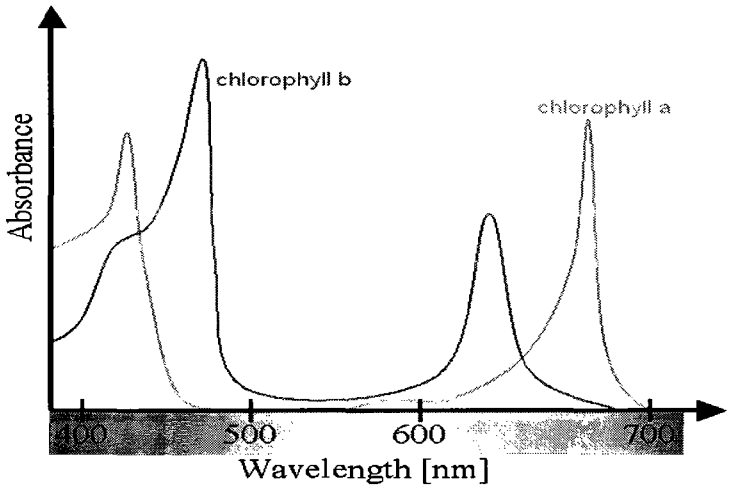

Figure 1.8: Absorbance spectra of chlorophyll *a* (green) and *b* (red) in an organic solvent (in the absence of protein). The spectra of chlorophyll molecules in PS complexes are slightly shifted depending on specific pigment-protein interactions. Image from http://www.answers.com/topic/chlorophyll

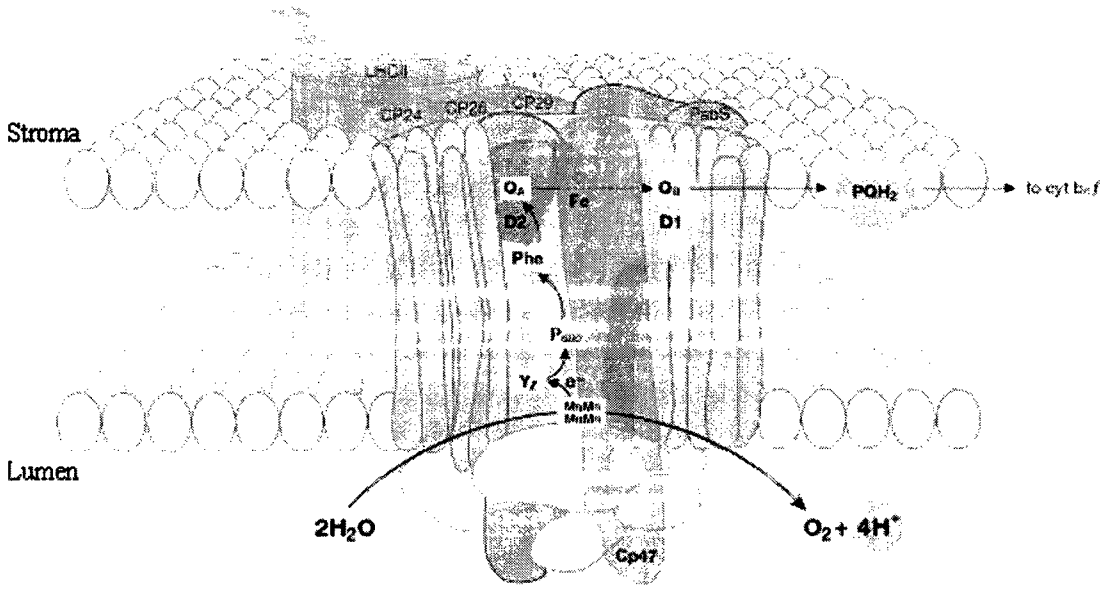

Figure 1.9 Organization of photosystem II and light-harvesting complex II in the thylakoid membrane. CP43, CP47: internal antenna chlorophyll–protein complexes. D1, D2: main components of reaction center (RC) with binding sites for electron acceptor quinones (Q_B, Q_A). P_{680}: chlorophyll special pair. Other cofactors associated with D1/D2: pheophytin (Phe), non-haem iron (Fe), Mn-cluster. Accessory chlorophylls and β-carotene are not shown. Chl, chlorophyll; PQH_2, plastoquinone pool; cytb6f, cytochrome b_6f complex; Y_Z, D1-Tyr161. For a more detailed description, see [9]. Image by J. Nield (Imperial College London, UK)

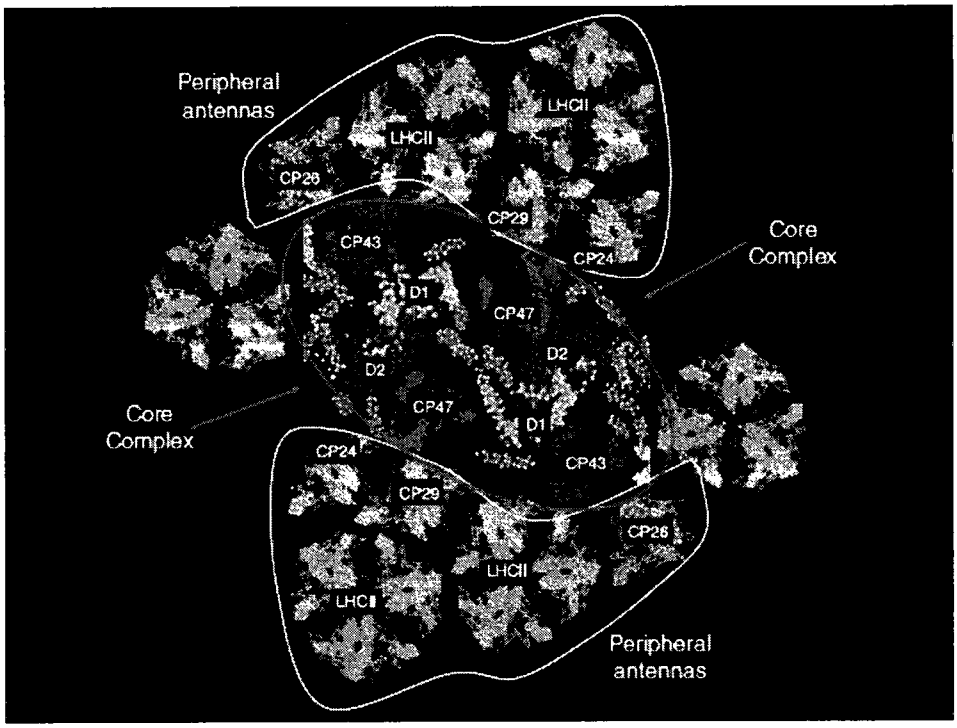

Figure 1.10. The overall structure of plant Photosystem II. (Image by Roberto Rossi)

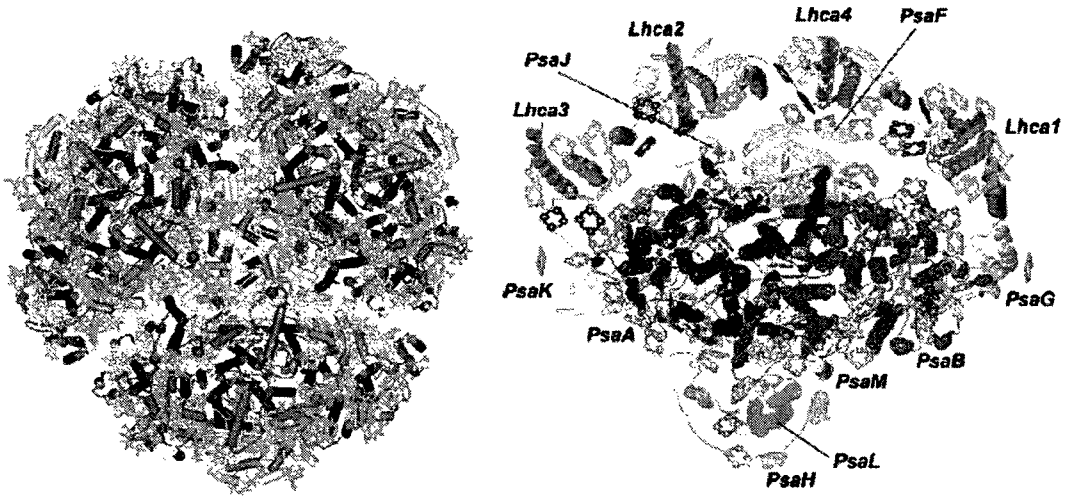

Figure 1.11: Cyanobacterial trimeric Photosystem I (left) and Plant Photosystem I (right). From [115].

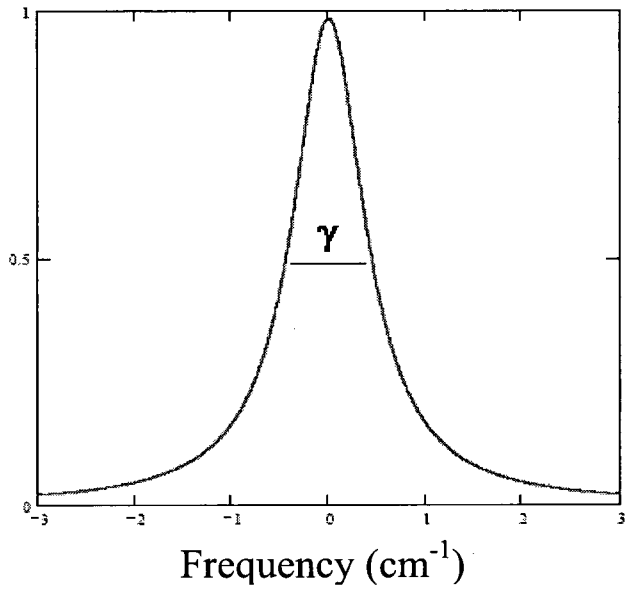

Figure 2.1 Natural or homogeneous shape of a spectral line [38]. The homogeneous profile is a Lorentzian and carries a full width at half maximum (FWHM) of $\gamma = 1/\pi cT_2$

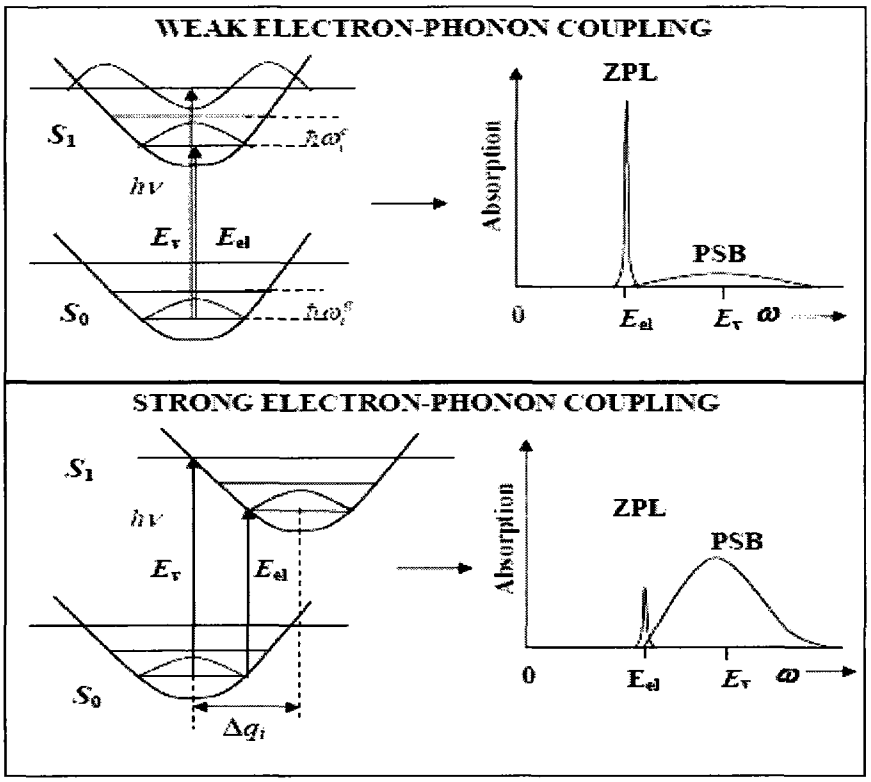

Figure 2.2. Schematic of the electron-phonon coupling of a guest impurity molecule in a low-T solid host matrix based on the Franck-Condon principle. A transition of the molecules from the ground electronic state, S_0, to the excited electronic state, S_1 after excitation at $h\nu$. The overlap between the ground and excited state vibrational wavefunctions is determined by the lattice coordinate displacement, Δq, the most probable transitions are those for which the overlap is the largest. E_{el} and E_v represent the purely electronic and most likely transition energies, respectively. $h\omega_t^g$ and $h\omega_t^{ex}$ are the ground and excited state vibrational energy levels, respectively. From [40].

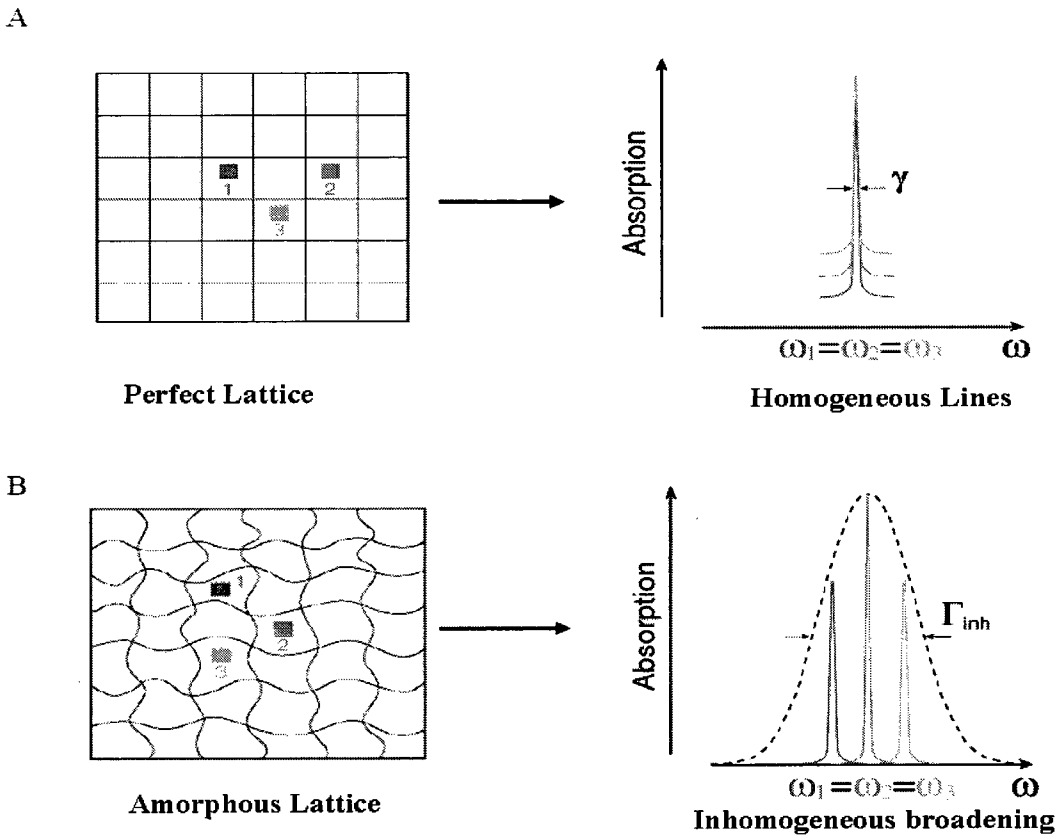

Figure 2.3. Schematic of homogeneous vs. inhomogeneous broadening. In frame (A), guest impurity molecules are in a perfect host lattice. Homogeneous lines overlap, resulting in an absorption spectrum with a linewidth equal to that of the individual ZPL. In frame (B) the impurity molecules are in a disordered host lattice, so that each impurity molecule absorbs at different frequency. This leads to a distribution of ZPL absorption frequencies and thus, the impurity absorption band is ***inhomogeneously broadened.*** (c) Tonu Reinot, ISU.

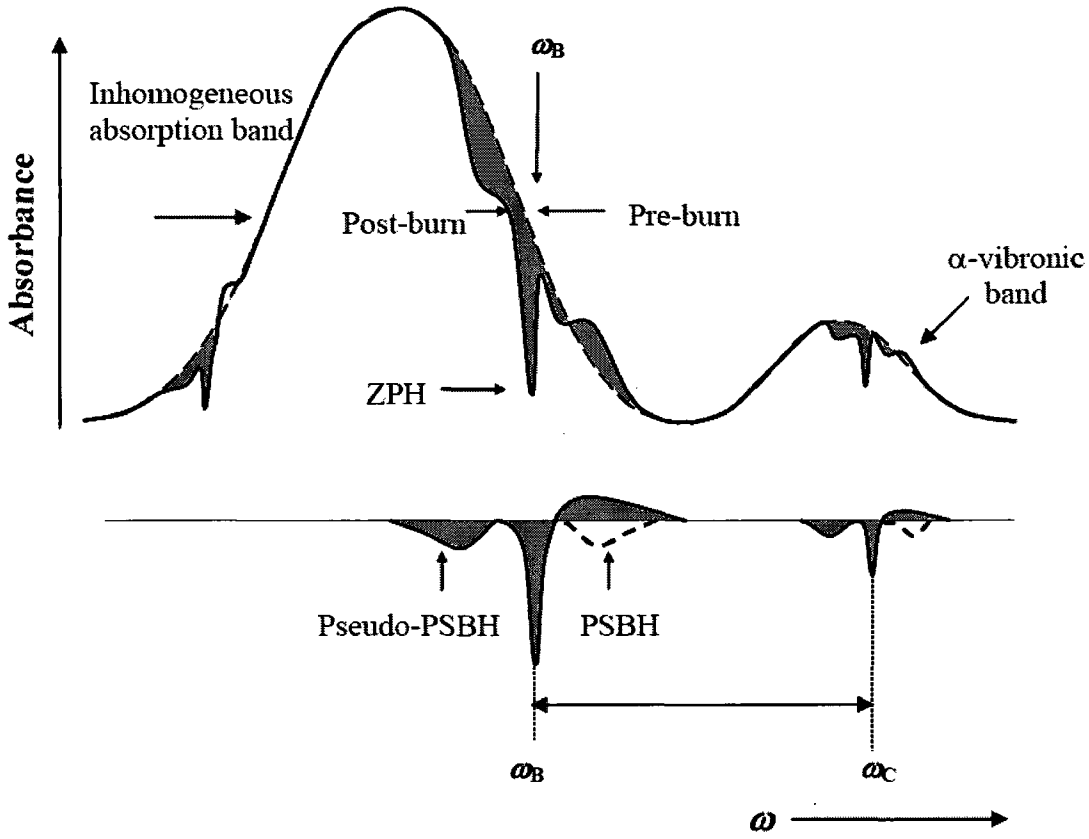

Figure 2.4. Spectral hole-burning in an inhomogeneously broadened absorption band [31]. Two curves represent the pre-burn (dashed-line) and the post-burn (solid line) absorption spectrum. After hole burning at frequency ω_B, the hole-burning spectrum is formed, as shown in the lower part of the figure (the pre-burn - post-burn absorption spectrum). Spectral holes form at ω_B and ω_C. The hole at ω_B consists of a zero-phonon hole (ZPH) component, which forms from burning out the ZPLs that are excited at ω_B. The "real" phonon side band hole PSBH forms from burning out the PSBs that are excited at ω_B. The pseudo-PSBH results from burning out the ZPLs that lie lower in energy to ω_B, and burn via their PSBs. A hole at ω_C that is a vibronic replica of the ZPH, with $\omega_C - \omega_B$ being some localized vibrational mode of the molecule.

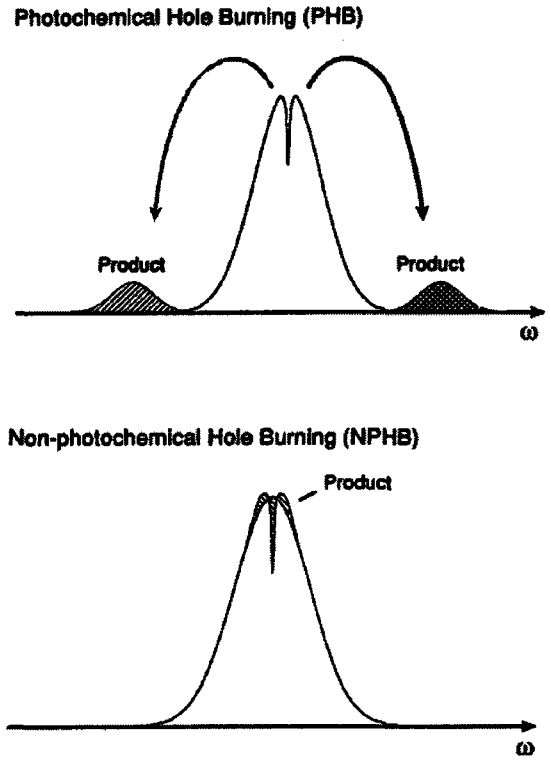

Figure 2.5: Spectral distribution of the photoproduct after photochemical (PHB) and non-photochemical (photophysical) (NPHB) hole burning. From [31].

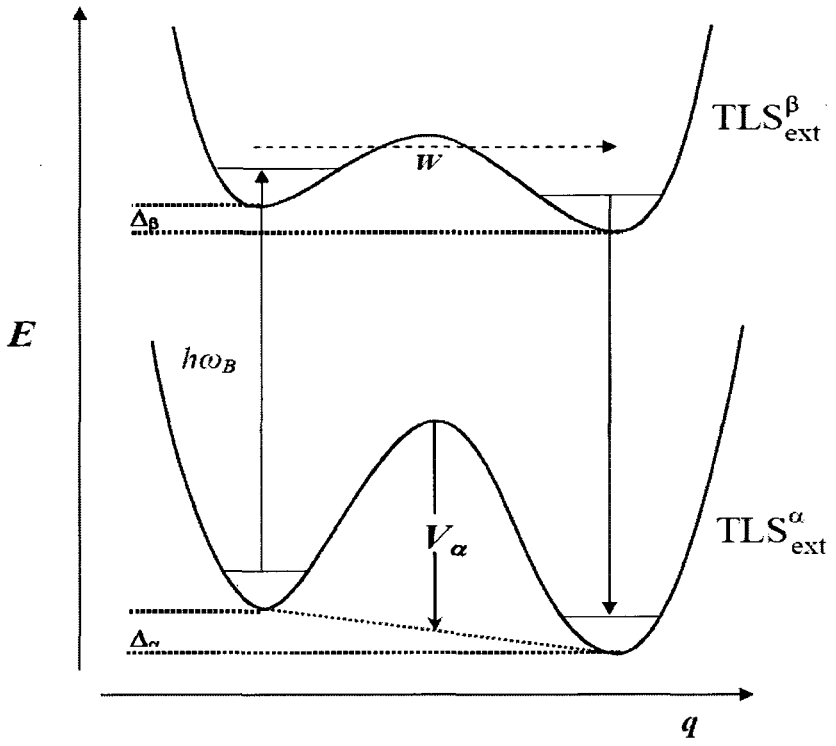

Figure 2.6. Schematic of the NPHB mechanism [22, 27, 31]. The diagram shows the extrinsic two level system (TLS_{ext}) of a guest molecule in the ground state (α) and excited state (β). After excitation ($h\omega_B$) at the burn frequency (ω_B) to β, the TLS_{ext} flips, due to the much lower barrier height (V_α) compared to the ground state, through phonon assisted tunneling (PAT), which is represented by the tunneling frequency, W. The molecule then decays to the ground state and finds itself in a different host configuration, and therefore absorbs at a different frequency. This results in the formation of a persistent spectral hole that can be observed experimentally. $\Delta\alpha$ and $\Delta\beta$ are the double well asymmetry parameters in the ground and excited state, respectively. q represents the intermolecular coordinate, ω_B is the burn frequency.

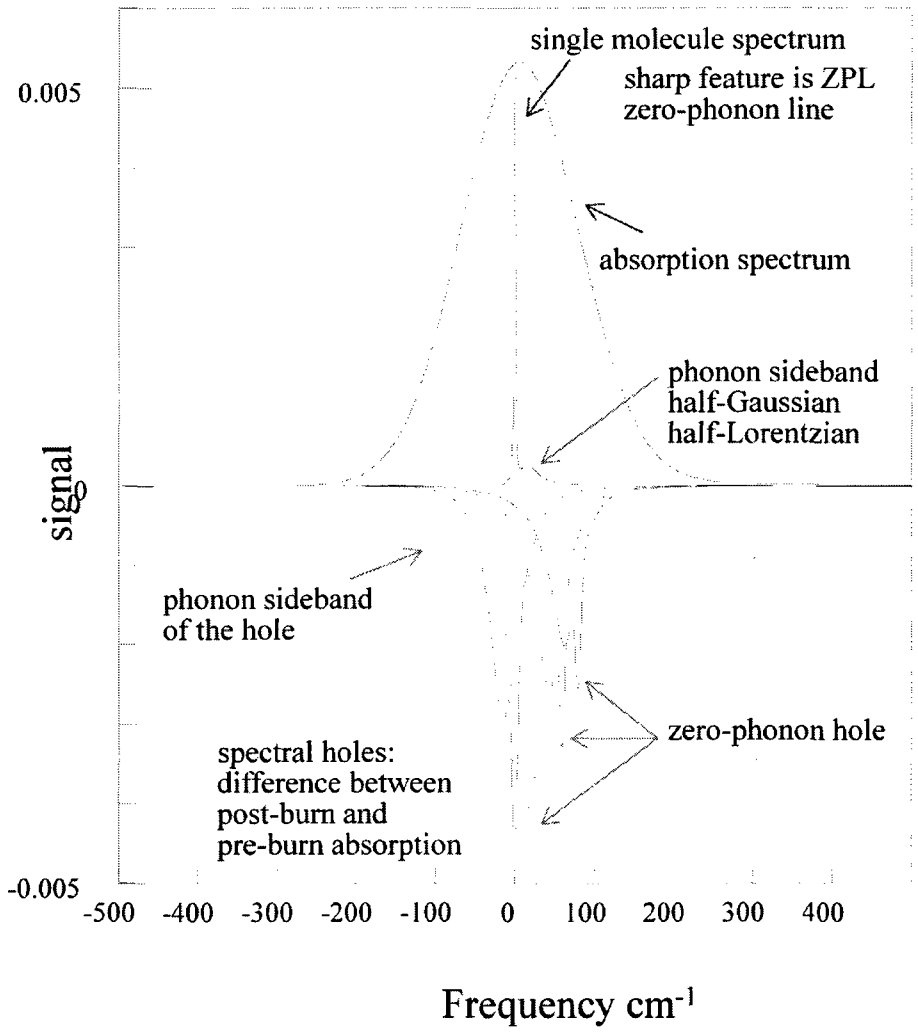

Figure 3.1: Simulated ensemble absorption spectrum (blue), single molecule absorption spectrum (brown) and several spectral holes burnt with the same irradiation dose at different wavelengths within the inhomogeneously broadened band.

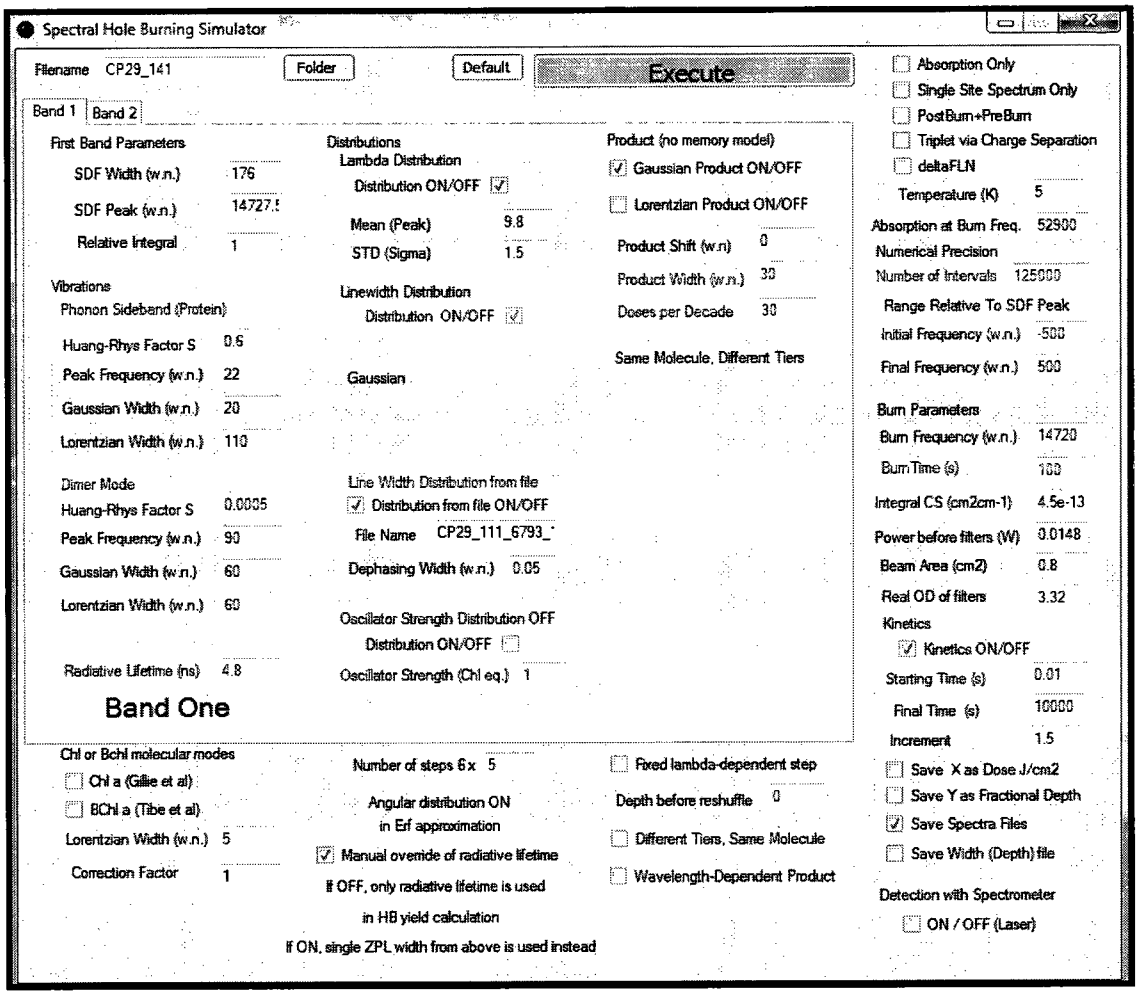

Figure 3.1B: Interface of Spectral Hole Burning Simulator.

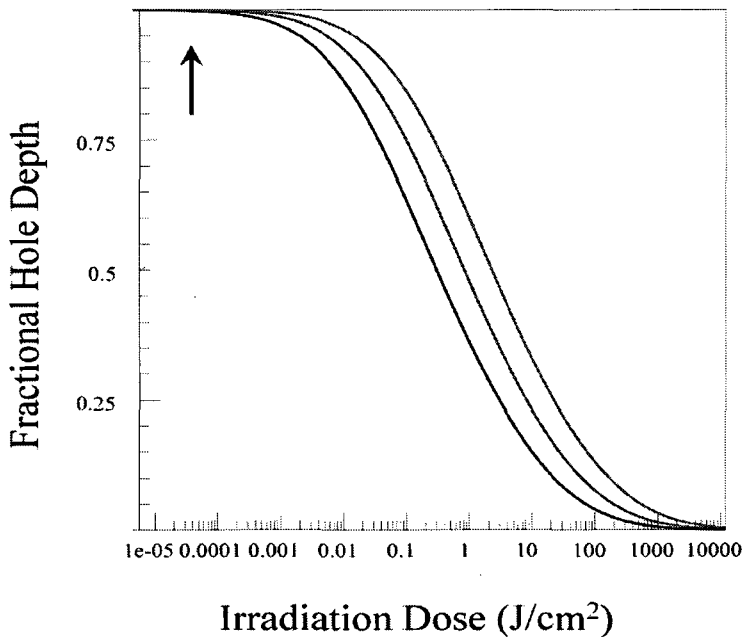

Figure 3.2: Simulated hole growth kinetic (HGK) curves (T=5 K), with burn wavelength coinciding with the SDF peak, The Gaussian distribution of tunneling parameter λ_0 was peaked at various λ_0 =11, 10.5 and 10, for red, blue and black curves, respectively. σ_λ=1. The homogeneous line width is 0.04 cm^{-1}.

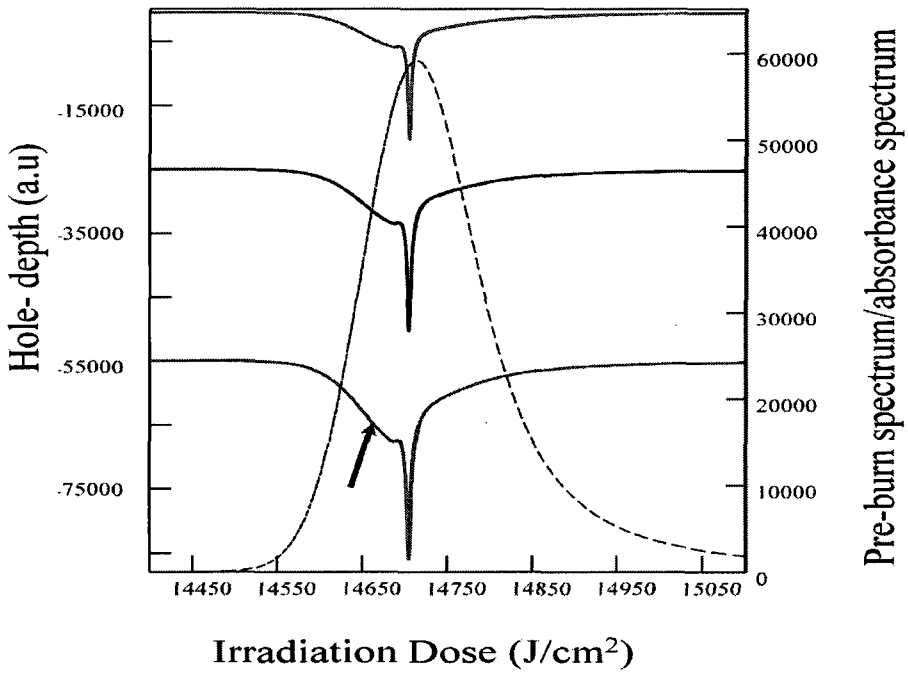

Figure 3.3: Simulation of absorption spectrum and the holes burnt at the peak of the SDF for various values of λ_0= 11, 10.5, and 10 corresponding to red, black and blue curves, respectively. σ_λ = 1; ZPL=3 cm^{-1}, i.e. there is no line-width distribution; other parameters are reported in Table 3.1.

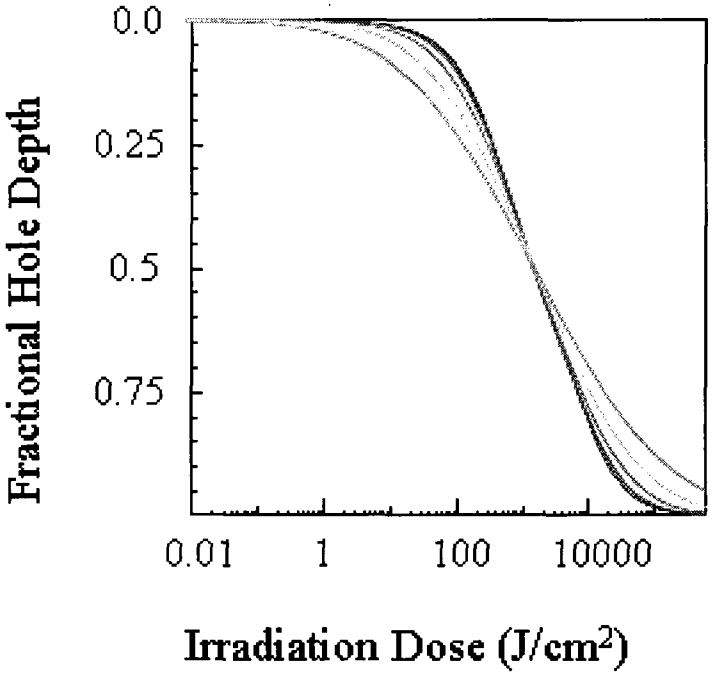

Figure 3.4: Dispersive hole growth kinetics (HGK) for λ_B at the peak of the SDF and in the absence of the line width distribution. ZPL width =3 cm^{-1}. The Gaussian distribution of tunneling parameter λ was peaked at 10 and had σ_λ= 0.0 (no dispersion), 0.3, 0.6, 1.0 and 1.5, corresponding to black, blue, red, green and purple curves, respectively.

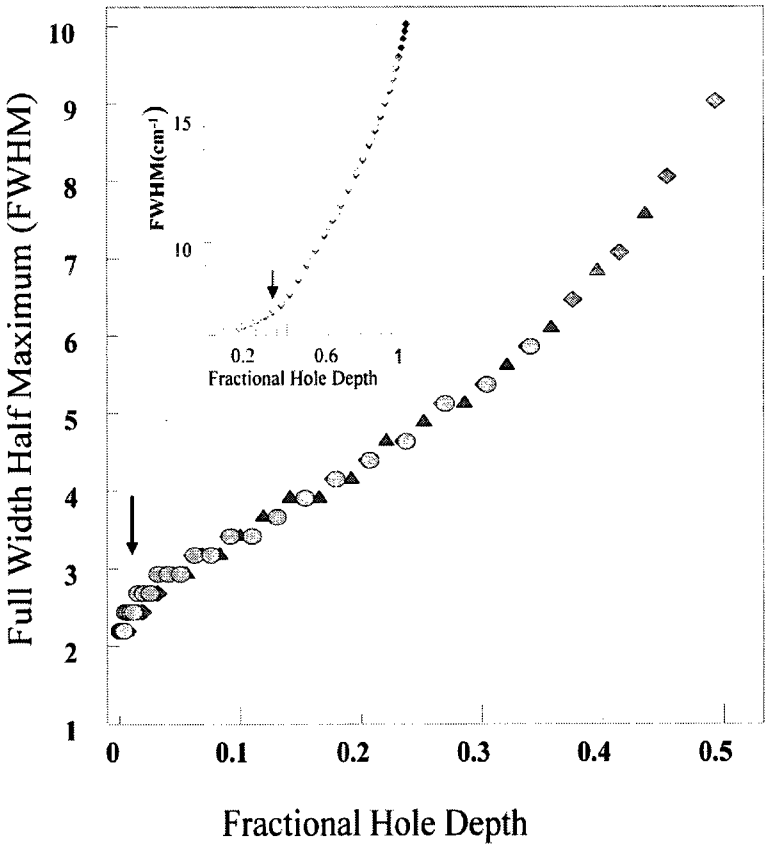

Figure 3.5: Hole FWHM dependence on Fractional hole depth. The diamonds, Triangles, and circles correspond to various values of λ_0 - 10, 10.5, and 11 respectively. σ_λ=1; ZPL width=1 cm^{-1} see Table 3.1 for other parameters that were used.

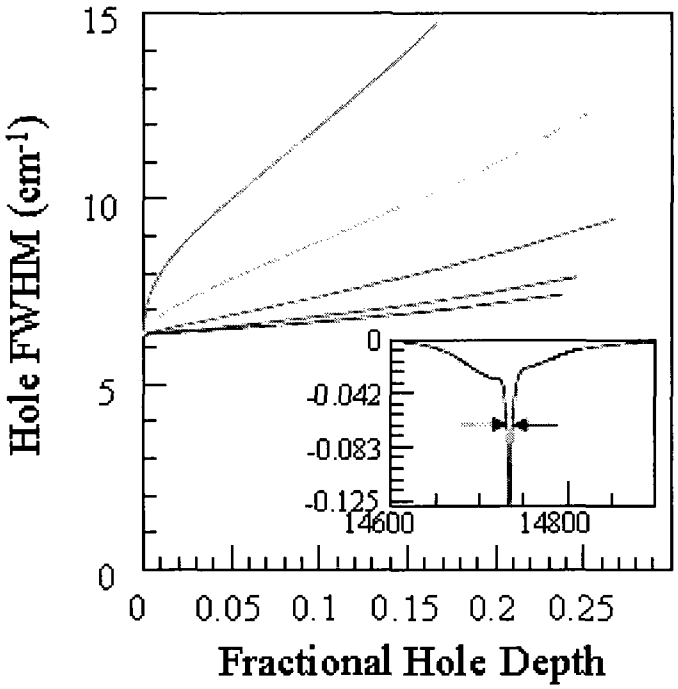

Figure 3.6: Hole FWHM as a function of the fractional hole depth, from bottom to top curves were obtained with tunneling parameter mean λ_0 =10 and σ_λ= 0.0, 0.3, 0.6, 1.0 and 1.5, respectively. The simulation was done with burning at the peak of the SDF and T=5 K. ZPL width was 3.0 cm^{-1}. The insert contains an example of the individual hole spectrum. Arrows indicate that hole width was measured at half the maximal depth. Green curve in this figure is the same as the black one in the figure to the left.

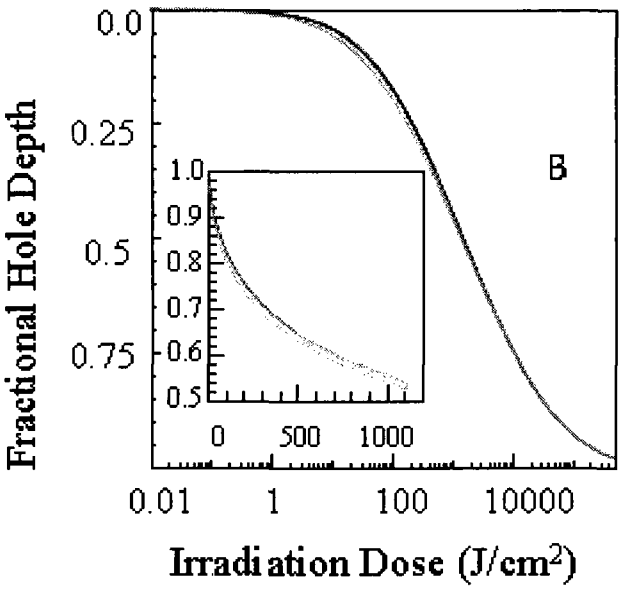

Figure 3.7 A semi-logarithmic plot of the fractional hole depth as a function of irradiation dose at 5 K. The calculation was performed with Gaussian linewidth distribution peaked at 3 cm^{-1} and with widths 0.0 (no distribution) 0.5, 1.0, 2.0 an 3.0 cm^{-1} corresponding to black, blue, red, green and purple curves respectively. The insert depicts the beginning of the curves on a regular (not logarithmic) scale. λ_0=10 and σ_λ=1.0

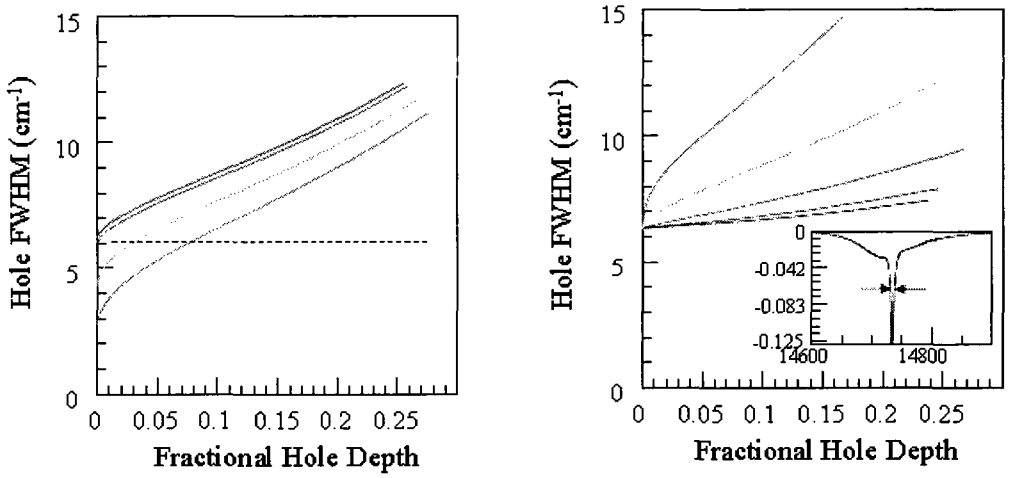

Figure 3.8: **Left frame:** Hole FWHM as a function of fractional hole depth. The simulation was done at 5 K and with burning at the peak of the SDF and with linewidth distribution peaked at 3.0 cm^{-1} and with widths of 0.0 (distribution off), 0.5, 1, 2.0, and 3.0 cm^{-1}, corresponding to black, blue, red, green and purple curves respectively. The λ-distribution was peaked at $\lambda_0 = 10$ and had σ_λ=1.0. Dashed horizontal line is twice the mean of the linewidth distribution.

Right frame: (same as Figure 3.6 for comparison) Hole FWHM as a function of the fractional hole depth, in the absence of the line width distribution. From bottom to top curves were obtained with tunneling parameter mean λ_0 =10 and σ_λ= 0.0, 0.3, 0.6, 1.0 and 1.5, respectively. The simulation was done with burning at the peak of the SDF and T=5 K. ZPL width was 3.0 cm^{-1}. The insert contains an example of the individual hole spectrum. Arrows indicate that hole width was measured at half the maximal depth. Green curve in this figure is the same as the black one in the figure to the left.

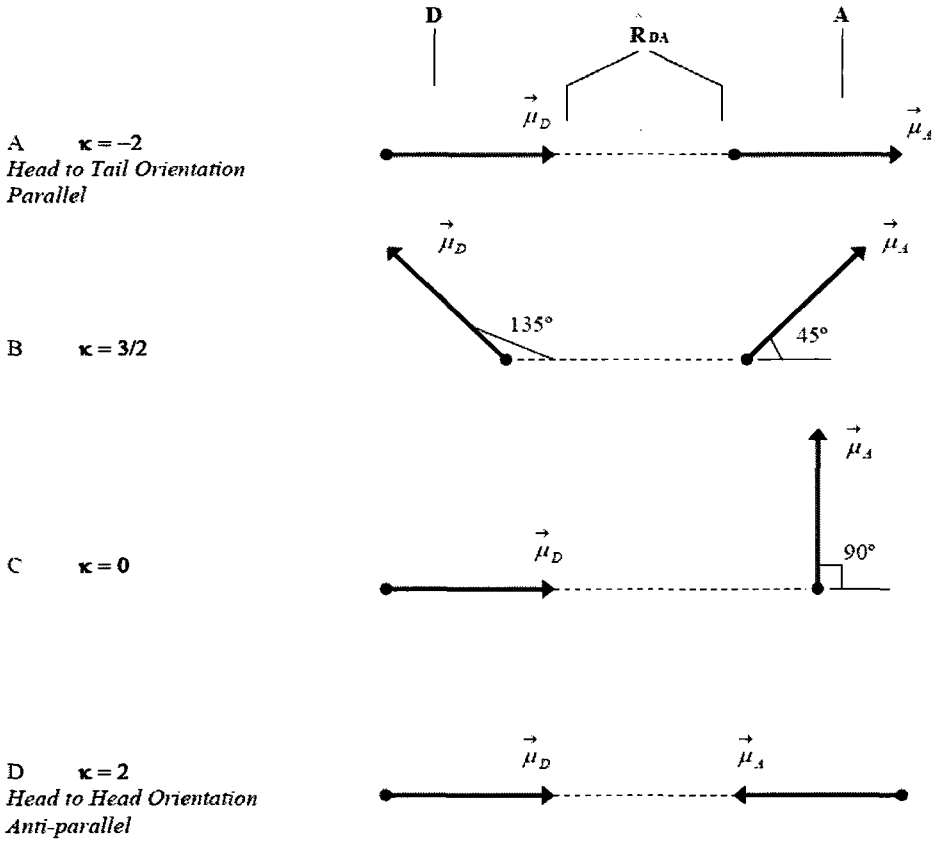

Figure 4.1: Examples of donor-acceptor dipole orientations with respective factors κ. The solid arrows represent the dipole vectors of the donor and acceptor molecules. The dashed line that connects the vectors represents the distance, between the two molecules. It is assumed here, for simplification, which both the donor and acceptor molecules are in the same plane. However, this cannot be assumed for real molecular systems.

A

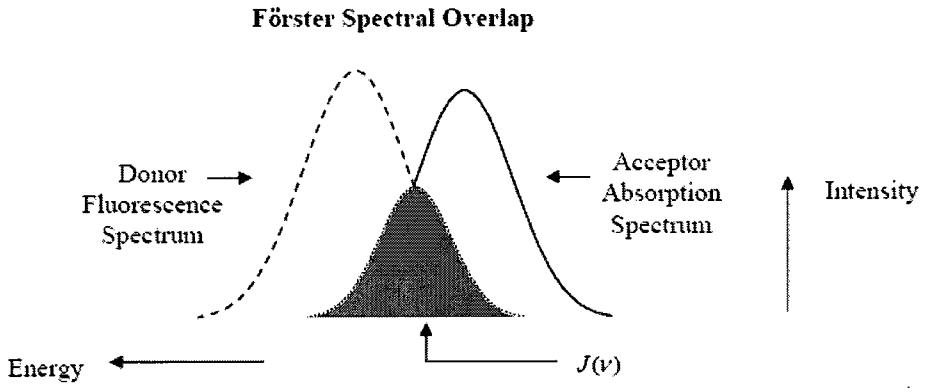

B

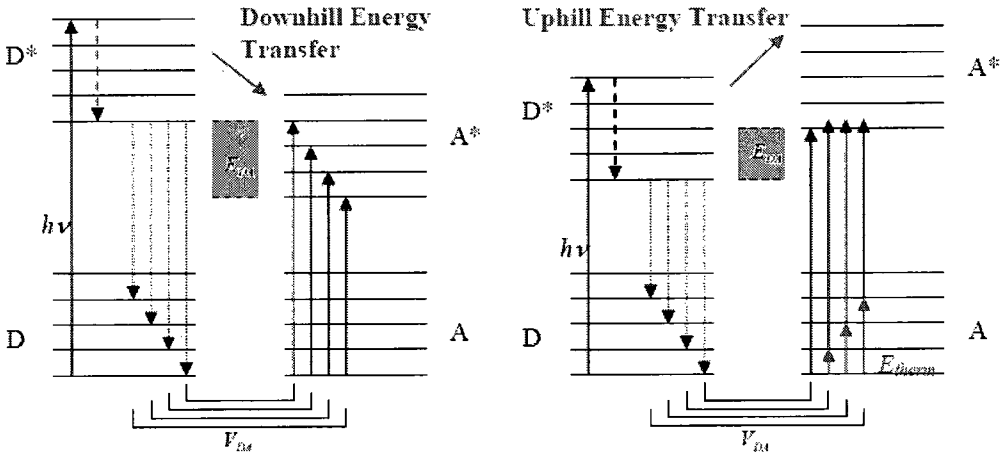

Figure 4.2: A*: A* conceptual of the spectral overlap, J(ν) [16]. B: The resonance energy transfer condition between the donor (D) and acceptor (A) molecule.

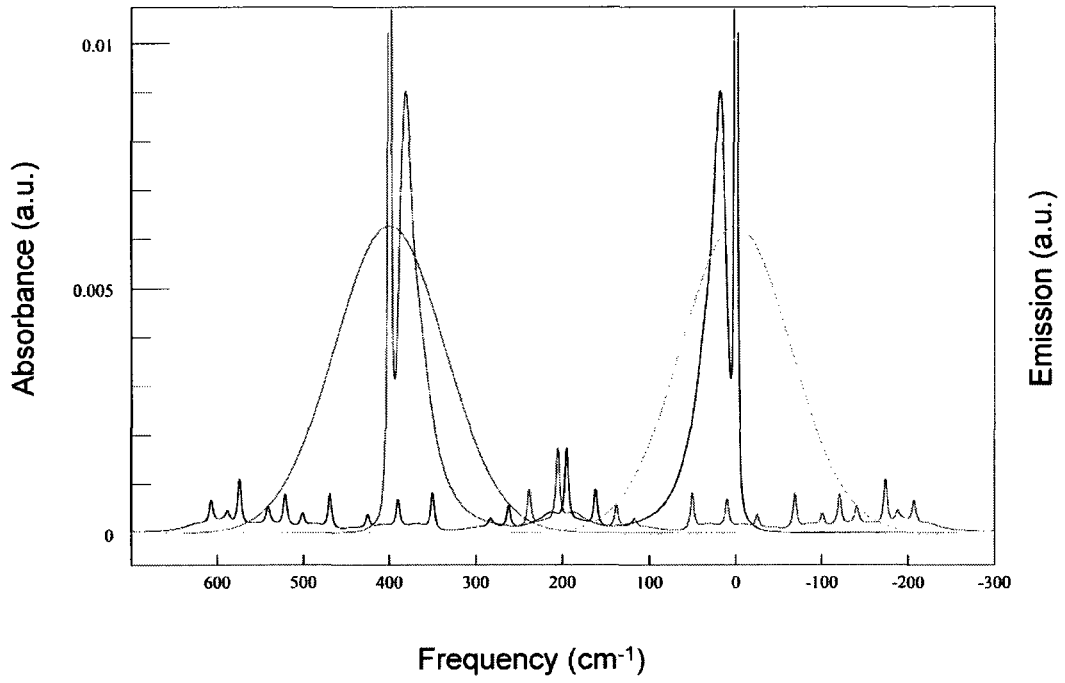

Figure 4.3 donor emission (blue) and acceptor absorption (black) spectra calculated numerically using HB simulator program, as well as respective site distribution functions of donor (red) and acceptor (green) pigments.

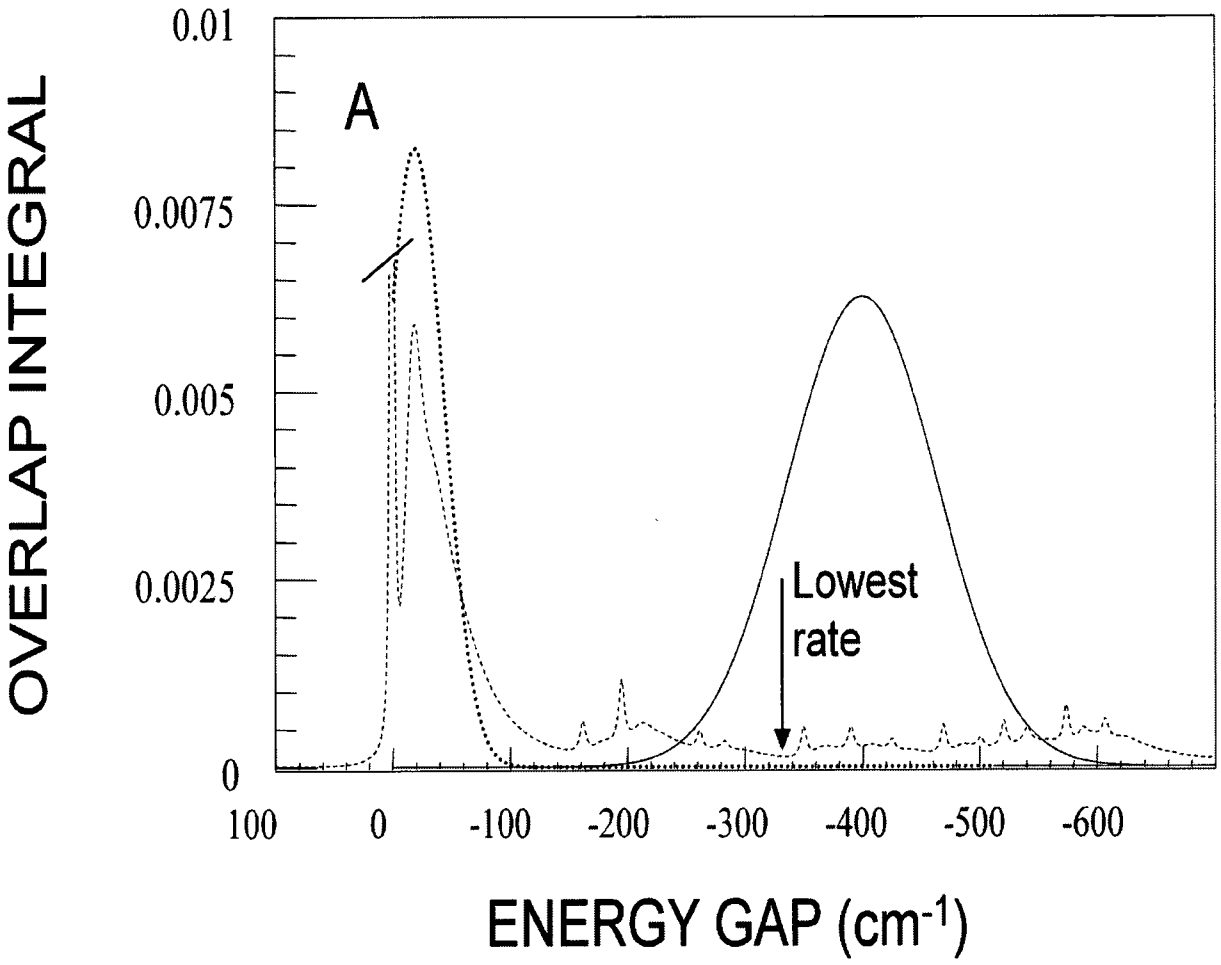

Figure 4.4 Overlap integral calculated numerically (dashed curve), acceptor SDF (solid curve) and the overlap integral according to Kolaczkowski et al (dotted surve).

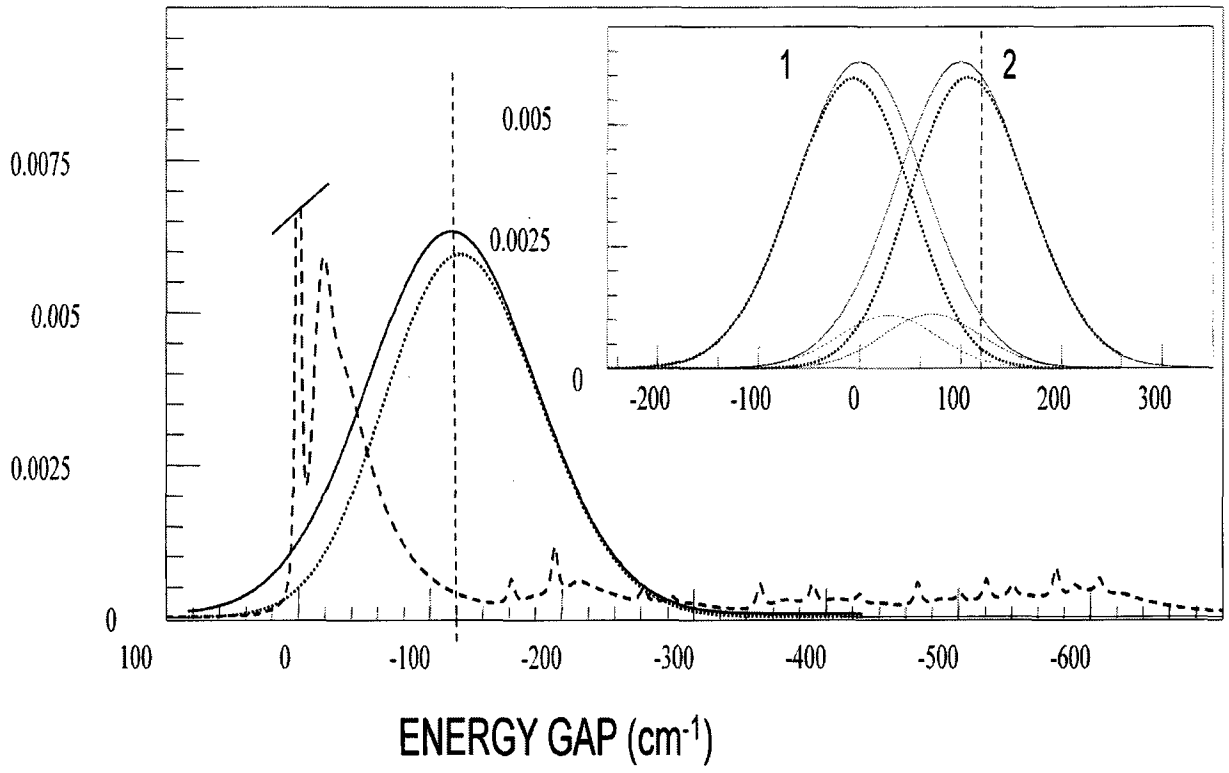

Figure 4.5 Main frame: spectral overlap function (dashed line, the ZPL-ZPL part is cut) as well as whole acceptor SDF (solid line) and part of that SDF which corresponds to acceptor pigments which are, indeed, the lowest-energy pigment molecules of the complex. The insert depicts donor and acceptor SDFs (solid lines labeled by 2 and 1, respectively) as well as the fractional SDFs of the pigments capable and incapable of energy transfer.

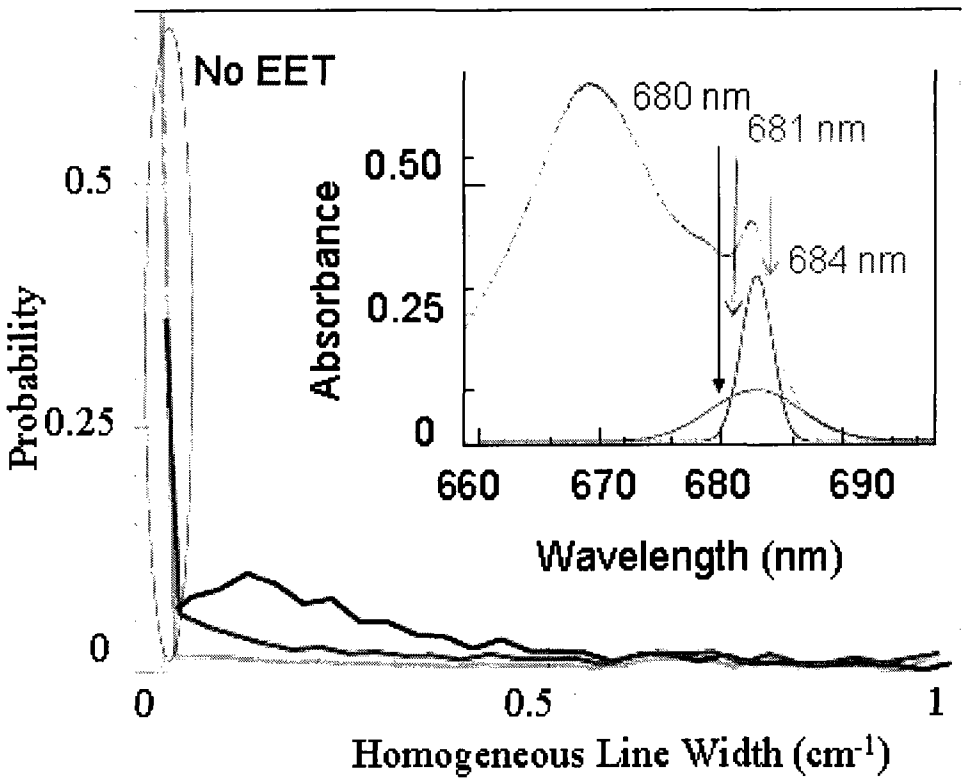

Figure 4.6. Theoretical homogeneous line width distributions calculated for V_{DA}=7.6 cm^{-1} at various wavelengths for the case of burning into two SDFs, both peaked at 683 nm, one 180 cm^{-1} wide and another 65 cm^{-1} wide. The insert contains the absorption spectrum of CP43 complex as well as the SDFs of the states A and B.

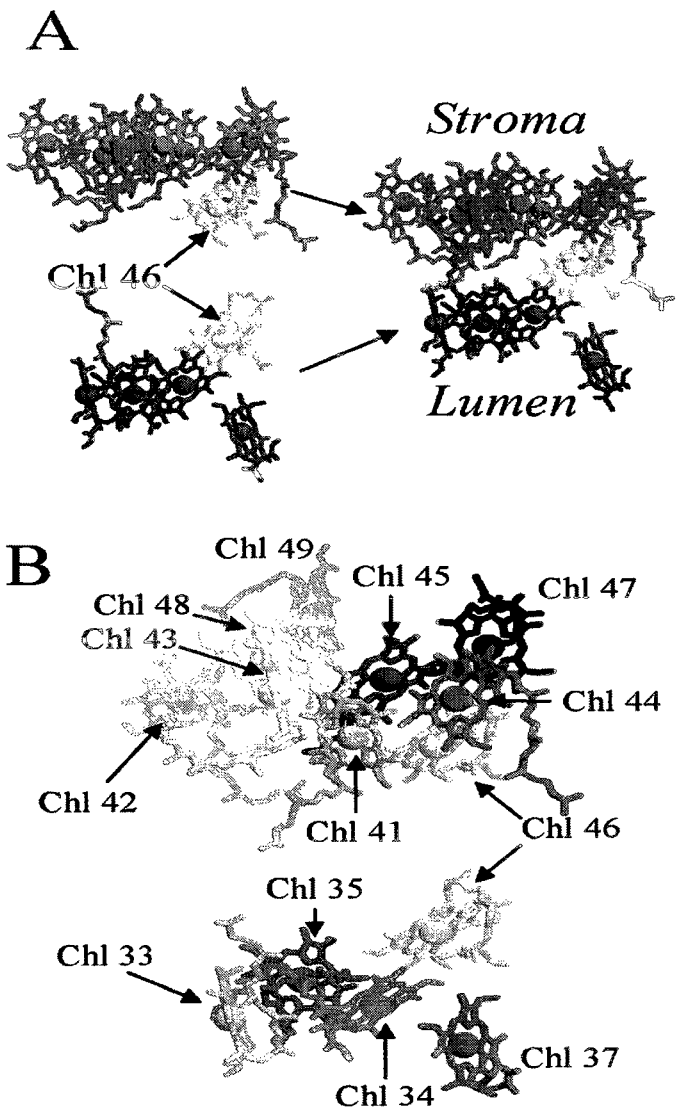

Figure 4.7. The Chls of the CP43 antenna protein. *Frame A*: Chls on the stromal side of the membrane are colored red, Chl 46 (which lies in the middle of the membrane) is colored pink, and lumenal Chls are colored blue. *Frame B*: CP43 chlorophylls separated into stromal and lumenal groupings and labeled according to Loll et al [8]. Note that Chl 46 is shown twice for clarity. From [112]

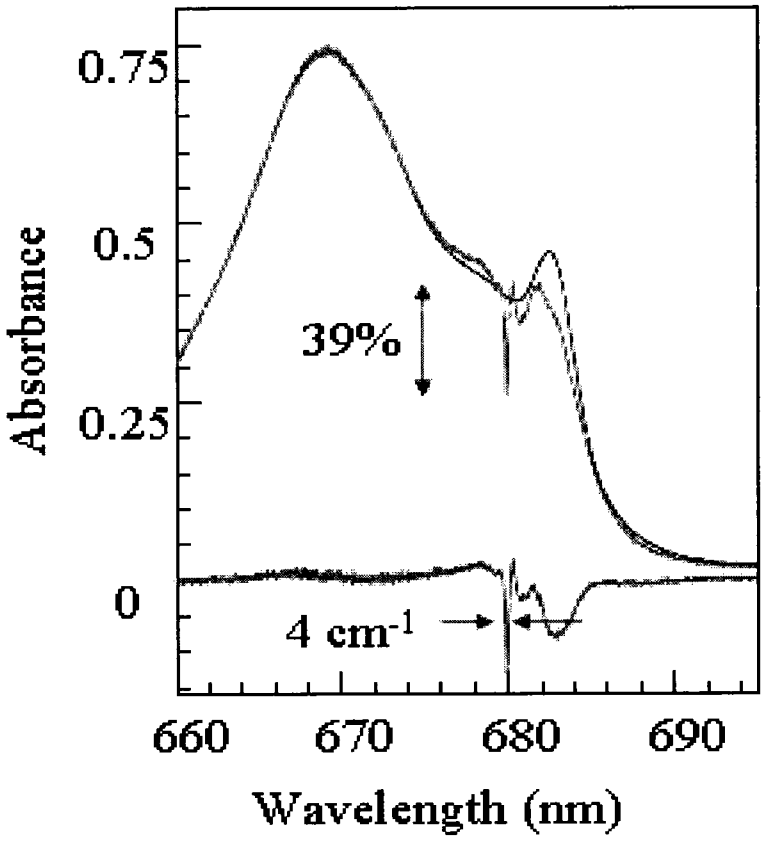

Figure 4.8: Absorption spectra of CP43 at 5 K and the hole burnt at 680 nm with 500 J/cm^2

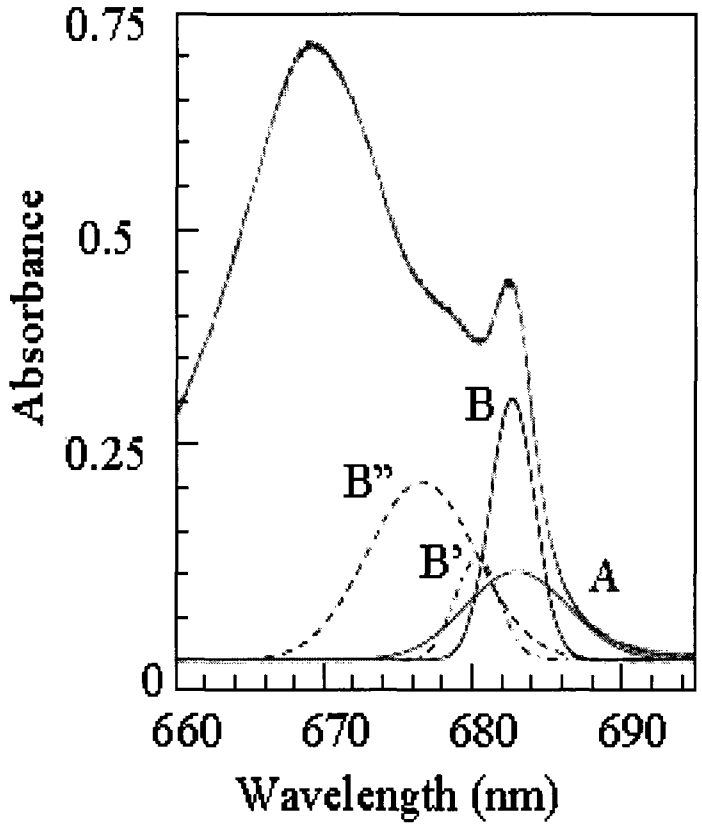

Figure 4.9. Absorption spectrum of CP43 at 5K and SDFs of A and B states. B' and B" bands are upper excitonic components of B according to Hughes et al [114].

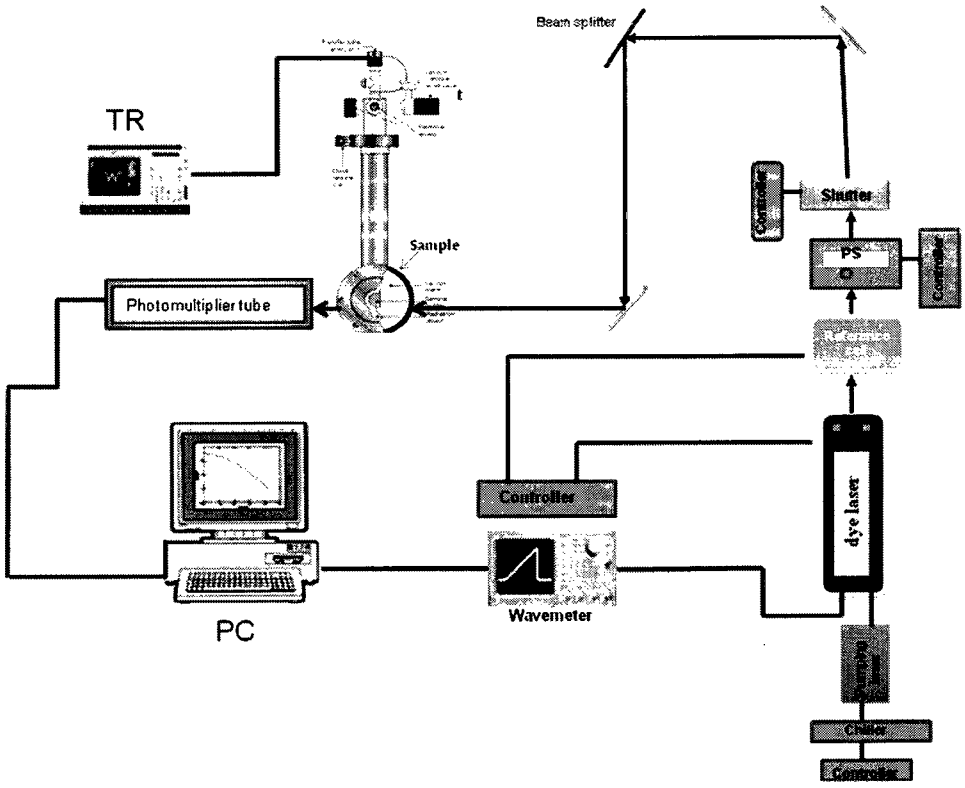

Figure 5.1. The experimental setup employed when measurements were performed in the fluorescence excitation mode.

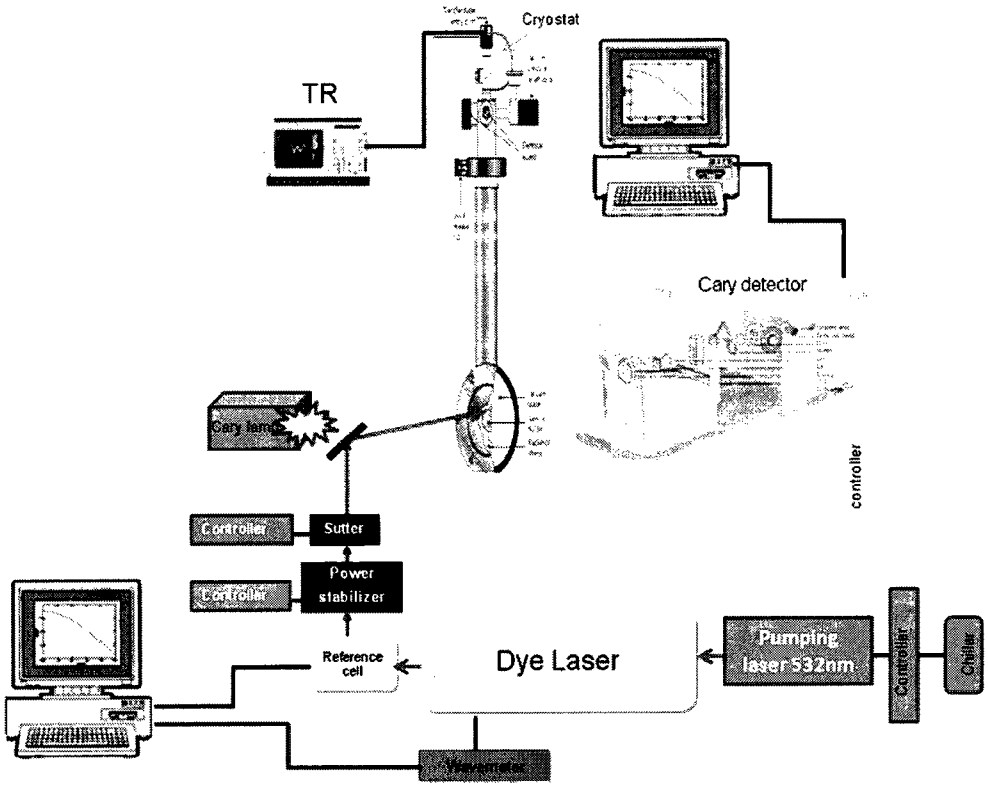

Figure 5.2. Experimental setup in absorption mode.

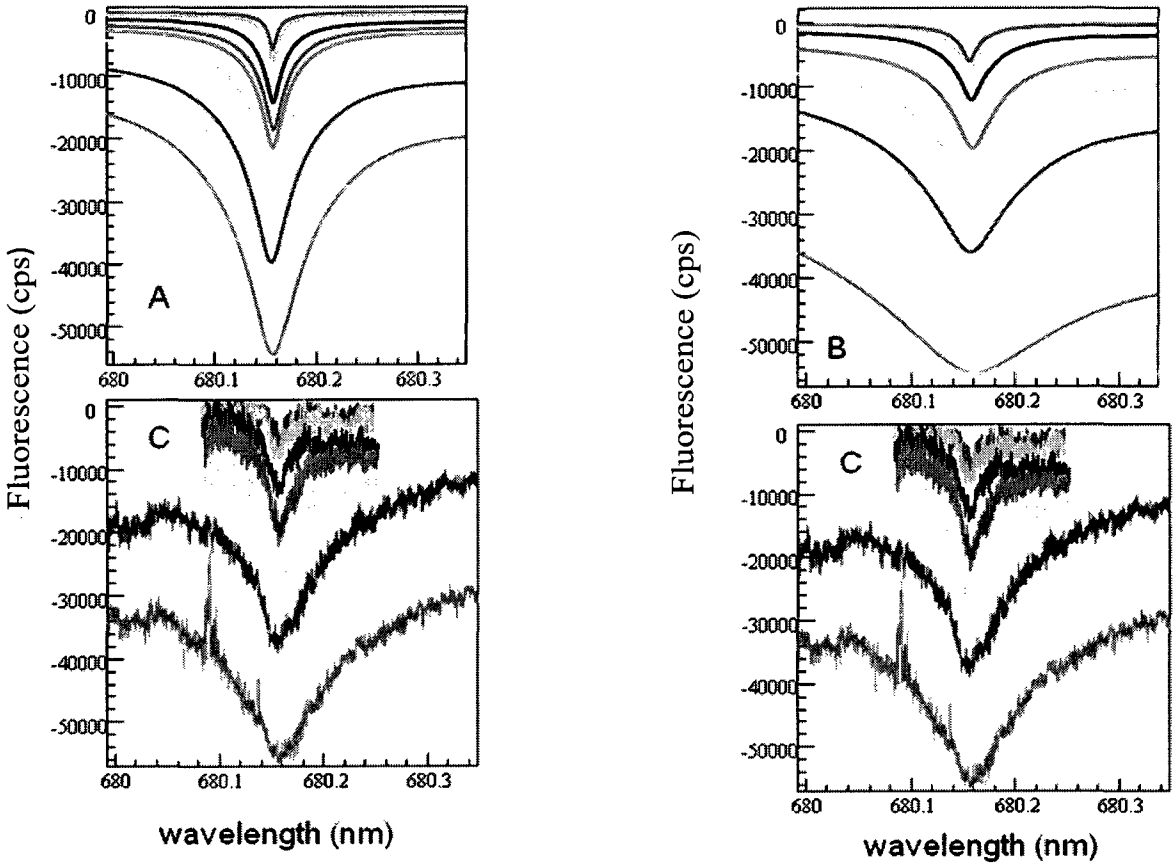

Figure 5.3 *Frame A and B*: Simulated burned holes spectrum of CP43 for A to B coupling of 11 cm^{-1} calculated using HB simulator, with A1B1 and A1B3 models, respectively. *Frame C*: The experimental holes burnt in the fluorescence excitation spectrum of CP43 of a spinach PSII core complex at 5K. Note that pre-burn absorption was ~160,000.

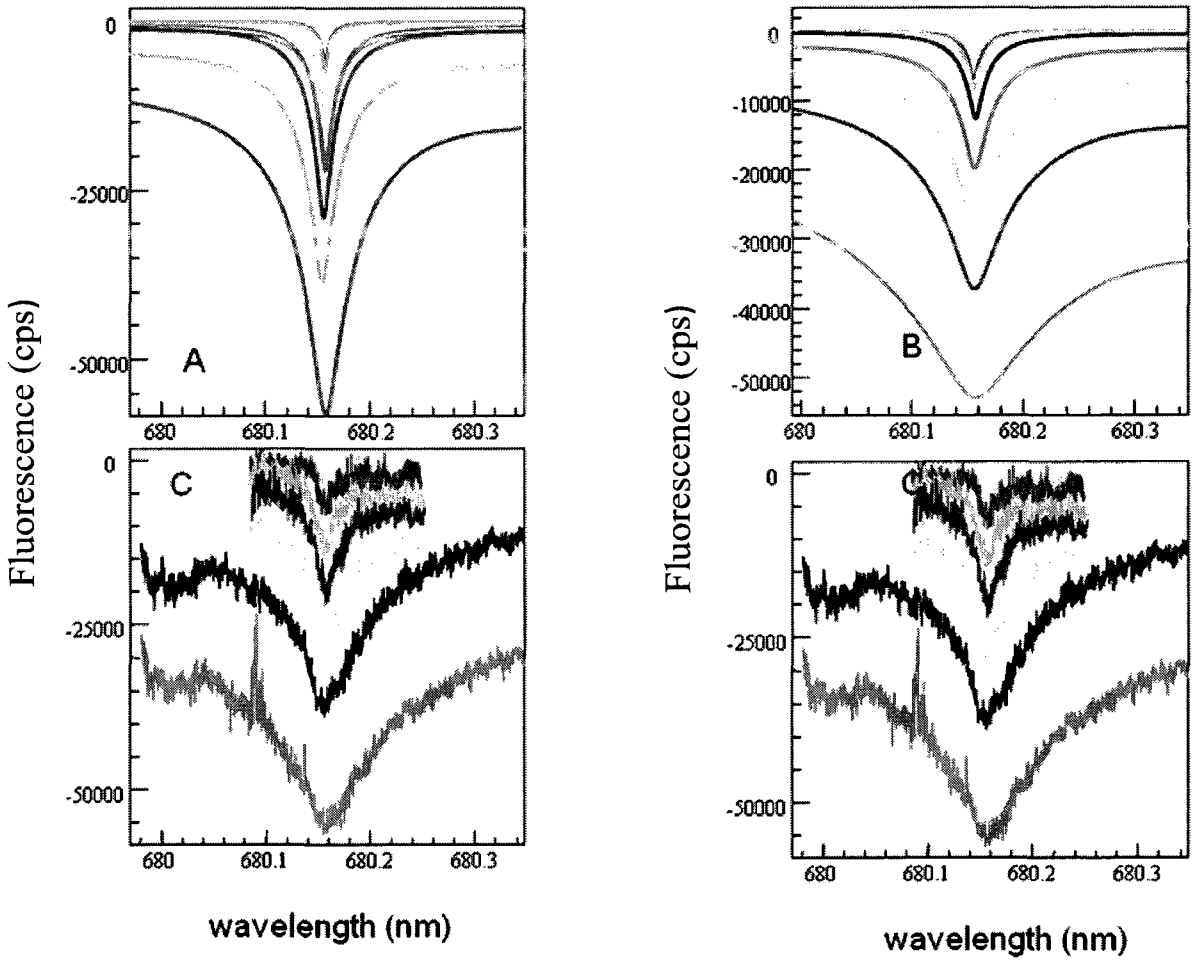

Figure 5.4 *Frames A and B*: Simulated burned hole spectrum of CP43 for inter-pigment coupling of 7.6 cm^{-1} and A1B1 model (left) and A1B3 model (right). *Frame C*: The experimental holes burnt in the fluorescence excitation spectrum of CP43 of spinach PSII core complex at 5 K.

LIST OF TABLES

Table 3.1 Simulation parameters of modeling for ZPH growth kinetics

Parameters(*Band A*)	Value
Zero-phonon Line width	3 cm^{-1}
Peak Energy of PSB (ω_m)	14705 cm^{-1}
Huang-Rhys factor(S)	0.6
Profile of PSB	$\Gamma_{Gaussian}$ (cm^{-1}) =22; $\Gamma_{Lorentzian}$ 140 cm^{-1}
Tunneling parameter (λ_0)	10
σ_λ	1
Phonon sideband - Peak Frequency (ω_B)	22 cm^{-1}
SDF Profile	Peak 14705 cm^{-1}; width 135 cm^{-1}
Actual burn position:	14705 cm^{-1}
Integrated cross-section:	$4.5 \cdot 10^{-13} cm^2 cm^{-1}$

Table 4.1: Simulation parameters for overlap function generation and for subsequent data fitting (CP43 [72])

CP43 [JL; 2000]	SDF peak and width (cm^{-1})	ω_B (cm^{-1})	S_{PSB}	ω_m; Γ_{Gauss}; $\Gamma_{Lorentz}$ (cm^{-1})	λ_0	σ_λ
A	14643; 180	14705	0.30±0.05	17; 11; 70	11±0.1	1.0±0.1
B	14643, 65	14705	0.30±0.05	24, 15, 70	10.5±0.3	1.0±0.1

Table 4.2. Dipole-Dipole couplings between CP43 chlorophylls (in cm^{-1}).

chl	33	34	35	37	41	42	43	44	45	46	47	48	49
33		-12.2	-6.5	-2.4	-4.4	15.6	16.6	1.8	-10.4	3.3	-2.3	-1.0	-0.06
34			-33.3	109.9	1.2	-8.6	-11.2	6.3	30.0	87.4	14.2	-7.6	-1.2
35				-26.5	-2.4	-1.4	-5.9	-6.8	-7.3	-23.2	-7.6	20.6	5.7
37					2.0	4.3	2.2	**7.6**	-1.6	33.7	3.6	-3.2	4.45
41						-19.8	-86.7	-25.8	28.9	-4.0	-1.8	3.2	-5.0
42							58.8	13.2	-26.7	12.1	5.3	-6.8	9.7
43								-11.0	69.0	-0.9	-7.6	28.0	-21.4
44									42.8	65.6	64.9	-21.6	11.6
45										-48.4	127.1	17.5	-7.1
46											-74.1	-10.5	10.8
47												-22.6	13.0
48													-81.8
49													

Table 5.1 A/B Simulation parameters of Bands A and B of CP43

Parameters(*Band A*)	Value
Inhomogenous Width:	180 cm^{-1}
SDF peak position:	14641 cm^{-1}
Relative amplitude:	1
Dephasing-Limited ZPL Width:	0.033cm^{-1}
Lambda Distribution:	Included with peak and st.dev. of 10.5 and 1
Oscillator Strength	1
Phonon Sideband - Strength:	0.3cm^{-1}
Phonon sideband - Peak Frequency:	17cm^{-1}
Phonon - Gaussian Width:	15cm^{-1}
Phonon - Lorentzian Width:	70cm^{-1}
Radiative Lifetim	3ns

Parameters(*Band B*)	Value
Inhomogenous Width:	65 cm^{-1}
SDF peak position:	14641 cm^{-1}
Relative amplitude:	1
Dephasing-Limited ZPL Width:	0.033 cm^{-1}
Lambda Distribution:	Included with peak and std. dev. of 11 and 1
Oscillator Strength:	1
Phonon Sideband - Strength:	0.3 cm^{-1}
Phonon sideband - Peak Frequency:	24 cm^{-1}
Phonon - Gaussian Width:	15 cm^{-1}
Phonon - Lorentzian Width:	70 cm^{-1}
Radiative Lifetime:	3 ns

List of Abbreviations

Chl	Chlorophyll
E	energy
EET	excitation energy transfer
FLN	fluorescence line-narrowing
FWHM	full width at half maximum
S	Huang-Rhys factor
Γ_{inh}	inhomogeneous broadening
LIF	laser induced fluorescence
NPHB	nonphotochemical hole burning
PC	photosynthetic complexes
PHB	photochemical hole burning
PSB	phonon side band
PS I	Photosystem I

PS II	Photosystem II
RC	reaction center
SDF	site distribution functions
SHB	spectral hole-burning
T	temperature
ZPL	zero-phonon line
ZPH	zero-phonon hole
MLS	Multi level system
NADP+	Nicotinamide Adenine Dinucleotide Phosphate
TLS	Two-Level system
HGK	Hole Growth Kinetics
SDF	Side disrtribution function

INTRODUCTION

Photosynthetic pigment-protein complexes are responsible for the primary light-induced steps of photosynthesis, the collection of photophysical, photochemical and biochemical reactions responsible for life on Earth. The effectiveness of these reactions approaches 100%. Photosynthetic complexes are networks of pigment molecules, optimized for maximal performance. Studying the energy transfer processes in photosynthetic complexes one can obtain a lot of information useful, for example, for development of new photovoltaic devices. Unfortunately, the information on energy transfer rates is hidden and not so easily accessible by optical/spectroscopic methods due to large inhomogeneous broadening exhibited by the spectra of photosynthetic complexes. Spectral Hole Burning (SHB) and other high-resolution frequency domain experiments have the ability to measure the homogeneous line widths which are inversely proportional to the excited state lifetimes. The above mentioned large inhomogeneous broadening is a consequence of static energy disorder (the environment of structurally similar pigments varies slightly from complex to complex due to amorphous nature of the protein). Another consequence is the distribution of donor-acceptor energy gaps, and respective distribution of energy transfer rates (or times).

Traditionally, only one lifetime (τ_{esl}) is obtained from the width (FWHM) of a spectral hole, but since both ZPL width and the SHB yield depend on the lifetime, SHB has an established pattern of preferentially probing the longer-lifetime (narrower line width) end of the lifetime distribution, if such distribution is present. Such tendency is definitely

present for protein-chlorophyll light-harvesting complexes. Although qualitatively it is well known that SHB preferentially probes the slow-rate end of the distribution, this effect has not been explored quantitatively. In particular, it has not been discussed which errors are introduced by failing to give proper attention to the EET rate distributions while interpreting the results of the SHB experiments in various systems. The present manuscript attempts such discussion.

An even broader question may be asked: Can one reliably establish, from the SHB data, the entire EET time distribution at given wavelength? If so, the data could then be compared to theoretical predictions based on structure, which, in turn, could produce even more information on transition energies in the absence of inter-pigment interactions (more simply – "site energies"), couplings of different chlorophylls, and improved overall understanding of light-harvesting antennae. Calculations of optical spectra and EET rates between chlorophyll molecules in various pigment-protein photosynthetic complexes became likely after the structures of these complexes were established at high enough resolution using X-ray crystallography. Structure-based calculations were performed for cyanobacterial Photosystem I and Photosystem II, and LH2 antenna complex of purple bacteria, as well as for other complexes. Such simulations produced significant results as for plausible origins of lowest-energy antenna states, trapping times, EET times, etc. However, further comparisons between the theory and experiment are needed to refine the parameters of such calculations – specifically the sets of both inter-pigment coupling energies and the site energies. The conflicting information on these parameters has to date impeded the progress in matching the features of calculated and experimental spectra in most of the photosynthetic complexes.

It could be argued that, when performed on a sufficiently large number of complexes, single molecule spectroscopy (SMS) is competent to deliver the information desired on the EET rate distributions. Practically speaking, however, low-temperature SMS experiments on photosynthetic complexes are relatively tricky to perform, and one often cannot be sure that SMS results are without systematic distortions that come from specific sample preparation procedures (i.e. the sum of the many LH2 single complex spectra from does not yield the bulk excitation spectrum which may indicate that in SMS samples the LH2 complex is not in the same local environment as in the bulk). Additionally, small light-induced fluctuations of position of spectral lines systematically affect the results of SMS experiments, making the line width averages larger than those corresponding to the results of SHB and even of the time-domain measurements. It goes without saying that the distributions of EET times should manifest also in the time-domain experiment but the methodology of extracting lifetime distributions from time-domain results is not developed any better than for frequency-domain approaches, and the usual practice is to fit the results with minimal possible number of decay exponents.

In summary, it would be interesting to investigate if it is possible to develop a reliable system of extracting EET rate distributions from the SHB data. To achieve this goal, one must learn to disentangle the effects of the EET rate distributions and other factors affecting the shape of the hole spectra and their evolution – something that has not yet been explored too deeply. This study provides the background necessary to engage in fitting the results of spectral hole burning experiments (whole hole shape evolution experiments and hole burning kinetics measurements) in photosynthetic complexes to determine the EET rate distributions.

Chapter 1

INTRODUCTION TO PHOTOSYNTHESIS

1.1. History of Photosynthesis Research

Flemish physician van Helmont (early 17th century) once grew a willow tree in a bucket of soil using only rain water to feed the soil. Five years later, though the amount of soil in the bucket had not significantly diminished, the tree was massive. Van Helmont came to the conclusion that it was the rain water that wet the soil that fed the tree and made it so massive. The book *Vegetable Statics* (published by English botanist Stephen Hales in 1727) made a claim that plants used mainly air as the nutrient during their growth. Later in the same century, English chemist Joseph Priestly (a discoverer of oxygen) ran experiments on respiration and combustion and arrived at the conclusion that green plants had an ability to reverse the effects of the respiratory processes of animals on the atmosphere. One experiment involved burning a candle in an enclosed volume of air. The resulting air could no longer support burning, and the mouse that had been kept in the residual air died. At the same time, a green branch of mint lived on in residual air for weeks. At the end of this period, Priestley found that a candle could burn in the reactivated air and a mouse could breathe in it. Now, we know that the burning candle used up all the oxygen in the enclosed air, but the oxygen was replenished by photosynthesis (due to the presence of the green

mint branch). In 1779, Dutch physician, Jan Ingenhousz, discovered that it is only in sunlight that plants produce oxygen and that, even in sunlight, the principle only applies to green parts of the plant. In 1782, Swiss minister Senebier concurred with Ingenhousz' findings and further observed that plants used carbon dioxide 'dissolved in water' as nourishment. Next milestones in the history of photosynthesis were made in the early nineteenth century. Another Swiss scholar, de Saussure, examined the quantitative relationships between the amount of organic matter and O_2 produced and the CO_2 taken up by a plant, coming to the conclusion that, during the assimilation of CO_2, water was also consumed by the plants. In 1817, two French chemists, Pelletier and Caventou, isolated the green substance of a plant and named such substance "chlorophyll", and in 1845, a German physician, Mayer, discovered that plants can transform energy of sunlight into chemical energy. By the mid-1800s, the phenomenon of photosynthesis could be represented as follows:

$$CO_2+H_2O+\text{LIGHT} \_\_\_\_\_ O_2 +\text{ORGANIC MATTER}$$

French plant physiologist Boussingault conducted accurate determinations of the ratio of CO_2 converted to O_2 during photosynthesis. In 1864, Boussingault found that the photosynthetic ratio – the volume of O_2 evolved to the volume of CO_2 used up – is almost unity. In the 1880s, several experiments by German botanist, Engelmann, using green alga *Spirogyra* revealed a correspondence between the absorption spectrum of the chlorophyll and the action spectrum of photosynthesis and a direct connection between O_2 evolution and chloroplasts of green leaves. These experiments convinced Engelmann that these are the chlorophylls which are the active photoreceptive pigments for photosynthesis. At the

beginning of the 20th century, the state of our knowledge of photosynthesis could be represented as follows:

$$(CO_2)_n + H_2O + \text{light} \_\_\_\_\_ (O_2)_n + \text{carbohydrates.}$$

It was unclear whether the source of O_2 was water or CO_2. British plant physiologist Blackman (circa 1905) suggested that the photosynthesis is a two-step mechanism including photochemical (light) reactions and non-photochemical (dark) reactions. The enzymatic non-photochemical reaction is slower than the photochemical reaction and therefore at brighter light intensities, the rate of photosynthesis is only dependent upon the rate of the non-photochemical reaction. Note that, with multiple steps, non-photochemical reaction can proceed both in light and in dark. By using flash illuminations lasting fractions of a second, the photochemical and non-photochemical reactions can be separated. Light flashes lasting less than a millisecond (10^{-3}) were used at that time. Dutch-born microbiologist Cornelius van Niel proposed that the plant-produced oxygen evolved during photosynthesis comes not from carbon dioxide, but from water. Now, we know that van Niel was correct in his hypothesis and such insight has been a major contribution to our modern understanding of photosynthesis. The overall equation of photosynthesis for green plants is:

$$6CO_2 + 6H_2O + \text{Energy} = C_6H_{12}O_6 + 6O_2$$

Next steps in photosynthesis research, relevant for the subject of this thesis, will be discussed in more details in the next sections.

1.2 Definition of photosynthesis

Photosynthesis can be defined as a metabolic process that changes light energy, mainly sunlight, into chemical energy. This process is carried out by many organisms from plants and algae to photosynthetic bacteria. The best known form of photosynthesis is the oxygenic one carried out by higher plants and algae, as well as by cyanobacteria. There are four main phases to the intricate process described by the above equation for photosynthesis: (1) light absorption and energy delivery by antenna systems, (2) primary electron transfer in the reaction centers (RC), (3) energy stabilization by secondary electron transfer, and (4) synthesis and transport of stable sugar products [1]. Phase 1 is a photophysical process, Phases 2 and 3 are photochemical processes, and Phase 4 is a biochemical process. We will make Phases 1 and 2 our main focus in the present thesis, the photophysical and initial photochemical processes in photosynthetic complexes. We often refer to Phases 1 and 2 as the early events of photosynthesis since they occur on extremely fast timescales (10^{-15} to 10^{-3} s) [2, 3]. Both antenna system pigment complexes and RCs are made up of chlorophyll-like molecules, as well as caratenoids (details on the structures of pigment molecules will be presented in section 1.3).

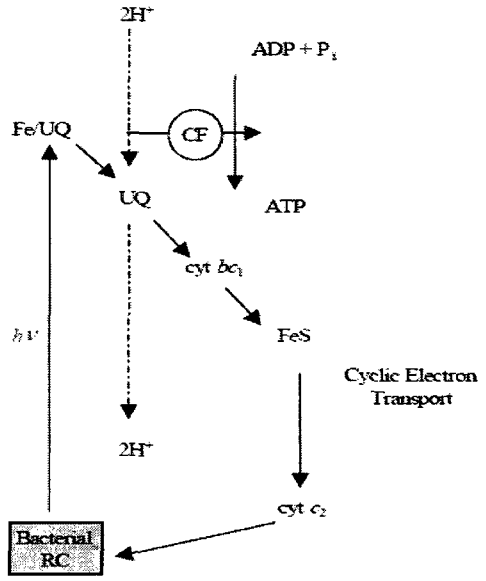

Figure 1.1. Schematic of cyclic phosphorylation in purple bacteria . After the bacterial RC is excited by light (hv), primary electron transfer to an iron-ubiquinone complex (Fe/UQ) occurs. The electron leaves the RC through transfer to a ubiquinone (UQ) and travels to cyctochromes bc_1 (cyt bc_1), to cytochromes c_2 (cyt c_2), and finally back to reduce the RC, completing the electron transfer cycle. In the meantime, the electron transfer across the bacterial membrane through UQ creates a proton gradient driving ATP synthesis. From [5]

There exist two distinct mechanisms of photosynthesis: (i) non-cyclic phosphorylation or (ii) cyclic phosphorylation (phosphorylation in this sense means the light driven synthesis of ATP from adenine diphosphate (ADP) and phosphate (Pi) [4], which is contributed by the primary electron transfer process). Only one of such mechanisms is needed for the process to occur. Cyclic phosphorlylation occurs in green sulfur and purple bacteria and is anoxygenic [1]. Non-cyclic phosphorylation occurs in cyanobacteria and higher plants and is oxygenic. Cyanobacteria and plants can, however, experience cyclic phosphorylation when they are too low in energy to run non-cyclic

phosphorylation. Figures 1 and 2 outline the differences between cyclic and non-cyclic phosphorylation.

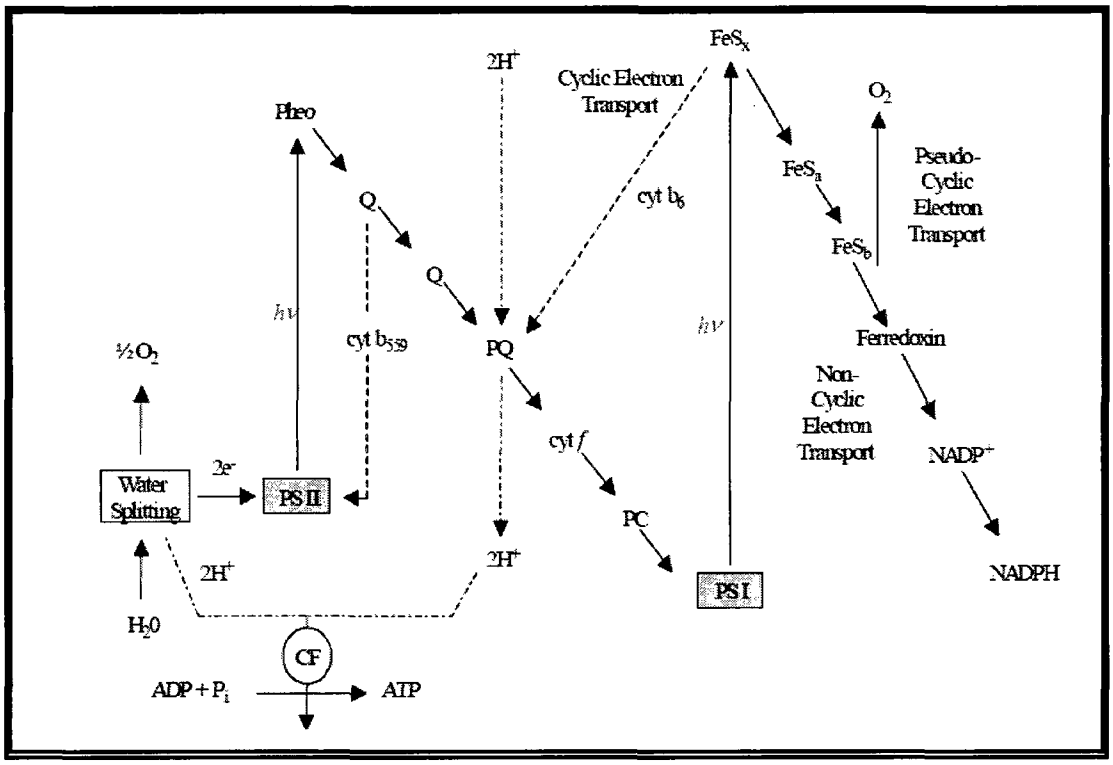

Figure 1.2. Schematic of non-cyclic phosphorylation in cyanobacteria and plants. Primary electron transfer to pheophytin (Pheo) occurs when the PS II RC is excited by light (hv) and the electron is then passed down to quinones (Q), a plastiquinone (PQ), cytochrome f (cyt f), and to plastocyanin (PC). After excitation, the Photosystem I (PS I) RC transfers an electron to a series of iron-sulfur complexes (FeS_x, FeS_a, FeS_b) and PS I is reduced by PC. This is followed by a reduction of FeS_b by NADP reductase (NADP+), which leads to the synthesis of NADPH and is used in the Calvin cycle. H_2O (generating O_2) and cytochrome b559 (cyt b559) reduces the PS II RC. Electron transfer across the thylakoid membrane creates a proton gradient, which drives ATP synthesis. If the organism is too low in NADPH to synthesize sugars, cyclic phosphorylation takes place. Then electron transfer from FeS_x to cytochrome b_6 (cyt b_6) takes place, ensuring that the PS I RC is reduced. From [5]

Simply put, in cyclic phosphorylation, the electron removed from the reaction center returns to re-reduce it. In non-cyclic phosphorylation, the electrons are not recycled and electrons must be obtained from an outside source (e.g. H_2O) to re-reduce the oxidized reaction center. Another difference between non-cyclic phosphorylation and cyclic phosphorylation is that a reducing compound, nicotinamide adenine dinucleotide phosphate (NADPH), is produced along with ATP in case of non-cyclic phosphorylation. The Phase 4 of photosynthesis (see above) uses the ATP and NADPH generated by Phase 3 in carbon fixation, generating sugars that the organism can use for energy. These are known as the dark reactions of photosynthesis because they can take place in the absence of light due the fact that the ATP and NADPH have already been generated by light reactions of photosynthesis. The dark reactions are referred to as the "Calvin, Basshan, and Besson cycle", or just Calvin cycle [2-5] in oxygenic organisms, named for the researchers who determined the chemistry of these enzymatic reactions. The Calvin cycle causes a CO_2 fixation into carbohydrates in oxygenic organisms. In the case of anoxygenic organisms, the Calvin cycle occurs in purple bacteria, but reverse tricarboxylic acid cycle (TCA) is used for carbon fixation [5] in green sulphur bacteria.

The two different mechanisms of photosynthesis are a reflection of variations in the morphology of photosynthetic organisms, which evolved from single celled prokaryotic bacteria to the complex multi-cellular biological structures of plants (eukaryotic organisms). There are three groups of prokaryotic organisms: cyanobacteria, photosynthetic bacteria, and Prochlorophyta where the photosynthetic machinery is most simple. Prochlorophyta and Cyanobacteria [1, 5] contain chlorophyll *a* and *b* and evolve oxygen

(same process is present in green plants). Photosynthetic bacteria use carbon, nitrogen, and sulphur compounds as the reductant source (anoxygenic) and are made up of two subgroups: Chlorobiineae and Rhodospirillineae [1,5]. Chlorobiineae, green sulphur bacteria, use sulphur compounds as electron donors (only one species, *Chloroflexus aurantiacus*, uses CO_2 along with S_2^- as reductants) and contain bacteriochlorophyll *a*, *c*, *d*, and *e*. Rhodospirillineae, purple bacteria, may use sulphur, nitrogen and carbon as electron donors and contain bacteriochlorophyll *a* and *b*. In prokaryotes light driven reactions of photosynthesis take place in the cellular membrane, as there are no organelles in all prokaryotes.

In eukaryotic organisms (i.e. plants and algae), the architecture of photosynthesis is much more advanced [1,5,6]. All eukaryotes are oxygenic and contain chlorophyll *a* and *b*. Photosynthesis takes place in organelles called chloroplasts. Speculation has been made that chloroplasts evolved from the Prochlorophyta bacteria, *Prochloron* [5]. Chloroplasts have a double membrane surrounding an internal membrane network. This internal membrane provides the chloroplasts with a large volume and surface area, causing a very high energy output. The internal membrane also has the chloroplast envelope, which are folds containing a liquid, the stroma, and stacks of inner membrane discs or thylakoids (Figure 1.3).

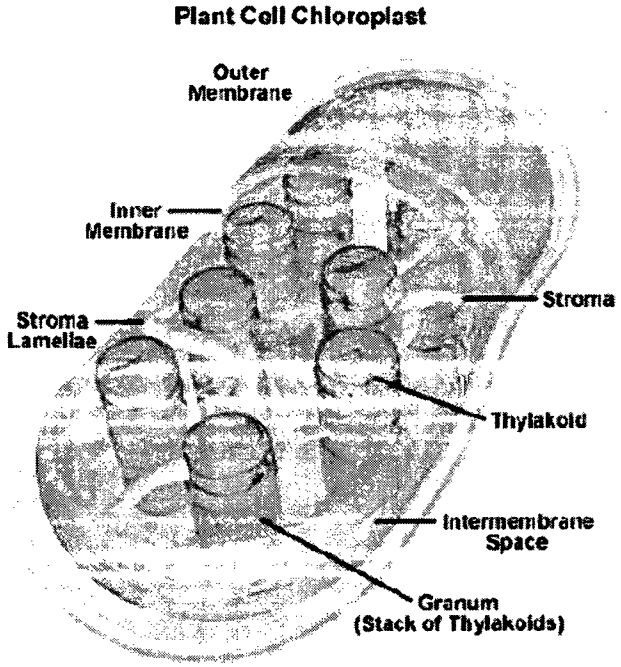

Figure 1.3: The structure of a chloroplast. From http:// micro.magnet.fsu.edu

Stacks of these thylakoids are known as grana. The thylakoid membranes store all pigment protein complexes needed for the light dependent reactions of photosynthesis. It is the stroma where the dark reactions of photosynthesis occur. As discussed above, primary processes of photosynthesis occur in special pigment-protein complexes, or photosynthetic complexes (PS complexes); more details on their structure will be presented in subsequent sections. The mutual arrangement of the protein complexes in oxygenic photosynthesis is depicted in Figure 4. One can compare this figure with Figure 2 to determine the contributions of various complexes to different steps of photosynthesis.

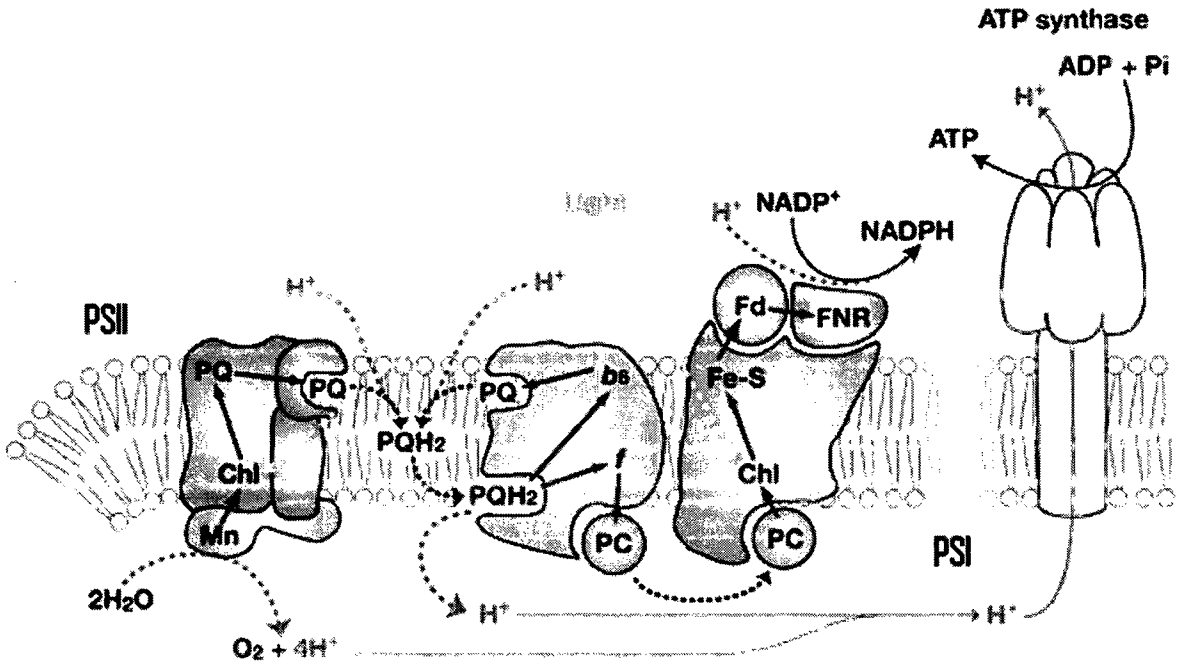

Figure 1.4: The electron transport system of oxygenic photosynthesis consists of three membrane spanning protein complexes, i.e., PS II, Cytochrome b_6f (Cyt b_6f) and PS I. PS II complexes oxidize water with light energy. When PS II is excited by four photons, the complex draws four electrons out of two molecules of water, and one oxygen molecule evolves. Such oxygen evolution occurs in the special subunit of PS II complex, "oxygen evolving subunit," containing four manganese atoms. An electron out of water is carried to a fat-soluble electron carrier, plastoquinone (PQ), in PS II (electron flow is indicated by blue arrows). The PQ in receipt of the two electrons gets two protons (H+) near by the membrane surface (the reduced PQ is shown as PQH_2), and carries protons and electrons to Cyt b_6f complex (the uptake and release of protons are indicated by red broken lines). Cyt b_6f complex carries the electrons to plastocyanin (PC), a water-soluble copper-protein. PC transfers the electrons from Cyt b_6f complex to Photosystem I (PS I). Another Chlorophyll-containing complex that runs on light is PS I, which pumps an electron to ferredoxin (Fd). Finally, the electrons are delivered to NADP+ via ferredoxin-NADP+ redactase (FNR) effecting NADPH. While electrons are delivered among three complexes, the proton

gradient forms between the membrane. The difference of proton concentrate will be a motivating force for production of ATPs by ATP synthase. Image by Satoshi Hanada.

1.3 The Photosynthetic Pigments

Photosynthetic complexes are made up of chlorophyll-like molecules including chlorophyll *a* and *b*, bacteriochlorophylls, pheophytin *a* and *b*, and other kinds of pigment molecules, e.g. carotenoid α and β, xanthophylls, which capture solar radiation (chemical structures are depicted in Figure 1.5 [1-4]. Because the $S_1 \leftarrow S_0$ transitions for these molecules range from ~ 450 nm to 900 nm, light is collected from the solar spectrum over a broad wavelength range [1-4].

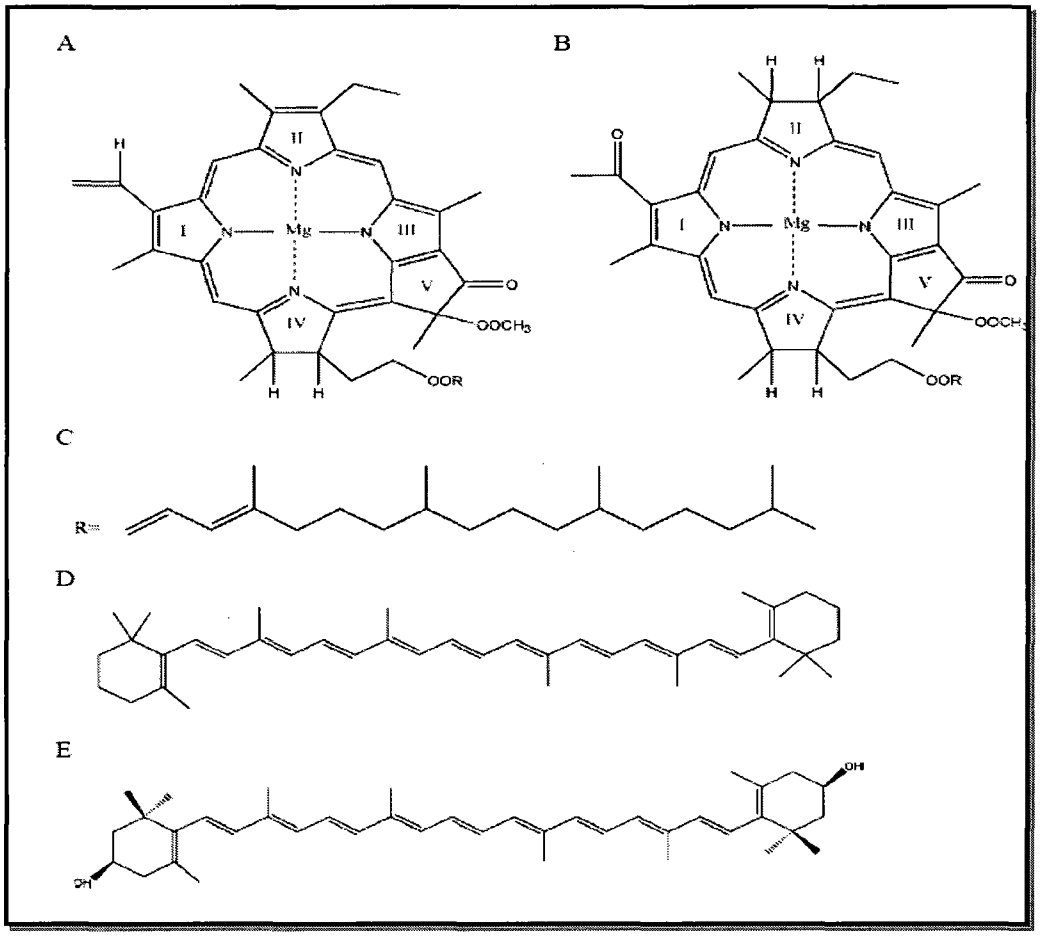

Figure 1.5: Chemical structures of (A) chlorophyll and (B) bacteriochlorophyll, with (C) being the phytyl tail; (D) beta-carotene, a carotenoid of photosystem II (PS II) which is responsible for quenching singlet states and preventing oxidation to the PS II RC, and (E) zeaxanthin, a xanthophyll which is an oxidized hydroxy derivative of beta-carotene, that is responsible for quenching reactive oxygen species in cyanobacterial and plant photosynthetic organisms. The Roman numbers I to V label the Chl and BChl rings according to the IUPAC nomenclature system. The structures of pheophytin and bacteriopheophytin respectively are identical to chlorophyll and bacteriochlorophyll, except that the central Mg atom is replaced with H atoms bonded to rings I and III.

Energy collected by the antenna complexes is transferred downward, as in a funnel, to lower-lying, chlorophyll-containing reaction center pigment complexes (see Figure 1.6). (Pigments and protein involved with primary electron transfer together are known as the reaction center, RC). It is well-known that the number of the reaction centers in the photosynthetic organisms is significantly smaller than the number of pigment molecules. Thus, most of the pigments function as antenna. Excitation energy forms an excited electronic state with a very high redox potential (usually ~ 0.4 to 1.1 V) [1,5] when transferred to a RC, and the respective pigment can therefore donate its electron to a lower-energy molecule (for example, a pheophytin in PS II), and as a result a primary charge separated state is formed. Put together, the initial charge separation events and light harvesting are very efficient and yield nearly 100% quantum efficiency (charge separation events per photons absorbed) [1]. In Phase 3 of photosynthesis (see previous subsection), the primary charge-separated state created by the reaction center is stabilized by further electron transfer along a chain that is coupled to a mechanism which can store energy in a chemical form (e.g. adenine triphosphate (ATP) synthase).

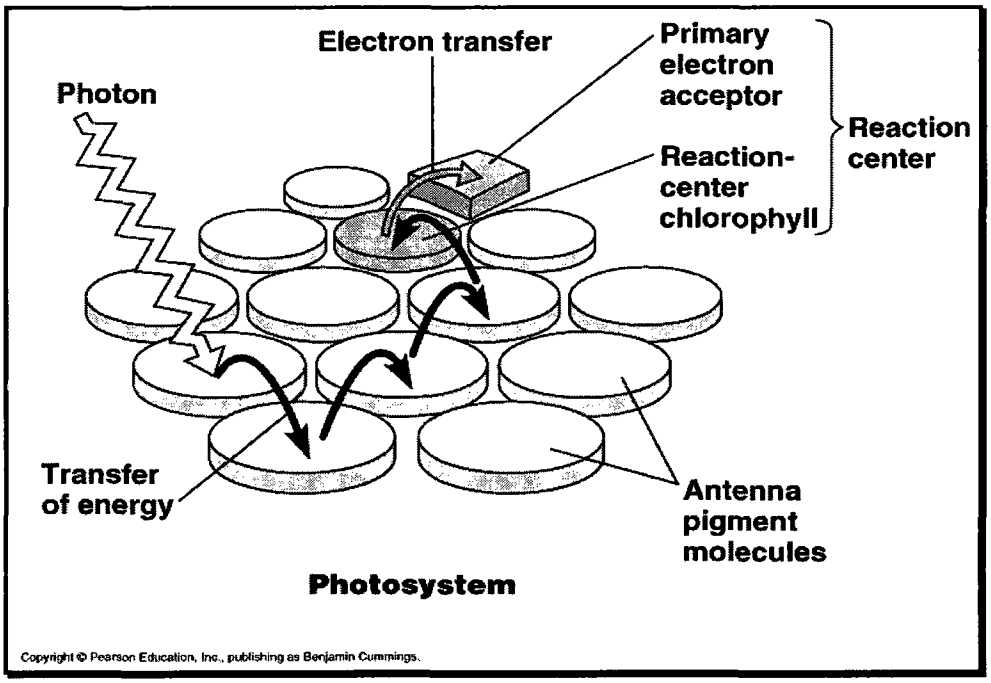

Figure 1.6. Schematic of light harvesting, energy transfer through antenna pigment molecules and transfer to the reaction center, where primary electron transfer (e.g. charge separation) is initiated. © Imperial College London.

1.3.1 The chlorophylls

Chlorophylls and their derivatives play an important role in the light absorption and energy transduction processes of photosythesis. Generally, complexes with proteins are formed except the chlorosomes of the green photosynthetic bacteria containing large BChl *c* aggregates. Chlorophyll molecules are arranged in the pigment-protein complexes (e.g. PSI, PSII, see Figure 1.4 above). In PS complexes chlorophylls have several functions, namely (1) the light harvesting (LH) antennas absorb light which is usually provided by sunlight. (2) ensuring the minimal loss of energy while transferring the excitation energy to

the reaction centers (RCs); where (3) they act as primary electron donors and acceptors in light-induced charge separation across the photosynthetic membrane.

In principle, in oxygenic photosynthesis, there are two most widespread types of chlorophylls, chlorophylls *a* and *b* as described below. *Chlorophyll a* is found in all known eukaryotic photosynthetic organisms and is thus suspected to be the most abundant large organic molecule on Earth. Among prokaryotes, it is found in large quantities only in the cyanobacteria (including the prochlorophytes). Traces of minor variants of chlorophyll *a* are found in some anoxygenic bacteria, the green sulfur bacteria and heliobacteria, where it functions as an intermediate in the electron transport chain. The only difference between chlorophylls *a* and *b* is in the composition of a side-chain (in chlorophyll *a* it is $-CH_3$, in chlorophyll *b* it is CHO). Chlorophyll *c* does not have ring D reduced and it does not have a phytyl tail, Chlorophyll *c* is not a 'chlorin' but more like a 'porphyrin'. Consequently, its Q_y extinction coefficient is weak. Chlorophyll *c* is found exclusively in marine algae like diatoms and dinoflagellates. It appears in LHCII-like antenna complexes (see below) and transfers energy to chlorophyll *a*. The only one difference between chlorophyll *d* and chlorophyll *a* is the substituent at the C-3 position which is a formyl group in chlorophyll *d*, and a vinyl group in chlorophyll *a*. $C_{55}H_{72}N_4O_5Mg$ is the chemical formula for chlorophylls *a* and *b*. All of these chlorophylls contain a network of alternating single and double bonds, Figure 1.7.

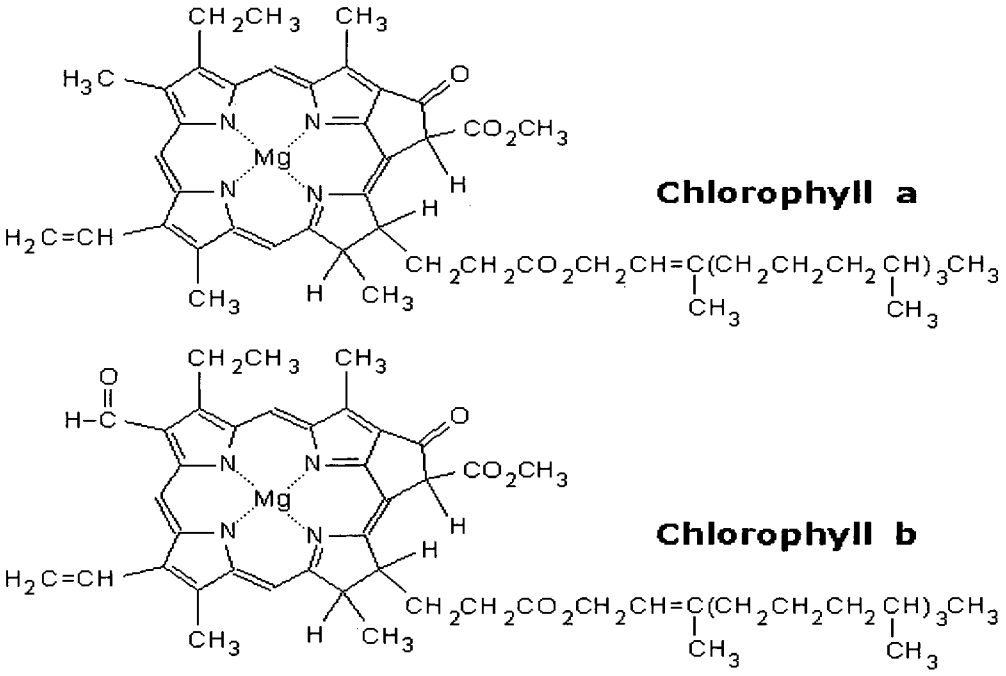

Figure 1.7: Chlorophylls *a* and *b* chemical structures. The size of the ring is about 1 nm, it is a planar molecule. A Mg atom in the center of the planar part is coordinated to four N-atoms. Each nitrogen is part of a substructural element of the molecule that comes from pyrrole, a cyclic compound with a nitrogen atom in a five-member ring with four carbons. From http://www.food-info.net/uk/colour/chlorophyll.htm

The two chlorophylls allow the plant to absorb the energy from the sunlight at somewhat different wavelengths, so the light wavelength that is not absorbed by chlorophyll *a*, will instead be absorbed by chlorophyll *b*. Chlorophyll *a* has approximate absorbance maxima of 430 nm and 662 nm, while chlorophyll b has approximate maxima of 453 nm and 642 nm in organic solvents at room temperature. Plants can obtain their energy from the blue and red parts of the spectrum, however, there is still a large spectral region, between 500-600 nm as shown in Figure 1.8 where very little light is absorbed giving the plant its green

color. In general all chlorophylls display two major absorption bands: one in the blue or near UV region and one in the red or near IR region. These absorption bands arise from $\pi \rightarrow \pi^*$ transitions, involving the electrons in the conjugated π system of the chlorin macrocycle.

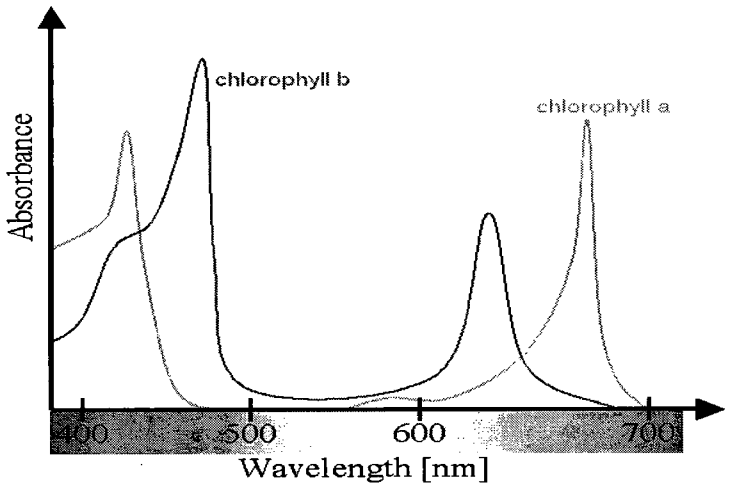

Figure 1.8: Absorbance spectra of chlorophyll *a* (green) and *b* (red) in an organic solvent (in the absence of protein). The spectra of chlorophyll molecules in PS complexes are slightly shifted depending on specific pigment-protein interactions. Image from http://www.answers.com/topic/chlorophyll

Another class of the photosynthetic pigments is *bacteriachlorophylls* [1-5], see also Figure 1.5B, that can be found in non-oxygenic phototrophic bacteria. These bacteria don't

produce oxygen as a product of photosynthesis, unlike plants; they also use wavelengths of light that are not absorbed by plants, with Q_y transitions in 800-900 nm region.

1.3.2 Carotenoids

Carotenoids are found in many non-photosynthetic organisms and in all known photosynthetic organisms. There are some consistent features that are common to most photosynthetic carotenoids. They rapidly quench triplet excited states of chlorophylls before they can react with oxygen to form the highly reactive and damaging excited singlet state of oxygen (singlet oxygen). Moreover, carotenoids also quench the singlet oxygen if it is still formed. Also, carotenoids are involved in the regulation of energy transfer in the antennas. This process, connected to the 'xantophyll cycle', avoids over-excitation of the photosystem II reaction center by allowing the light-harvesting system to switch to a state where excitations are no longer delivered to the RC but, instead, are broken down into heat. In light-harvesting, carotenoids are absorbing photons in the 400-500 nm regions and transferring the energy to (bacterio-)chlorophylls. (They are responsible for red and yellow colors of the autumn leafs; carotenoid colors become visible after chlorophylls get photobleached by the Sun over the summer.) The first excitation energy transfer process to be quantitatively measured (by Duysens in the 1950s) was the energy transfer from spirilloxanthin to bacteriochlorophyll in the LH1 antenna of the purple photosynthetic bacterium Rhodospirillum rubrum Finaly, carotenoids have a structural role. In the major

plant light harvesting complex (LHC II), the two central luteins form an essential element in the structure of the whole complex.

1.4. Photosystems and Reaction centers

The Figure 1.4 above represented a fraction of a thylakoid membrane with the key components of the electron transfer chain. Although the existence of the pigment-protein complexes was discovered long time ago, the exact information on their structure, necessary to explain their optical properties and the details of energy and electron transfer, was not available until recently. The first PS complex for which the structural data became available was the reaction center of purple photosynthetic bacteria [7]. (X-ray diffraction on protein crystals is used to determine their structure at a resolution of several Å. This resolution is sufficient to determine not only positions but also the orientations of the pigment molecules and allows performing comparisons between experimental and modeling studies,) Reaction centers exist in all green plants as well as in bacteria and algae and all exhibit relatively similar structure. In green plants the reaction centers are parts of the complex structures of Photosystem I and Photosystem II. The reaction centers that are found in purple bacteria (e.g. *Rhodopseudomonas*) are most easily isolated, which makes them better understandable than those in green plants.

1.4.1. Photosystem II

Photosystem II (PS II) is one of the two large supramolecular pigment-protein complexes embedded in the thylakoid membranes of green plants, algae, and cyanobacteria. PS II splits water into protons, electrons and releases oxygen [8-11], by

using sunlight. It contains the redox-active reaction center built into the D1 and D2 proteins. Six chlorophyll *a* molecules, two pheophytin *a* molecules, two β-carotenes, and one cytochrome *b*559 are supported by D1 and D2 proteins and are considered the reaction center [8-11]. The structure of PS II is schematically presented in Figure 1.9.

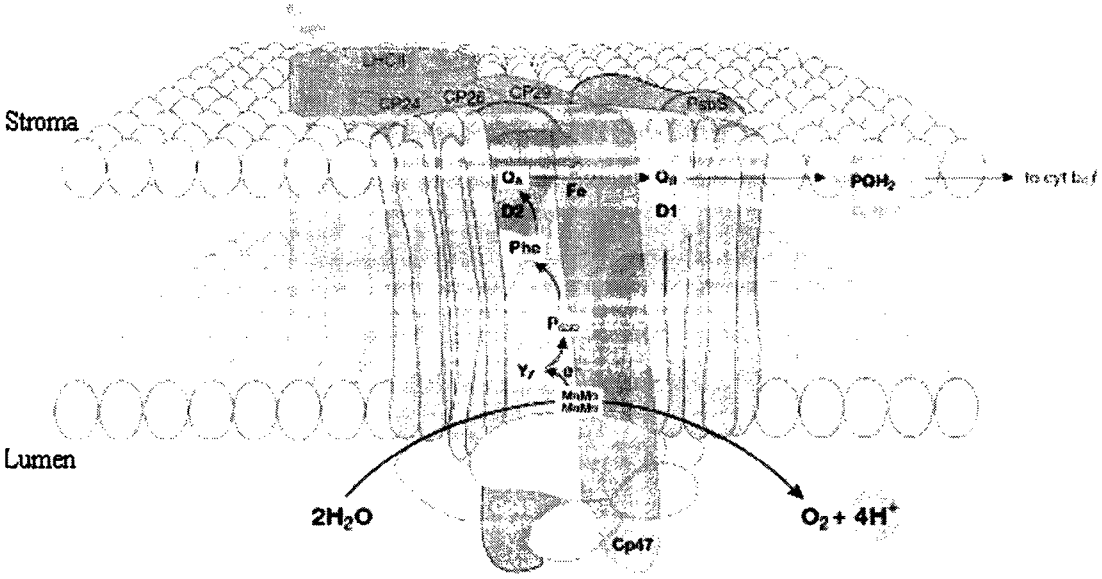

Figure 1.9 Organization of photosystem II and light-harvesting complex II in the thylakoid membrane. CP43, CP47: internal antenna chlorophyll–protein complexes. D1, D2: main components of reaction center (RC) with binding sites for electron acceptor quinones (Q_B, Q_A). P_{680}: chlorophyll special pair. Other cofactors associated with D1/D2: pheophytin (Phe), non-haem iron (Fe), Mn-cluster. Accessory chlorophylls and β-carotene are not shown. Chl, chlorophyll; PQH_2, plastoquinone pool; cytb6f, cytochrome b_6f complex; Y_Z, D1-Tyr161. For a more detailed description, see [9]. Image by J. Nield (Imperial College London, UK)

The absorption of one photon by Photosystem II removes one electron from the P680 group of chlorophylls and charge separation reaction leads to the formation of the primary radical pair P_{680}^{+} $Pheo^{-}$ [12]. Then, a secondary charge transfer reaction happens involving the plastoquinones (Q_A and Q_B), which results in P_{680}^{+} Q_A^{-} and then P_{680}^{+} Q_B^{-} formation [12,13]. With its resulting positive charge, $P680^{+}$ is sufficiently electronegative that it can remove one electron from a molecule of water. When these steps have occurred 4 times, requiring 2 molecules of water (H_2O), one molecule of oxygen and four protons (H+) are released. The P680 is in fact a weakly coupled multimer of four chlorophyll and two pheophytin molecules [14]. The electrons are eventually transferred to the cytochrome b_6/f (see Figure 1.4).

Approximately 250 molecules of chlorophyll surround the reaction center in higher plants; functioning as antennae by absorbing photons and allowing the energy transfer to the reaction center. All oxygenic photosynthetic organisms contain equal amounts of the two core antenna complexes CP43 and CP47 and the D1/D2/Cyt b559 RC. (In the Figure 1.9 the CP43 and CP47 complexes are located on both sides of the RC.) O_2-evolving PSII core complexes are made up of an assembly of these three pigment-protein complexes along with the extrinsic 17-, 23-, and 33-kDa proteins. It is easier to remove the CP43 complex from the PSII than CP47.

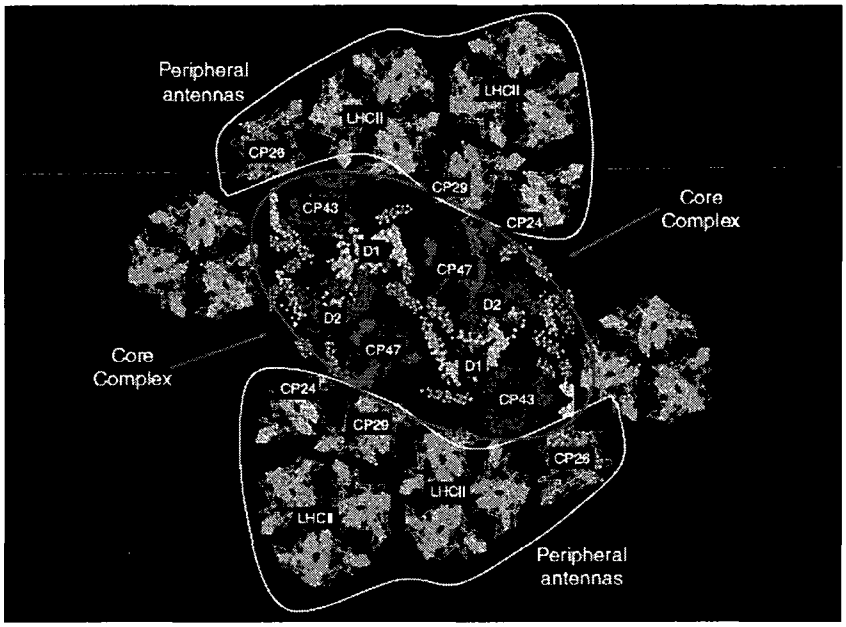

Figure 1.10. The overall structure of plant Photosystem II. (Image by Roberto Rossi)

The outer antenna consists of chlorophyll *a/b* binding proteins, which contain most of the light-harvesting pigments of PS II. These proteins, of which the trimeric light-harvesting complex II (LHC II) is the most abundant PS complex in Nature, are required not only for the transfer of excitation energy to the RC and the efficient absorption of light, but they also play essential roles in various regulation mechanisms of the photosynthesis process under light-saturating conditions, such as state transitions and nonphotochemical quenching. The overall quantum efficiency of the charge separation process relies upon the relative rate constants of various processes (including excitation energy transfer (EET) from chlorophylls in the light-harvesting antenna to the chlorophylls in the RC that perform the CS; CS and charge recombination in the RC; stabilization of the CS by secondary

electron transfer (ET); and trivial relaxation or loss processes of the excited state: intersystem crossing, internal conversion, and fluorescence.)

1.4.2. Photosystem I

The activation of P700 in Photosystem I enables it to pick up electrons from the cytochrome b_6/f complex and raise them to a sufficiently high redox potential that, after passing through ferredoxin they eventually convert $NADP^+$ to NADPH. The photosystem I in green plants and cyanobacteria has a structure with 90 antenna chlorophyll (Chl) *a* molecules surrounding the six core Chl *a* molecules that function in the fast electron steps and 12 polypeptides with highly conserved amino acid sequences [6, 15-19]. PS I antenna structure, not just RC, shares some structural similarities with PS II which suggests a common evolutionary origin. However, the center of the PS II core has fewer pigments than PS I, likely as a protective measure against the high oxidative potential of PS II and the process of photo-damage, resulting in a lower quantum yield [20] in PS II as compared to PS I [21]. In cyanobacteria the PS I forms trimers in vivo. In case the environment is iron-deficient (and not enough iron-containing RCs can be formed) the trimer may become surrounded of additional antenna, consisting of IsiA proteins, similar to CP43 of the Photosystem II. In higher plants PS I is monomeric, with the PS I core accompanied by Lhca1...Lhca4 antenna complexes.

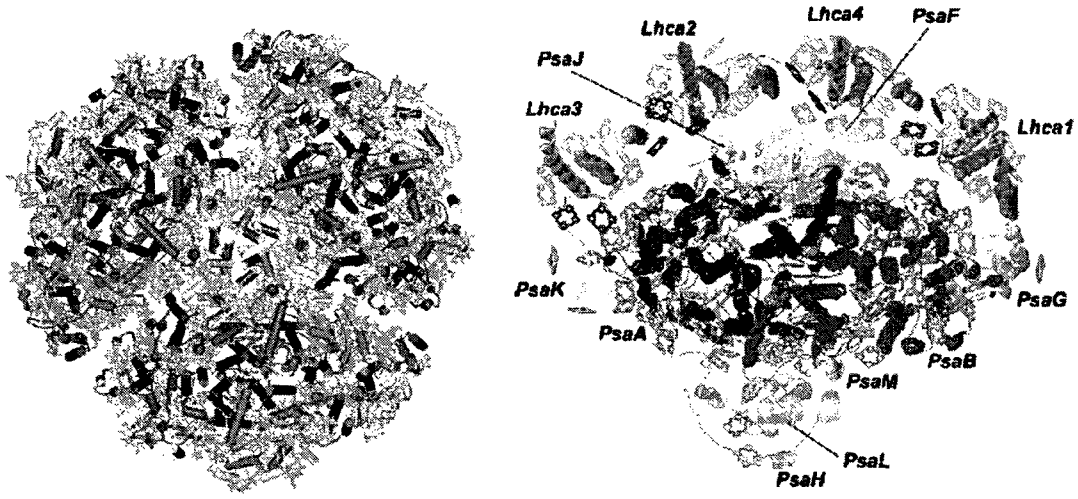

Figure 1.11: Cyanobacterial trimeric Photosystem I (left) and Plant Photosystem I (right). From [115].

Understanding the multiphasic complex process of photosynthesis has many significant scientific implications. A good understanding of photosynthesis and how it varies among different organisms is important from structural biological, biochemical, evolutionary, and genetic standpoints. A good understanding the physics of photosynthesis, especially the early events of light-harvesting, such as EET and electron transfer, is very important as a model for solar cell science and technology [22-27]. Finding data has practical applications for next generation photovoltaic devices, in either creating solar cells that mimic photosynthesis [24,25] or actually using photosynthetic complexes in bioengineered devices [26,27]. Many different techniques have been used in studying photosynthetic complexes, including a wide range of spectroscopy methods (e.g. Spectral Hole-Burning) and some biochemical and genetic techniques. More details on hole burning spectroscopy can be found in Chapter 2.

Chapter 2

HOLE BURNING SPECTROSCOPY AND ITS APPLICATIONS TO PHOTOSYNTHETIC COMPLEXES

2.1 Introduction

The parameters of interest in photosynthesis research by optical methods are energy and charge transfer times. These times determine the widths of the lines in the spectra of chlorophyll molecules in the PS complexes at low temperatures. Unfortunately this information is not immediately easily accessible. The optical spectra of photosynthetic pigment–protein complexes usually show broad absorption bands, often consisting of a number of overlapping, 'hidden' sub-bands belonging to different chlorophyll molecules in the complex structure. Spectral hole burning [28] is an ideal technique to unravel the optical and dynamic properties of such hidden species. The ability of a narrow bandwidth, high intensity laser light to remove a narrow homogenous line from an inhomogeneously broadened spectral band, causing the dip (hole) in the resultant spectrum, is used in the Hole-burning spectroscopy. The hole formation mechanism may be either photophysical or photochemical (see below). HB enables high resolution studies of biologically important

systems at low temperatures, which earlier could be explored only by low resolution spectroscopy [29-37]. For studying the S_1 (Q_y) excited-state electronic structure, excitation energy transfer (EET), and electron transfer (ET) dynamic of protein-chlorophyll complexes at low temperature, Spectral Hole Burning (SHB) is a powerful frequency-domain technique. In the following sections, the principles of spectral hole burning (HB) will be discussed in details.

2.2 Spectral Lineshape Theory

Absorption of a quantum of light energy, promoting an electron from a ground state (E_g) to a higher electronic energy level (E_{ex}) is involved in optical excitation of a molecule. Such excited molecule emits a photon or decays to the ground electronic state through radiationless process. The Heisenberg uncertainty principle (H.U.P.) must be satisfied as this excitation-decay process is quantum mechanical in nature. H.U.P. familiar form is given by:

$$\Delta x \Delta p \geq h / 2\pi \qquad (2.1)$$

where x represents the position of the electron, p represents its momentum, and h is the Planck's constant [47]. For optical processes, however, this relation may be recast in a more useful form

$$\Delta E \Delta t \geq h / 2\pi \qquad (2.2)$$

where E represents the energy of the excited electronic state and t represents the time the electron spends at this particular energy [38]. Thus, the energy cannot be precisely known when the electron is promoted to a higher quantum energy level. It also cannot be known exactly how much time this electron spends at this higher energy level. The accuracy of the information is sacrificed when trying to precisely determine either the energy or lifetime of a particular state. Therefore, the spectral lineshape of an optical transition is broadened (with respect to a delta function one would expect in the absence of H.U.P.), and this is known as *uncertainty or natural or homogeneous broadening* [39] (see Figure 2.1). The relationship between the excited state lifetime and the width of the respective spectral line γ may be expressed as

$$\gamma=1/\pi c T_2, \tag{2.3}$$

where γ is in cm^{-1} and c is speed of light in cm/s and T_2 is total dephasing time in seconds. Different contributions to T_2 will be discussed in the next subsection.

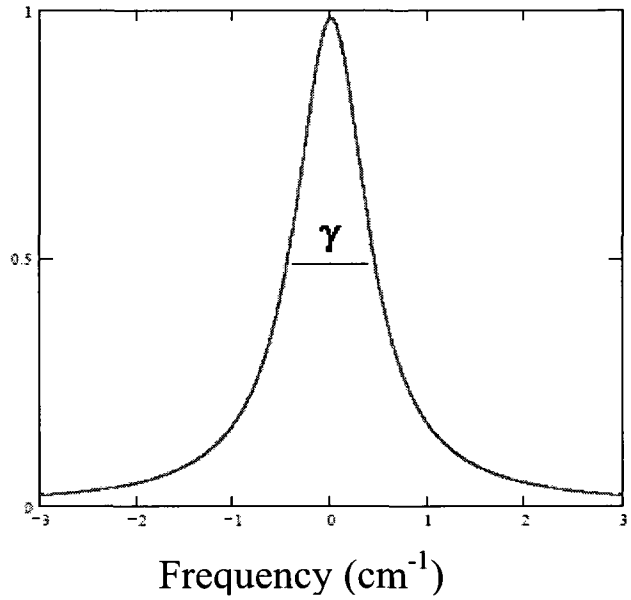

Figure 2.1 Natural or homogeneous shape of a spectral line [38]. The homogeneous profile is a Lorentzian and carries a full width at half maximum (FWHM) of $\gamma = 1/\pi cT_2$

2.3 Single Molecule Optical Spectrum in solid host-guest systems

The typical absorption band of the S_0-S_1 transition for pigment molecule embedded into solid is shown in Figure 2.2. The sharp zero-phonon transition with a width γ is accompanied at the high energy side by a sideband due to lattice phonons. Such line shape reflects the Franck-Condon principle as applied to lattice vibrations. The relative intensity α in the zero-phonon line (the Debye-Waller factor) is:

$$\alpha = I_{ZPL} / (I_{ZPL} + I_{PSB}) = \text{(intensity in zero-phonon line/total intensity)} \quad (2.4)$$

where I_{ZPL} and I_{PSB} are the relative integrated intensities of the ZPL and the PSB, respectively. At $T \sim 0$, $\alpha = exp(-S)$, where S is the dimensionless Stokes shift (also known as the Huang-Rhys factor). S can be used to characterize the strength of the electron-phonon coupling. In general, electron phonon coupling is weak when $S < 1$ (Figure 2.2a). For $S > 1$, the electron-phonon coupling is strong (see Figure 2.2b).

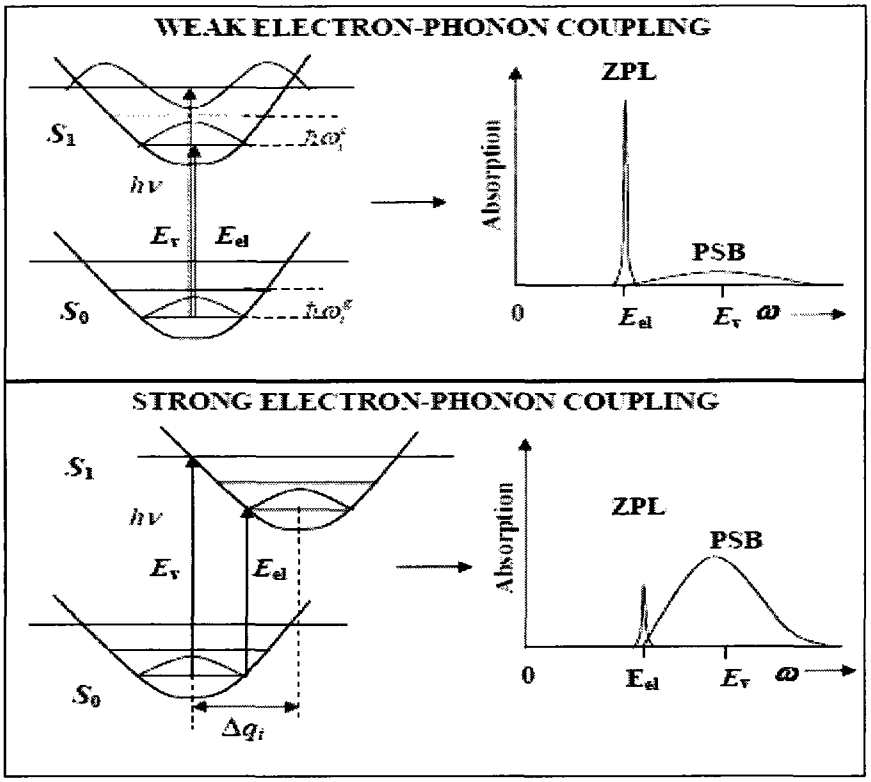

Figure 2.2. Schematic of the electron-phonon coupling of a guest impurity molecule in a low-T solid host matrix based on the Franck-Condon principle. A transition of the molecules from the ground electronic state, S_0, to the excited electronic state, S_1 after excitation at $h\nu$. The overlap between the ground and excited state vibrational

wavefunctions is determined by the lattice coordinate displacement, Δq, the most probable transitions are those for which the overlap is the largest. E_{el} and E_v represent the purely electronic and most likely transition energies, respectively. $h\omega_t^g$ and $h\omega_t^{ex}$ are the ground and excited state vibrational energy levels, respectively. From [40].

In the excited state, the charge distribution in the pigment molecule is different from that in the ground state. The lattice molecules sense the difference and adjust positions accordingly. This adjustment process can be represented as a superposition of lattice motions (e.g. phonons). Thus, electronic transition of the probe molecule gets coupled to the lattice phonons. Electronic relaxation is much slower than vibronic relaxation and the width of the pure electronic transition is much narrower than that of the associated phonon transitions at low temperatures. This is why the zero-phonon line is so prominent in the spectrum. As temperatures increase, the spectrum loses its characteristic features because (1) the Debye-Waller factor drops rapidly so that, for many systems, the intensity in the zero-phonon line is close to zero above 50 K; and (2) the width γ of the transition increases strongly as the temperature goes up. Due to this thermal broadening, the peak intensity of the ZPL drops. Both effects lead to a broad unstructured line shape at higher temperatures. As discussed above, the width γ is associated with a total dephasing time T_2, which in fact depends on temperature: $\gamma = 1/ c\pi T_2(T)$. T_2 represents the lifetime of the excited state coherence; its physical meaning is easily understood. If the ensemble of probe molecules is excited with a short pulse, the associated transition dipole moments will oscillate in phase for a while. Both lattice vibrations and decay to the ground state will destroy the coherence. Once T_2 has elapsed, just a fraction (1/*e*) of the initial ensemble is left coherently oscillating.

The width γ (or the time constant T_2) is made up of two rather different contributions (physically): contributions from the decay processes of the excited state population leading to a finite lifetime T_1 (so-called T_1 processes, energy relaxation); and contributions that come from the pure phase-destroying processes (known as T_2^* processes; they do not involve transition back to the ground state):]. At $T \neq 0$, the homogeneous line shape broadens because of dephasing processes that are induced by thermally activated phonon modes of the host matrix. Such dephasing is caused by quasi-elastic scattering of a phonon by the molecular impurity, which alters the phonon's direction of propagation and an insignificant change to its energy. Overall,

$$1/T_2(T) = 1/2T_1 + 1/T_2^*(T) \qquad (2.5)$$

As the temperature T approaches zero, T_2^* becomes infinitely long and the line width is determined solely by the energetic relaxation lifetime. In this limit, γ is known as the natural line width. In some limiting cases, like whenever dephasing processes can be neglected, it can be concluded that the lifetime of the excited state may be determined from the associated line width. Factor 2 in Eq. 2.5 appears because the lifetime of the ground state is infinitely long. In the case of PS complexes one should note that the characteristic times of the energy and charge transfer processes, which are of interest to us, are in the picosecond range. These time constants play the role of T_1 and correspond to the homogeneous line widths of several cm^{-1} (~100 GHz). For comparison, typical line widths resulting from pure dephasing are of the order of 1 GHz in PS complexes at ~5 K. Thus, ignoring line broadening due to pure dephasing is usually justified in photosynthesis research at low temperature.

2.4 Inhomogeneous Broadening

Perfect Crystals

The Spectral Hole burning is a technique [28, 41] that is intimately related to disorder in this system. Such disorder may be caused by a variety of reasons. For example, it is possible for holes to be burnt into Doppler-broadened gas phase spectra with a disorder arising out of the Maxwell-Boltzmann velocity distribution. (This technique is called Lamb-dip spectroscopy.) In the spectroscopy of matrix-isolated probe molecules, disorder is caused by structural imperfections. Figure 2.3A illustrates an ordered lattice structure doped with dye probe molecules. The probe molecules are isolated from one another if their concentration is low enough. Due to the environment of each probe molecule being identical, the spectral features are identical as well.

If the host matrix is not so perfectly ordered that each molecule is in an identical environment, each molecule will experience a *different local nano-environment*. These different local environments arise from the particular inhomogeneities in the host matrix that shift the ground and excited states of the impurity molecules, and in solid matrices this is always the case [28]. Therefore, the coupling of each impurity molecule to the host matrix will be different and this will result in a distribution of the ZPL frequencies. This phenomenon is called *inhomogeneous broadening* [28,31].

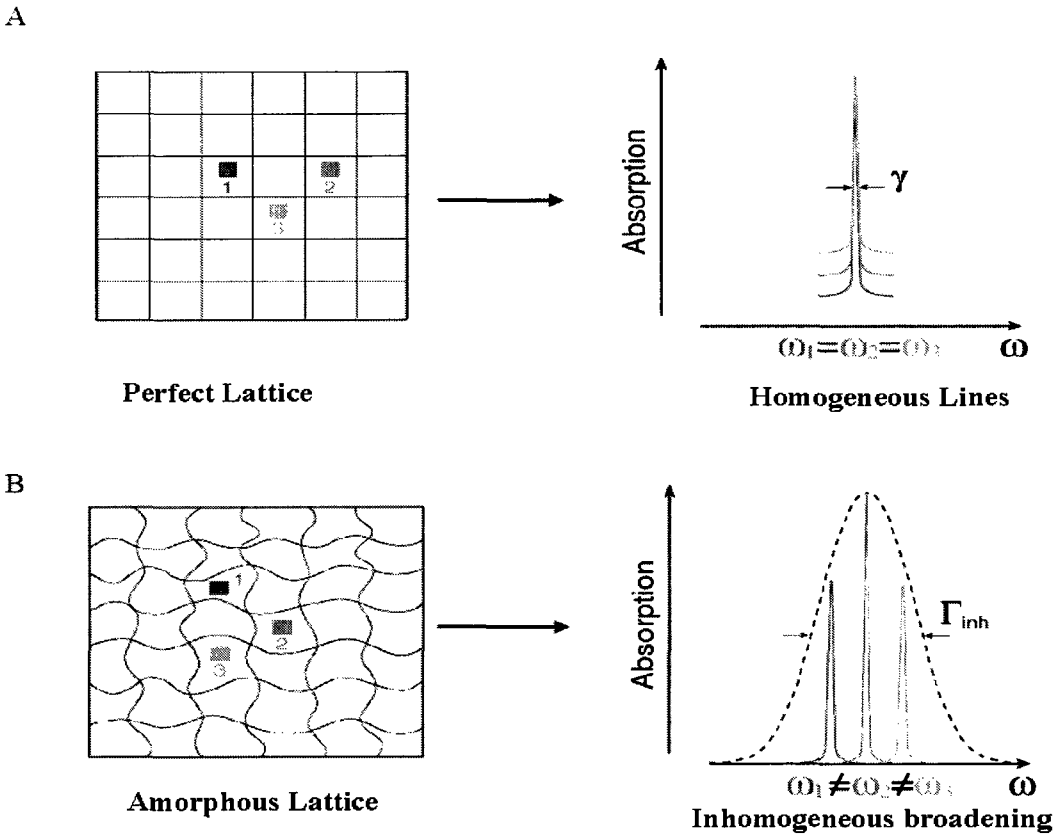

Figure 2.3. Schematic of homogeneous vs. inhomogeneous broadening. In frame (A), guest impurity molecules are in a perfect host lattice. Homogeneous lines overlap, resulting in an absorption spectrum with a linewidth equal to that of the individual ZPL. In frame (B) the impurity molecules are in a disordered host lattice, so that each impurity molecule absorbs at different frequency. This leads to a distribution of ZPL absorption frequencies and thus, the impurity absorption band is ***inhomogeneously broadened.*** (c) Tonu Reinot, ISU.

To characterize the inhomogeneous broadening, the inhomogeneous distribution function (IDF or SDF), should be introduced. This is often assumed to be a smooth Gaussian function [28, 31, 41]. The bandwidth (Γ_{inh}) of the SDF at low temperatures is larger than the homogeneous widthγ. The disorder is large enough that $\Gamma_{inh} \approx$ 1-5 cm^{-1} [28] even for Shpol'skii systems where the guest molecules are embedded in a highly ordered crystalline

host. The inhomogeneous broadening is much greater with $\Gamma_{inh} \approx 100$ - 400 cm^{-1}, for glasses and proteins. The ensemble absorption spectrum observed in experiment is a convolution of the SDF with a single molecule spectrum discussed in the previous subsection. This convolution causes just a broadening of the ZPL and PSB features in a Shpol'skii system but a complete elimination of any discernable spectral features in a glassy system (Fig. 2.3b). This convolution consequently gives a characteristic width of about $\Gamma_{inh} + S\omega_m$ for the ensemble spectrum, where ω_m is the mean phonon frequency and S is the Huang-Rhys factor [32, 33, 41,]. Because the detailed ZPL and PSB information is obscured by the inhomogeneous band, methods of selective excitation at low temperature are necessary. Many site-selective spectroscopies (techniques that make use of narrow-band lasers) have been developed to overcome the effects of large inhomogeneous broadening: fluorescence line narrowing (FLN) [41, 42], spectral hole burning (SHB) (see below) [43-45], photon echo (PE) [42,46,47], and single-molecule spectroscopy (SMS) [48,49]). SHB and SMS, in particular, provide extremely high spectral resolution and sensitivity and are powerful tools for probing the molecular dynamics and structural disorder of amorphous glassy solids. This is especially true for SMS, as it works at the ultimate limit of site selective spectroscopy- spectrally and spatially selecting out an individual impurity in an ensemble.

2.5 Hole-burning Spectroscopy

The physical principles of SHB are straightforward. A narrow bandwidth laser (with λ_B being burn wavelength) is used to excite a small subset of impurity molecules in

an inhomogeneously broadened absorption band via their ZPLs. After these molecules are optically excited, they are then photophysically or photochemically transformed so that they no longer absorb at their original frequency after they return to the ground electronic state. This leaves the inhomogeneous absorption band with a "hole" whose shape reveals the ZPL and PSB structure of these selected molecules (see Fig. 2.5). Only the homogeneous lines that absorb at the exact same frequency are "burned" for sufficiently narrow line width laser ($\gamma_{laser} << \gamma$).

The different photochemical and photophysical pathways resulting in a spectral hole determine the particular hole burning type. Hole-burning mechanisms can be divided into two categories: persistent HB and transient HB (THB). Within the first category, there is ***photochemical HB*** (PHB) and ***non-photochemical HB*** (**NPHB**). The time scales involved in persistent SHB at low temperature are usually seconds to hours, whereas THB spectrum often lasts only microseconds (μs) or milliseconds (ms). In photochemical hole-burning (PHB) spectroscopy [44,47,49] there is a photoreaction (such as tautomerization, bond breaking, or isomerization) of the impurity molecules in the excited electronic state resulting in permanent chemical identity changes. As a result, the molecules' optical properties become different and they do not absorb at the original excitation frequency any more. In nonphotochemical hole-burning (NPHB) spectroscopy [29, 35], the host matrix experiences structural rearrangement when the impurity molecules are optically excited [51]. When the photochemically stable impurity molecules return to the ground electronic state, the local nano-environment is no longer the same and this results in a shift of the impurity molecules ZPLs, causing a spectral hole. Compared to the width of the SDF, the resulting spectral shift of the photoproduct in PHB is usually large. On the other hand, the

transition frequency of the product of NPHB still stays close to the burning frequency. The spectral distribution of the photoproduct in NPHB is known as antihole. As some freedom to rearrange the host is required in this case, NPHB is observed only in amorphous systems (polymers, glasses and protein hosts).

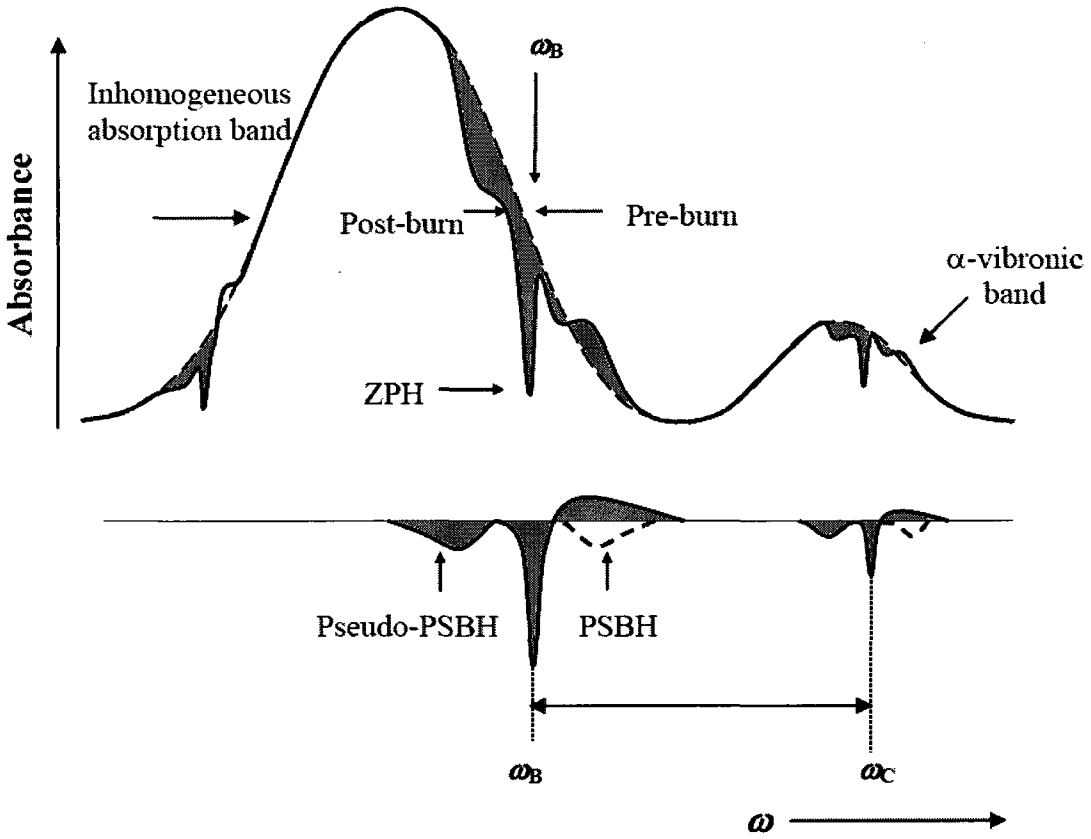

Figure 2.4. Spectral hole-burning in an inhomogeneously broadened absorption band [31]. Two curves represent the pre-burn (dashed-line) and the post-burn (solid line) absorption spectrum. After hole burning at frequency ω_B, the hole-burning spectrum is formed, as shown in the lower part of the figure (the pre-burn - post-burn absorption spectrum). Spectral holes form at ω_B and ω_C. The hole at ω_B consists of a zero-phonon hole (ZPH) component, which forms from burning out the ZPLs that are excited at ω_B. The "real"

phonon side band hole PSBH forms from burning out the PSBs that are excited at ω_B. The pseudo-PSBH results from burning out the ZPLs that lie lower in energy to ω_B, and burn via their PSBs. A hole at ω_C that is a vibronic replica of the ZPH, with $\omega_C - \omega_B$ being some localized vibrational mode of the molecule.

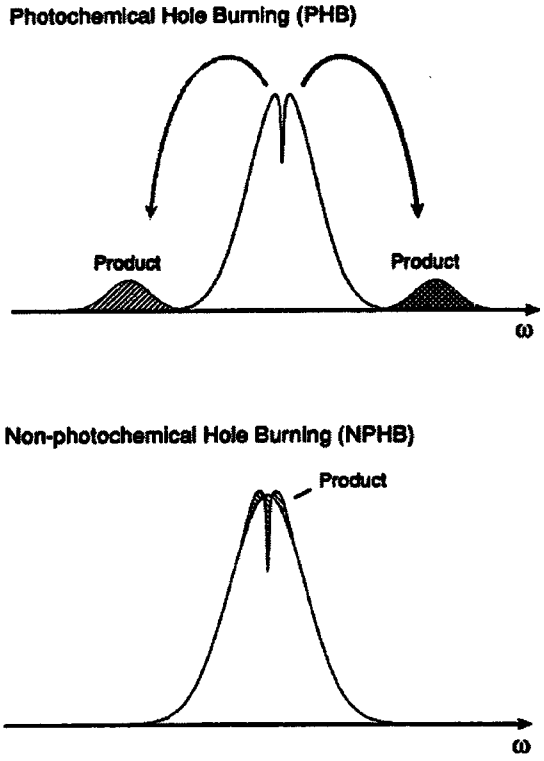

Figure 2.5: Spectral distribution of the photoproduct after photochemical (PHB) and non-photochemical (photophysical) (NPHB) hole burning. From [31].

2.6. Two-level systems (TLS)

Unlike crystals whose low temperature properties are determined by phonons, those of glasses and proteins are determined by additional kind of low-temperature excitation: TLS [35,52, 53] are groups of atoms (or just atoms in some cases) that may occupy two slightly different energetic configurations. The phenomenon of nonphotochemical hole-burning (NPHB) is accounted for by the coupling of the impurity molecules to these *TLS* (See Figure. 2.6) [51,54, 55]. The superscripts α and β label the ground and excited electronic states of the impurity molecule. Excitation of the electronic transition of a chromophore at frequency ω_B occurs in the left well, and is followed by a tunneling process in the excited electronic state. If the double-well potentials in the excited and ground states of the TLS / chromophore system have different asymmetry, the electronic transition energy will be different for molecule trapped in the right well. If the barrier height is significantly larger in the ground state than in the excited state, the system is trapped in the right well semi-permanently (at low temperature).

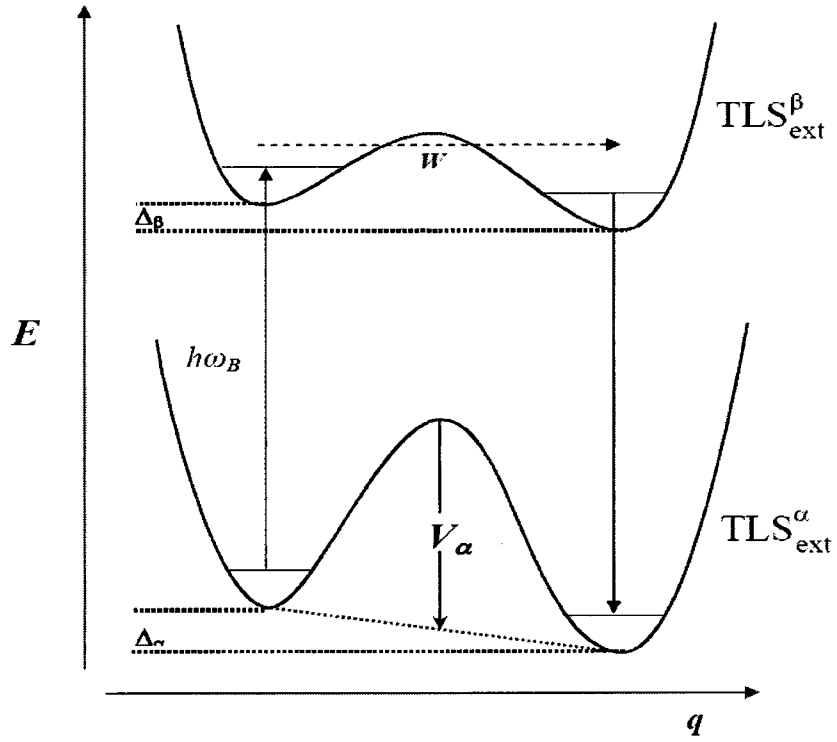

Figure 2.6. Schematic of the NPHB mechanism [22, 27, 31]. The diagram shows the extrinsic two level system (TLS_{ext}) of a guest molecule in the ground state (α) and excited state (β). After excitation ($h\omega_B$) at the burn frequency (ω_B) to β, the TLS_{ext} flips, due to the much lower barrier height (V_α) compared to the ground state, through phonon assisted tunneling (PAT), which is represented by the tunneling frequency, W. The molecule then decays to the ground state and finds itself in a different host configuration, and therefore absorbs at a different frequency. This results in the formation of a persistent spectral hole that can be observed experimentally. $\Delta\alpha$ and $\Delta\beta$ are the double well asymmetry parameters in the ground and excited state, respectively. q represents the intermolecular coordinate, ω_B is the burn frequency.

Two types of TLS - extrinsic (TLS_{ext}) and intrinsic (TLS_{int}) – are distinguished in case of NPHB in glasses [54,56]. TLS_{ext} are associated with the impurity molecule and its

inner shell of solvent molecules. The TLS_{int} exist in the amorphous host regardless of doping. TLS_{int} of the host are connected with the excess free volume of glasses [57] and are responsible for the initiation of the hole formation in NPHB. The coupling of the low frequency phonon modes and impurity molecules to the TLS_{int} seem to be responsible for optical dephasing in glassy solids (i.e. for the particular shape of the temperature dependence of T_2*). When the impurity molecule is optically excited, the rearrangement of the host environment is triggered and this initiates the phonon-assisted tunneling process that leads to hole formation. The rate-determining step in nonphotochemical hole-burning NPHB is the phonon-assisted tunneling in $\boldsymbol{TLS^{\beta}_{ext}}$. Figure 2.6 pictures phonon-assisted tunneling in the excited state involving phonon emission; the anti-hole site absorbs at higher energy of $\boldsymbol{\omega_B}$. There are seven other energy level schemes possible [54] making eight all together. Four of these lead to blue shifted anti-hole sites while the other four lead to red-shifted sites. Four of the schemes involve phonon absorption and the others involve phonon emission. Beyond the TLS model, further extensions have also been made [58]; Shu and Small have proposed multi-level systems (MLS) in glasses and proteins, with several energetic configurations are present to offer deeper explanation of the NPHB phenomenon [54,55]. In case of proteins (including photosynthetic complexes) the picture of MLS further develops into multi-well multi-tier energy landscape [59, 60]. One can also note that in case of photosynthetic complexes, where chromophores are built into protein not by scientists but by Nature, the distinction between intrinsic and extrinsic TLS loses meaning.

Both NPHB and PHB are known as persistent hole burning methods, as the holes can be observed long after they are burnt. This differs from *transient spectral hole-burning,*

where holes can only be observed on a timescale of μs or ms [33]. The triplet state is used as a reservoir to store impurity molecules in resonance with the laser in transient spectral hole burning (or *triplet bottleneck hole-burning* (TBHB)). The decay of the transient hole may be measured using time-domain methods. In frequency-domain, transient hole burning experiment involves measuring the difference between spectra acquired with laser on and laser off.

Summarizing, PHB, NPHB, and TBHB are particularly powerful methods in determining the low temperature excitation/ energy transfer properties of photosynthetic pigment protein complexes where spectra are inhomogeneously broadened due to intrinsic structural disorder of the protein matrix [31,35, 36]. Such spectroscopies uncover important information, for example: (1) the inhomogeneous broadening of Γ_{inh} of field $S_0 \rightarrow S_1(Q_y)$ chlorophyll pigment protein electronic transitions via ZPH action spectra [34, 36,61], (2) electron-phonon coupling parameters (S and ω_i) and intramolecular Franck-Condon factors via vibronic spectral hole structure [31,62,63], (3) the extent of correlation between site-distribution functions (SDF) of different molecular electronic transitions [64], and (4) the excitation energy transfer (EET) and electron transfer rates from the zero-point vibrational level in and between different photosynthetic complexes [54,64]. Information obtained from (1), (2), and (3) are especially important for photosynthetic EET calculations since they determine the spectral density in the nonadiabatic Förster rate equation (see Chapter 4). More recent developments in NPHB spectroscopy involve combining SHB with external fields, e.g. electric (Stark), or high pressure [65,66].

There are several formalisms developed for the theoretical modeling of SHB [35,58,67]; one of the formalisms, developed by Hayes and Small [32], has been

successfully used to simulate low temperature spectral holes of impurity doped glasses such as APT in glassy water and photosynthetic complexes such as the bacterial RC, photosystem I and II of cyanobacteria, and the FMO antenna complex [68]. The master equation describing the absorption spectrum after burning with a laser at ω_B for time t in low temperature limit is given by:

$$A(\Omega,t) = \exp(-\sum_k S_k)\prod_k \sum_{R=0}^{\infty}\left(\frac{S_k^R}{R!}\right)\int d\omega G(\omega)\, exp^{-\sigma P\phi t L(\omega_B-\omega)} l_{R,k}(\Omega-\omega-R\omega_k) \tag{2.6}$$

where $G(\omega)$ is the SDF introduced previously, σ is the integrated absorption cross section of the impurity molecule (cm^2), P is the photon flux (number of photons per unit time per unit area; $cm^{-2}\ s^{-1}$), and S_k is the Huang-Rhys factor of the k_{th} phonon. φ is the hole-burning quantum yield that is given by [69]

$$\phi(\lambda) = \frac{\Omega_0 \exp(-2\lambda)}{\Omega_0 \exp(-2\lambda)+\tau_{fl}^{-1}} = \frac{R}{R+\tau_{fl}^{-1}} \tag{2.7}$$

where τ_{fl} is the fluorescence lifetime and λ is the tunneling parameter, which can be expressed as $\lambda = d\sqrt{2mV}/\hbar$ through the TLS parameters (see Figure 2.6). Here V is the barrier height in the excited state, m is the reduced mass of the tunneling entity and d is the change in generalized coordinate associated with tunneling. The $l_{R,k}$ are the single site lineshape functions with R=0,1,2... corresponding to the 0,1,2,...-phonon transitions. $l_{R=0}$ is the ZPL lineshape function which is Lorentzian with the width γ.

L $(\omega-\omega_B)$ is the single site absorption spectrum for the ZPL centered at the burning laser frequency, ω_B. Then $L(\omega-\omega_B)$ can be written as follows

$$L(\omega_B - \omega) = \exp(-\sum_k S_k) \prod_k \sum_{R=0}^{\infty} \left(\frac{S_k^R}{R!}\right) l_{R,k}(\omega_B - \omega - R\omega_k) \qquad (2.8)$$

The hole burned spectrum is then the difference between the post-burn and pre-burn spectra, or $A_t(\Omega) - A_0(\Omega)$. In the shallow hole limit and assuming the ZPL is Lorentzian, th width of the hole is just twice the homogeneous line width γ.

Chapter 3

MODELING SPECTRAL HOLE BURNING IN PHOTOSYNTHETIC COMPLEXES

Photosynthetic complexes are membrane-bound proteins holding together a network of pigment (mostly chlorophyll; Chl see Chapter 1) molecules located relative to each other in order to facilitate light harvesting, energy funneling to the reaction center and electron transfer across the membrane. The trans-membrane potential difference produced by the photosynthetic complexes is further used by bacteria and plants in the synthesis of various organic compounds.

The techniques of optical spectroscopy are focused on interactions of photosynthetic complexes with light and thus offer the most precise way to obtain relevant information about their photophysical properties. The optical spectra of photosynthetic complexes consist of partially overlapping bands. Each band corresponds to certain *Chl molecules* in the complex and is a convolution of a single-molecule spectrum and the Inhomogeneous broadening (due to the amorphous character of protein environment, see Chapter 2) which is usually described by "*site distribution function*" (SDF), defined as a relative number of molecules having the purely electronic (O-O) S_0-S_1 transition at a given frequency. Thus, the information contained in the homogeneously broadened lines is hidden.

Several methods were developed to overcome inhomogeneous broadening. Spectral hole burning (SHB) and Single Molecule Spectroscopy (SMS) have shown the ability to resolve the intricacy of significant details on primary processes in photosynthesis. The optical spectrum of a single molecule in a solid (protein environment of the Chl molecules in

photosynthetic complexes behaves as an amorphous solid) (see Chapter 2) is made up of a narrow zero-phonon line (ZPL) and phonon sidebands, which correspond to the electronic transitions accompanied by the excitation of either delocalized lattice (protein) vibrations (phonons) or localized vibrations of the pigment molecule itself. The hole spectrum consists of a zero-phonon hole and phonon sideholes. The ZPL (ZPH) width is inversely proportional to the excited state lifetime. Analysis and simulations of the hole shapes and their evolution with increasing irradiation dose allows to extract the information on lifetimes and on electron-phonon couplings. Both types of information are important for building a complete and comprehensive picture of the energy transfer processes in photosynthetic complexes.

3.1 Simulations with Gaussian linewidth distributions

The development of the shape of a non-photochemical hole burnt into the absorption spectrum of a chromophore in the amorphous host can, in fact, be satisfactorily simulated (in the absence of the homogeneous line width distributions, to which we get later) for a broad range of irradiation (burning) doses. This is true only if all three of the following effects are taken into account: ω-distribution reflects that spectral hole burning is possible in the cases of both resonant and non-resonant (via phonon sideband or via tails of the Lorentzian ZPL) excitation. α-distribution is the result of various chromophore molecules being oriented with their transition dipole moment vectors at various angles with respect to laser light polarization. Of special importance is λ-distribution, the distribution of the tunneling parameter of the two-level systems (TLS) of the amorphous matrix. Non-

photochemical spectral hole burning [35,54,55,70] results from tunneling in TLS (see Chapter 2). This can be observed both in glasses [70-72] and proteins [29-37,72-76]. The basics of this model are described by Eqs.2.6-2.8 (See Reinot et al [70]):

$$\phi(\lambda,\tau_{esl}) = \frac{\Omega_0 \exp(-2\lambda)}{\Omega_0 \exp(-2\lambda) + \tau_{esl}^{-1}} \tag{3.1}$$

Equation 3.1 serves as a reminder and presents the SHB yield, which enters SHB master equation. The simulated hole growth kinetics (HGK) and hole spectra shown in all figures below were obtained using:

$$D(\Omega,t) = 1.5\int d\omega L(\Omega-\omega)G(\omega)\int d\lambda f(\lambda)\times \\ \times\int d\alpha \sin\alpha\cos^2\alpha e^{-P\sigma\phi(\lambda,\tau_{esl})L(\omega_B-\omega)t\cos^2\alpha} \tag{3.2}$$

The latter expression, which is modified Eq. 2.6, (see Ref. 5 for physical basis of Eq. 3.2) demonstrates the absorption at Ω following burning at ω_B with photon flux P for time t. $G(\omega)$ is the Site Distribution Function (SDF), demonstrating the likelihood of coming across different zero-phonon transition frequencies before burning, σ and ϕ are the integral absorption cross-section and hole burning quantum yield, respectively. $L(\omega_B-\omega)$ is the single site absorption profile , see Chapter 2. $f(\lambda)$ represents the Gaussian distribution of tunneling parameter λ, which affect the hole burning yield ϕ in Eq.1. It is peaked at λ_0 and has standard deviation of σ_λ.. The existence of the λ-distribution is a consequence of the distributions of the barrier heights and widths. Ω_0 is the constant pre-

factor in the Fermi Golden rule expression for the TLS relaxation rate for nonphotochemical hole burning. $\Omega_0 = 7.6\ 10^{12}\ s^{-1}$ for APT in glassy water [70]. When this number is modified, it effectively shifts the λ_0, the peak of the λ-distribution. We keep it the same as utilized in [70] in our modeling in order to compare our λ-distribution parameters with that obtained for glasses before.

Some examples of the holes calculated using Eq. 3.2 are presented in Figure 3.1A below. The Spectral Hole Burning Simulator program(Figure 3.1 B) has been written in Visual Basic Figure 3.1 B and it has been extensively tested in our laboratory for various combinations of parameters to ensure its error-free operation, as well as to determine which precision is appropriate for various cases – to find a proper trade-off between the calculation precision and calculation time. In its present form the program allows for simultaneous burning into two overlapping bands with different electron-phonon coupling parameters, and different distributions of the tunneling parameter and of homogeneous line width.

Concerning pigments well isolated from each other in a glassy matrix, excited state lifetime is set at $T=0$ by radiative decay time τ_{fl}. At $T>0$ the effective lifetime is also affected by pure dephasing. The effects of line width distributions on hole burning are practically unexplored. While Reinot et al. made a brief study of the effects of the (weibull) distribution of excited state lifetimes due to irregularities of pure depahasing and ruled these effects negligible [71], the distribution parameters may significantly differ in the case of EET in photosynthetic complexes. The distribution of EET rates comes not from

differences from molecule to molecule in fast spectral diffusion as was the case in [71] but out of energetic disorder in photosynthetic complexes.

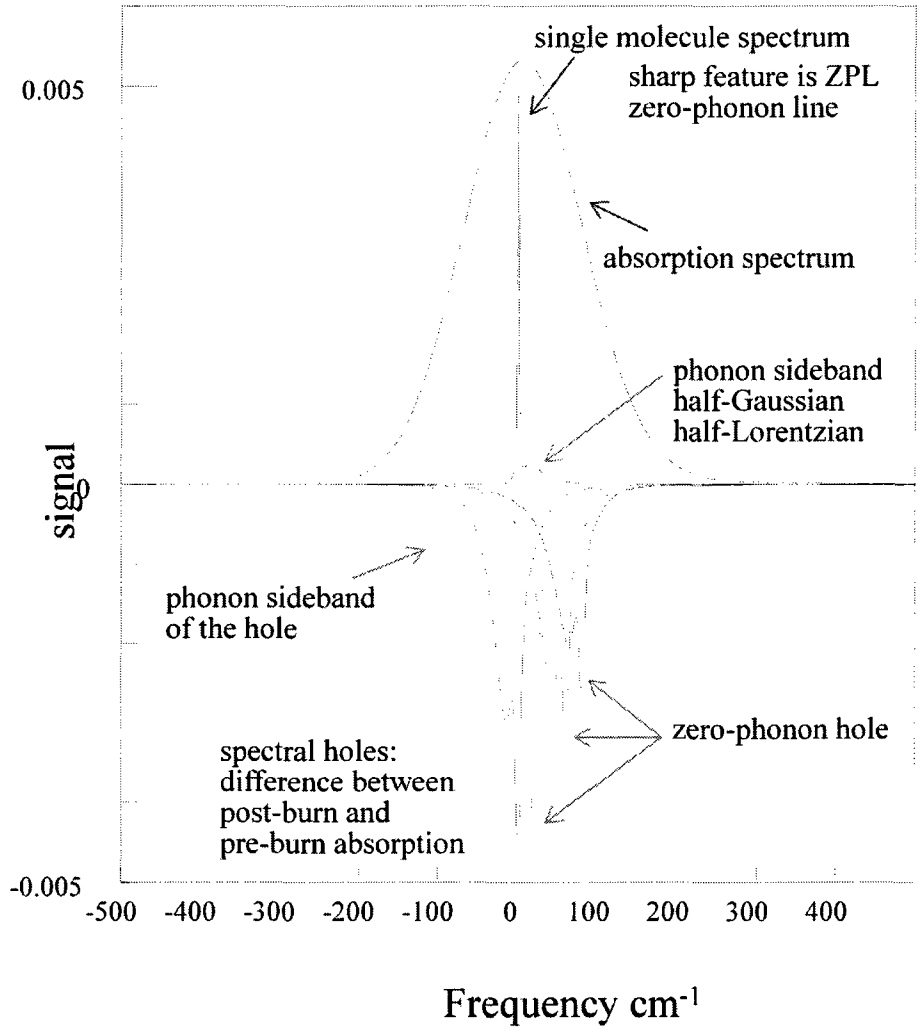

Figure 3.1a: Simulated ensemble absorption spectrum (blue), single molecule absorption spectrum (brown) and several spectral holes burnt with the same irradiation dose at different wavelengths within the inhomogeneously broadened band.

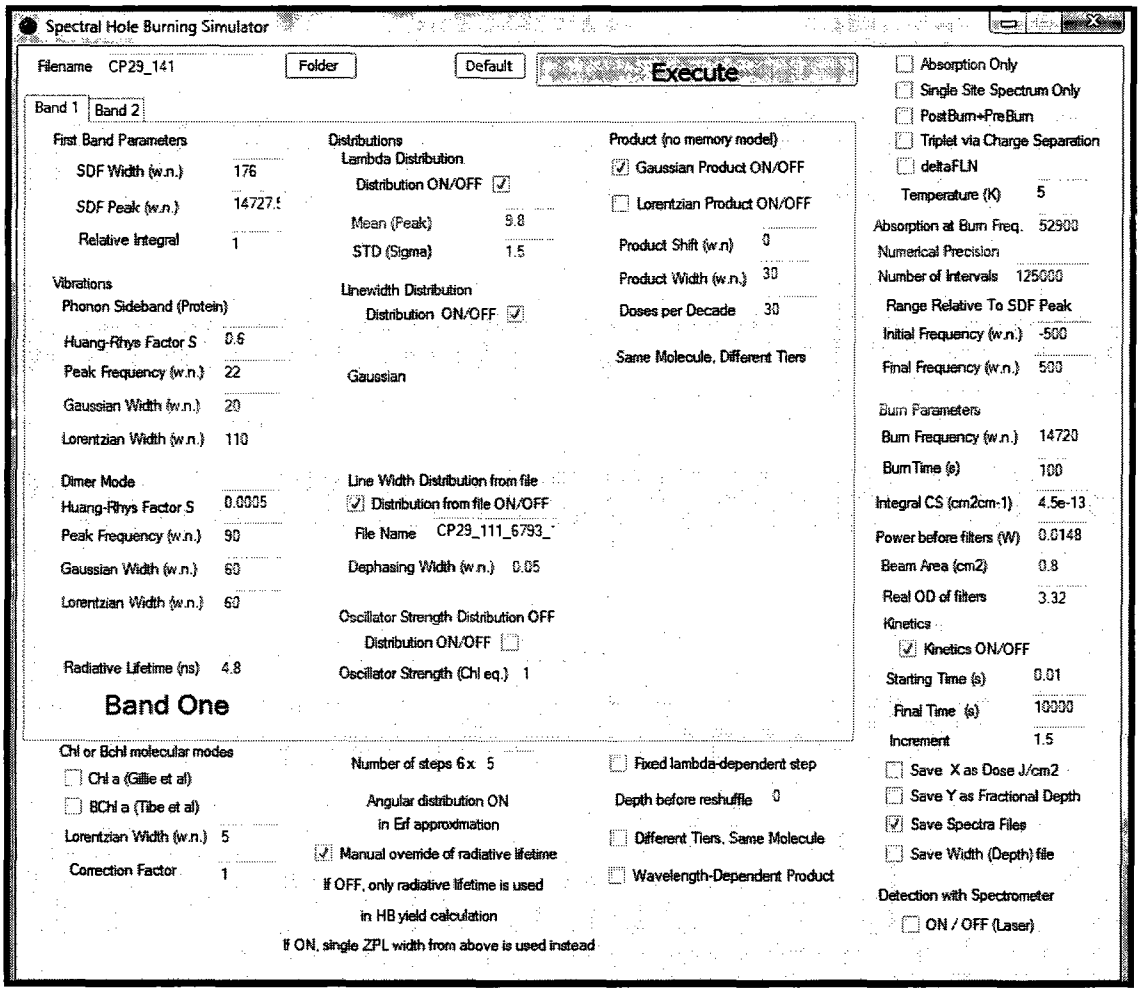

Figure 3.1b: Interface of Spectral Hole Burning Simolator.

For photosynthetic complexes, the combined influence of all four distributions has never before been explored. In almost all instances, only the simplest model of Hayes et al [33], including only ω-distribution (α and λ were fixed), has been applied to photosynthetic

complexes [74, 76]. This means that although parameters related to electron-phonon coupling were determined with sufficient precision, the calculated hole growth kinetics was far from experimental. The first attempt was recently made [77] to blend the homogeneous line width distribution into the model of Hayes et al. The excited state lifetime (in this case primary charge separation time) of the P680 state of the reaction center of plant Photosystem II (PS II) is subject to a broad distribution [78] (as demonstrated by Prokhorenko and Holzwarth [78]). By employing line width distribution corresponding to the primary charge separation rates, hole burning (triplet bottleneck and persistent) and photon echo results were reconciled and the development of the spectral hole was modeled more successfully than without this distribution [77]. It was demonstrated that the electron-phonon coupling for the P680/P684 state of the PS II RC might be much weaker than believed earlier. Therefore, the impact of the line width distributions on the hole spectra of photosynthetic complexes may likely be important. However, analysis of [77] did not include λ- and α-distributions.

As the energy transfer times in the photosynthetic complexes typically fall into the picosecond time range, the respective homogeneous line widths are at least several times (and usually orders of magnitude) larger than those observed by Reinot et al. for APT in glassy matrices [70]. Therefore, the number of frequency intervals into which the spectrum being calculated is divided can be decreased accordingly compensating, in part, for the increase in complexity of calculations associated with the inclusion of homogeneous line width distribution. While taking the lifetime (energy transfer time) distributions into consideration one must remember that in the case of non-photochemical hole burning the EET time τ_{EET} enters the Eq. 3.1 above twice – once via the ZPL width in the

homogeneous single-site spectrum $L(\omega_B - \omega)$, and also via the spectral hole burning yield, which has to be altered:

$$\phi(\lambda, \tau_{EET}) = \frac{\Omega_0 \exp(-2\lambda)}{\Omega_0 \exp(-2\lambda) + \tau_{fl}^{-1} + \tau_{EET}^{-1}} \tag{3.3}$$

In the case of the triplet bottleneck holes [77] Equation 3.3 does not apply. It is evident from Eq. 3.3 that EET and non-photochemical hole burning are **competing** processes. EET removes the excitation from given pigment and thus reduces the chances of NPHB.

On the other hand, in the reaction centers, such as PS II RC, the triplet formation occurs after the primary charge separation, and triplet hole burning yield is, in the first approximation, a constant which can be set to one without making a significant error, if in SHB experiments triplet bottleneck holes are measured after the saturation of persistent ones, i.e. after the short-lifetime end of the lifetime distribution is burned away. Thus,

$$\phi(\tau_{CS}) = \frac{\tau_{CS}^{-1}}{\tau_{fl}^{-1} + \tau_{CS}^{-1}} \approx 1 \quad for\ \tau_{fl}^{-1} << \tau_{CS}^{-1} \tag{3.4}$$

Note that, in case of charge separation, the yield of the triplet bottleneck hole burning does not depend on the tunneling parameter λ, the latter is applicable only to persistent SHB. One might argue that triplet bottleneck hole burning as in [77] probes molecules / states with broadest line widths and/or largest values of λ. (But this matters only if one attempts to explore persistent SHB due to charge separation.) The angular distribution still applies. Persistent hole burning is assumed not to remove the excitation from a given molecule and not to affect charge separation yield.

Combining Eqs 3.1-3.3 one gets:

$$D(\Omega,t)=1.5\int d\omega L(\Omega-\omega,\tau_{EET})G(\omega)\int d\lambda f(\lambda)\int d\Gamma T(\Gamma)\times$$
$$\times\int d\alpha\sin\alpha\cos^2\alpha\, e^{-P\sigma\phi(\lambda,\Gamma)L(\omega_B-\omega,\tau_{EET})t\cos^2\alpha} \qquad (3.5)$$

where $T(\Gamma)$ is the distribution of homogenous line widths and all other quantities are the same as above. (For simplicity's sake, our software operated with the distributions of the homogeneous line widths $\Gamma=(c\pi\tau_{EET})^{-1}$+constant dephasing-limited width (which is, for example, of 0.03 cm^{-1} for CP43 at 5 K), rather than the distributions of the lifetimes.) The angular integral was treated as demonstrated in [67]. It was taken into account that

$$F(x)=1.5\int d\alpha\sin\alpha\cos^2\alpha\cdot e^{-x\cos^2\alpha}=\frac{1.5}{x}\left[\frac{\sqrt{\pi}}{2}\frac{erf(\sqrt{x})}{\sqrt{x}}-e^{-x}\right], \qquad (3.6)$$

which was fitted with a polynomial for x<10 and with $(1/x)\sqrt{9\pi/16x}$ for x>10. Integrals over λ and homogeneous line width were calculated as sums with at least 30 members each, fast Fourier transform algorithm was used for integration over ω. Assuming that there exists no correlation between the SHB rate $\Omega_o exp(-2\lambda)$ (governed by the TLS dynamics) and energy transfer time (governed by inter-pigment interactions and spectral overlaps), a probability of a certain combination of Γ and λ was assumed to be proportional to $f(\lambda)\cdot T(\Gamma)$. In the complex excitonically coupled systems with multiple EET pathways relying on particular realizations of disorder, such assumption may not always be appropriate. For example, particular states may be dominated, even at the same fixed

wavelength, by a variety of chlorophylls, which may demonstrate distinct distributions of HB yield and which transfer energy along distinct paths characterized by distinct distributions of EET rates.

The multi-chromophoric nature of the photosynthetic complexes may affect more parameters than just the ZPL shape and SHB yield. Owing to the excitonic interactions, states being burnt could have oscillator strength different from that of the single chlorophyll (or bacteriochlorophyll) molecule, and the oscillator strength of the states absorbing at given wavelength may also be subject to distribution. To account for that effect during simulations, one might add another distribution to the Eq. 3.5: that of the integrated absorption cross-section σ. However, it can be demonstrated that introducing realistic oscillator strength distributions has very little effect on the hole growth kinetics. Same is true for realistic distribution of electron-phonon coupling parameters [79-81]. As in [82], both latter distributions were ignored to speed up the calculations.

We start with describing the behavior of the spectral holes in the absence of the line width (lifetime) distribution.

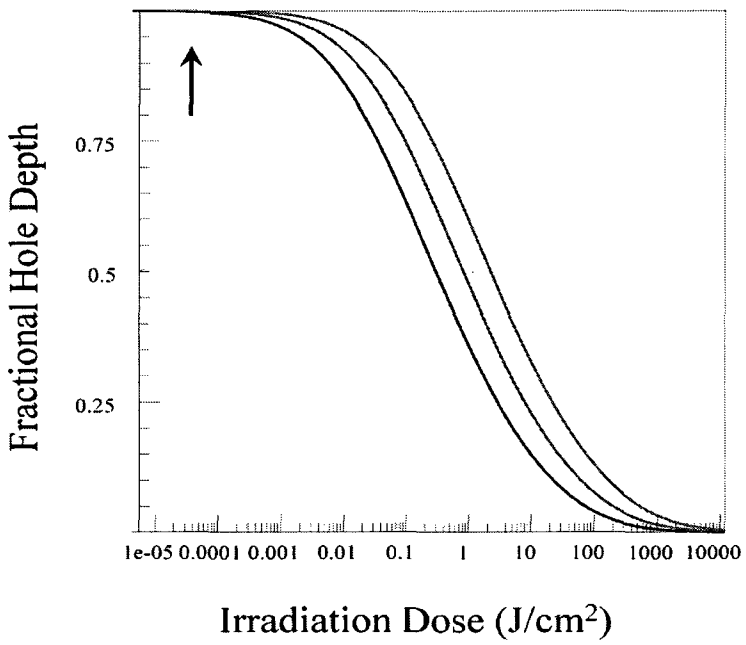

Figure 3.2: Simulated hole growth kinetic (HGK) curves (T=5 K), with burn wavelength coinciding with the SDF peak, The Gaussian distribution of tunneling parameter λ_0 was peaked at various λ_0 =11, 10.5 and 10, for red, blue and black curves, respectively. σ_λ=1. The homogeneous line width is 0.04 cm^{-1}.

The modeling of ZPH growth kinetics was done using master equation (Eq.3.2), the parameters reported in Table 1 below were used unless specified otherwise in the figure captions. Figure 3.2 shows the effect of different values of the peak of the distribution of tunneling parameter λ on the hole growth kinetics (HGK) HGK curves illustrate the evolution of the depth of the ZPH while burning is progressing The λ-distribution was peaked at λ_0=10, 10.5 and 11 and the standard deviation was fixed at σ_λ=1. These values are typical for photosynthetic complexes. The homogeneous line width used in the simulations was 0.04 cm^{-1} (1.2 GHz), also a typical value for photosynthetic complexes at 5K [72]. The HGK data (Figure 3.2) certainly show a big qualitative effect of varying λ_0

between 10 and 11. On a logarithmic plot, the increase of λ_0 results in a shift of the curve towards higher irradiation doses without the change in the shape of the curve.

Table 3.1 Simulation parameters of modeling for ZPH growth kinetics

Parameters(*Band A*)	Value
Zero-phonon Line width	3 cm^{-1}
Peak Energy of PSB (ω_m)	14705 cm^{-1}
Huang-Rhys factor(S)	0.6
Profile of PSB	$\Gamma_{Gaussian}$ (cm^{-1}) =22; $\Gamma_{Lorentzian}$ 140 cm^{-1}
Tunneling parameter (λ_0)	10
σ_λ	1
Phonon sideband - Peak Frequency (ω_B)	22 cm^{-1}
SDF Profile	Peak 14705 cm^{-1}; width 135 cm^{-1}
Actual burn position:	14705 cm^{-1}
Integrated cross-section:	$4.5 \cdot 10^{-13} cm^2 cm^{-1}$

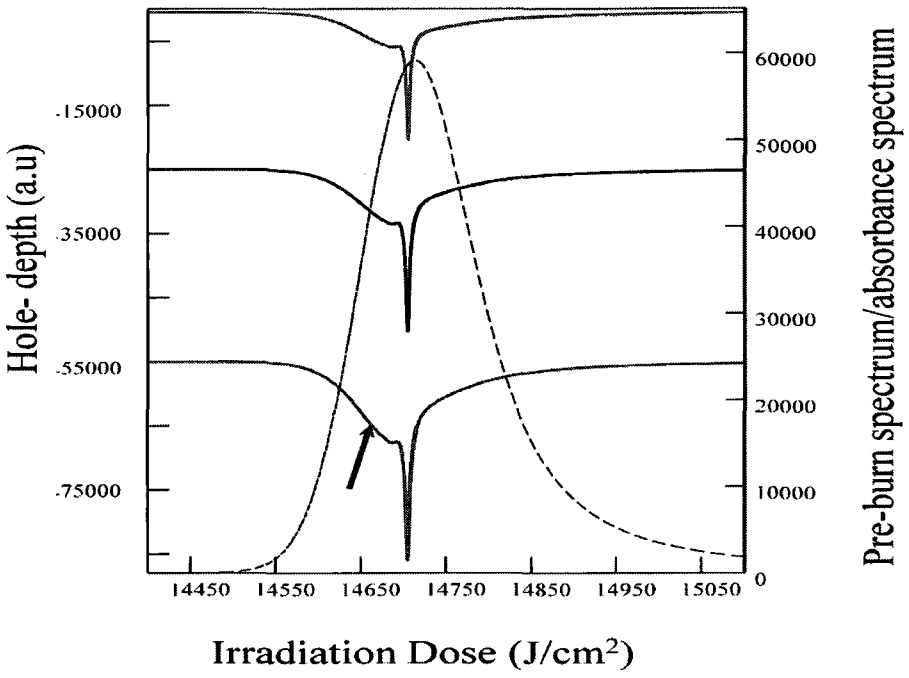

Figure 3.3: Simulation of absorption spectrum and the holes burnt at the peak of the SDF for various values of λ_0= 11, 10.5, and 10 corresponding to red, black and blue curves, respectively. σ_λ = 1; ZPL=3 cm^{-1}, i.e. there is no line-width distribution; other parameters are reported in Table 3.1.

Figure 3.3 represents not the HGK, but the whole hole spectra obtained for the same irradiation dose and different values of λ_0. In agreement with the HGK curves, the lower λ_0 corresponds to deeper holes for the same dose. The absorption spectrum is also presented in Figure 3.3 for comparison.

Next we explore the effects of changing the width of the tunneling parameter distribution, σ_λ, on the hole growth kinetics. Figure 3.4 depicts the HGK curves obtained for fixed λ_0=10 and σ_λ=0.0, 0.3, 0.6, 1.0 and 1.5.

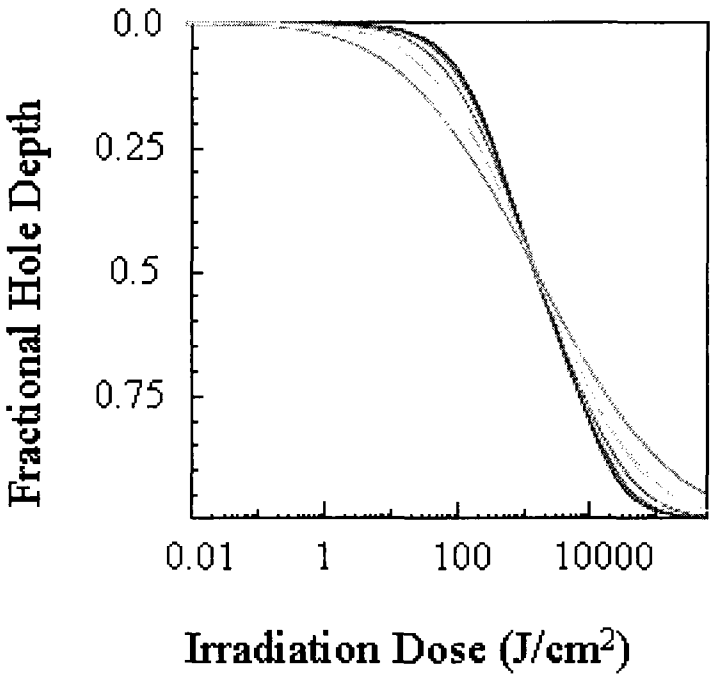

Figure 3.4: Dispersive hole growth kinetics (HGK) for λ_B at the peak of the SDF and in the absence of the line width distribution. ZPL width =3 cm^{-1}. The Gaussian distribution of tunneling parameter λ was peaked at 10 and had σ_λ= 0.0 (no dispersion), 0.3, 0.6, 1.0 and 1.5, corresponding to black, blue, red, green and purple curves, respectively.

As is evident from Figure 3.4, increase of the σ_λ reduces the "slope" of the sigmoidal HGK curve, and makes it more resembling a straight line (NB: the x-axis is logarithmic). As one could suspect, and as we will indeed see below, the line width distributions may affect the dependence of the hole width on various model parameters. Thus, before engaging in exploring these effects, we must look at the hole width behavior in the absence of line width distribution. Figure 3.5 depicts the dependence of the hole width on λ_0 for fixed σ_λ. The hole width was defined at half the maximal depth of the hole (at λ_B)

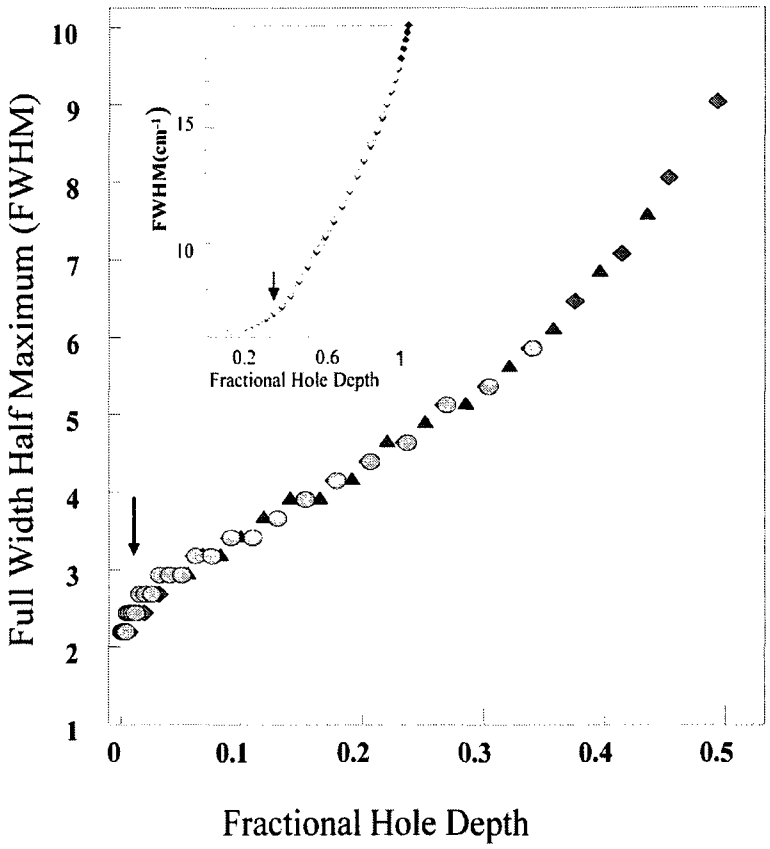

Figure 3.5: Hole FWHM dependence on Fractional hole depth. The diamonds, Triangles, and circles correspond to various values of λ_0 - 10, 10.5, and 11 respectively. σ_λ=1; ZPL width=1 cm^{-1} see Table 3.1 for other parameters that were used.

The λ-distribution was peaked at λ_0 = 10, 10.5 and 11. The modeling of the dependence of the hole width on fractional depth demonstrated that the width dependence on depth has almost identical behavior for any λ_0. It is obvious that for small irradiation doses the hole width extrapolates to twice the homogeneous line width, as predicted in Chapter 2.

Figure 3.6 depicts the dependence of the hole width on the fractional hole depth for fixed value of λ_0 and varying values of σ_λ. We stress that the FWHM of the hole is determined at half the maximal depth of the whole hole feature, not at half the depth of the narrow ZPH component alone (see insert of Figure 3.6).

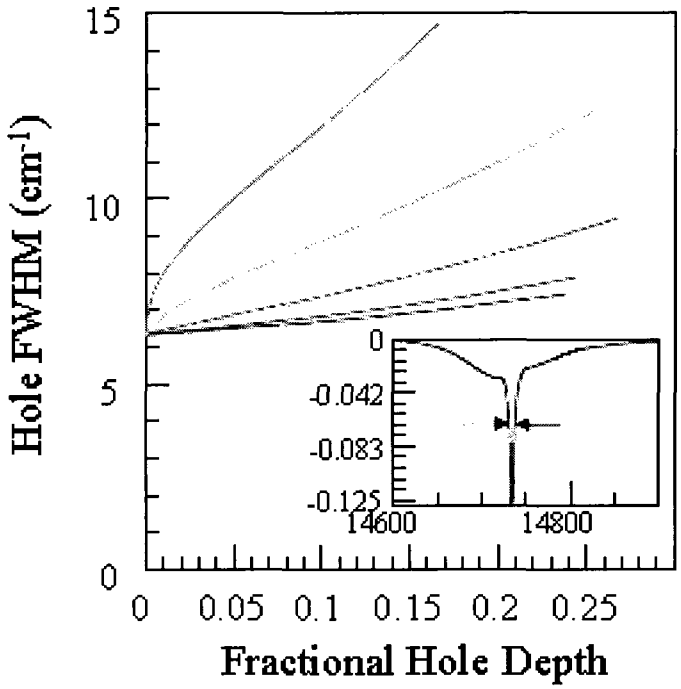

Figure 3.6: Hole FWHM as a function of the fractional hole depth, from bottom to top curves were obtained with tunneling parameter mean λ_0 =10 and σ_λ= 0.0, 0.3, 0.6, 1.0 and 1.5, respectively. The simulation was done with burning at the peak of the SDF and T=5 K. ZPL width was 3.0 cm^{-1}. The insert contains an example of the individual hole spectrum. Arrows indicate that hole width was measured at half the maximal depth. Green curve in this figure is the same as the black one in the figure to the left.

It is evident from the figure that for larger σ_λ values (more dispersive hole growth kinetics) the hole is broadening faster.

In this chapter we discuss the effects of a Gaussian distribution of the homogeneous line widths. There is no physical reason to expect the line width distributions to be perfectly Gaussian in reality. However, Gaussian distributions will serve their purpose as with their help we demonstrate general tendencies which one can expect in the case of broad more or less symmetric line width distributions indeed observed, for example, for PS II RC [77,78] or for B800-B850 EET in LH 2 complex [82-85]. One class of more realistic distributions resulting from Förster-type EET will be discussed in the Chapter 4.

Figure 3.7 contains the HGK curves obtained for different widths of the line width distribution, with all other parameters being fixed.

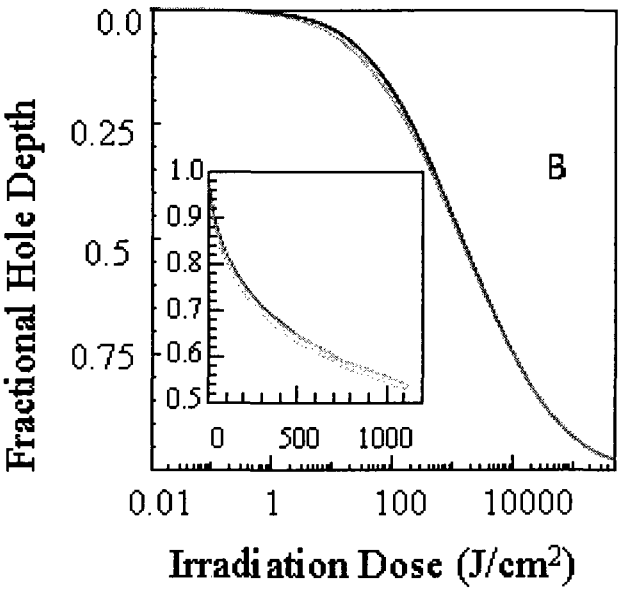

Figure 3.7 A semi-logarithmic plot of the fractional hole depth as a function of irradiation dose at 5 K. The calculation was performed with Gaussian linewidth distribution peaked at 3 cm^{-1} and with widths 0.0 (no distribution) 0.5, 1.0, 2.0 an 3.0 cm^{-1} corresponding to black, blue, red, green and purple curves respectively. The insert depicts the beginning of the curves on a regular (not logarithmic) scale. λ_0=10 and σ_λ=1.0

Figure 3.7 shows modeling of HGK as a function of irradiation dose for different widths (0.0, 0.5, 1.0, 2.0, and 3.0 cm^{-1}) of the line width distribution, corresponding to black, blue, red and green curves respectively. The resonant holes grow somewhat faster in the beginning with the increased width of the distribution. However, for larger irradiation doses and hole depths, the curves become practically indistinguishable. Thus, the shape of the HGK curve is not very sensitive to the presence of the line width distribution. In the next Figure, 3.8, we present the dependence of the hole width on fractional hole depth for various widths of the Gaussian line width distribution and all other parameters being fixed.

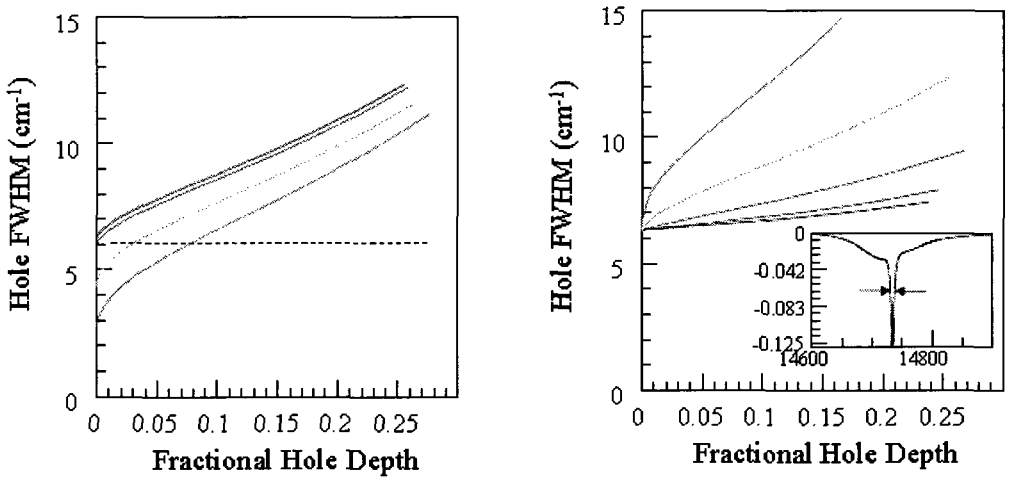

Figure 3.8: Left frame: Hole FWHM as a function of fractional hole depth. The simulation was done at 5 K and with burning at the peak of the SDF and with linewidth distribution peaked at 3.0 cm^{-1} and with widths of 0.0 (distribution off), 0.5, 1, 2.0, and 3.0 cm^{-1}, corresponding to black, blue, red, green and purple curves respectively. The λ-

distribution was peaked at $\lambda_0 = 10$ and had σ_λ=1.0. Dashed horizontal line is twice the mean of the linewidth distribution.

Right frame: (same as Figure 3.6 for comparison) Hole FWHM as a function of the fractional hole depth, in the absence of the line width distribution. From bottom to top curves were obtained with tunneling parameter mean λ_0 =10 and σ_λ= 0.0, 0.3, 0.6, 1.0 and 1.5, respectively. The simulation was done with burning at the peak of the SDF and T=5 K. ZPL width was 3.0 cm^{-1}. The insert contains an example of the individual hole spectrum. Arrows indicate that hole width was measured at half the maximal depth. Green curve in this figure is the same as the black one in the figure to the left.

As Figure 3.8 indicates, the slope of the hole width dependence on dose is much more sensitive to the value of σ_λ than to the width of the line width distribution. σ_λ alone determines the "slope" of the width dependence of fractional depth. The only parameter dependent on the linewidth distribution width is to what width the hole FWHM dependence extrapolates for small burning doses. If the linewidth distribution is broad enough, the shallow holes will be much narrower than twice the mean of the line width distribution (dashed horizontal line). Holes as narrow as 4 cm^{-1} can be explained if one has the line width distribution peaked at 3 cm^{-1} and with the width of 3 cm^{-1}. This situation is close to that indeed observed in LH2 complex [82]. Summarizing, one can argue that a) one can determine σ_λ just from the slope of the hole width dependence on the irradiation dose, and it will not be very sensitive to the presence or absence of the line width distribution. Thus, protein dynamics can be disentangled from the line width distributions. Unfortunately, b) one cannot determine the parameters of the line width distribution that easily. However, if we the mean of the line width distribution is available from elsewhere (from time-domain

experiments, which are not preferentially sensitive to the longest EET times), one can determine the width of that distribution by fitting the hole FWHM dependence on its depth.

The analysis of the whole hole shape evolution probably can be helpful in disentangling the effects of the lambda distribution and the linewidth distribution, but the procedure for that is not yet developed (research in progress) At the moment we demonstrated that one cannot use the analyses of the most established parameters alone to

Fully determine the parameters of the line width distribution.

Chapter 4

REALISTIC LINEWIDTH DISTRIBUTIONS

One of the most unique physical aspects of photosynthetic complexes (PCs) is likely to be their complex, inter-connected energy transfer processes arising out of the special arrangements and couplings of different photosynthetic pigment molecules. These may cause a wide variation of energy transfer channels, and corresponding rates [86.87]. Energy transfer in PCs has thus been modeled by means of many different approximations. For instance, energy transfer has been modeled as localized Förster donor - acceptor states [88] in the weakly coupled B800 dimer ring of purple bacterial LH2 [86]. Energy transfer has been modeled through coherent excitonic relaxation in strongly coupled antenna systems, such the Fenna-Matthews-Olsen (FMO) light harvesting antenna complex [87] and through exciton formation [89], as in the PS II reaction center (RC) [77,78]. It is therefore necessary to understand the physical picture of EET in photosynthetic systems; these can be described in terms of two limiting cases: weak and strong coupling between donor and acceptor molecules (states) [90,91]. Energy transfer can be thought of as hopping process between independent, localized states in the weak coupling limit. This is the case considered in this Chapter. In the strong coupling limit, however, the electronic states cannot be thought of as localized on individual molecules, since new intermolecular coherent eigenstates (excitonic states) are formed by way of strong electronic coupling.

EET is thought of as a perturbation induced relaxation process between these coherent excitonic states.

4.1 Förster Energy Transfer Theory

Energy transfer between weakly coupled photosynthetic pigment molecules often can be satisfactorily described by Förster theory [88]. Energy transfer is characterized as an incoherent hopping process from a donor molecule to an acceptor molecule in the weak interaction limit ($V/\Gamma_{inh} << 1$) in the Förster model. The ratio of the electronic coupling between donor and acceptor pigments, V, and the disorder (inhomogeneous broadening) Γ_{inh}, is an important factor for deciding whether energy transfer occurs through incoherent hopping, and if it can be modeled with Förster theory or with Dexter theories [88,92] or excitonic relaxation. If $V/\Gamma_{inh} << 1$, then it can be assumed that interactions are in the weak coupling limit and incoherent hopping energy transfer can be assumed; however, if $V/\Gamma_{inh} >> 1$, then strong coupling interaction is present and energy transfer can be pictured through excitonic relaxation [86]. By using Fermi-Golden rule approximation [93] the energy transfer rate for this process can be calculated. As determined by Förster, this transfer rate is given as

$$k_{DA} = \frac{2\pi}{\hbar}|\langle D^* A|V_{DA}|DA^*\rangle|^2 \int_0^\infty dv J(v) \qquad 4.1$$

Here $|\langle D^* A|V_{DA}|DA^*\rangle|^2$ represents the electronic coupling between donor molecule, (D being the wavefunction of D, the donor) and acceptor molecule (A, with wavefunction A), J (ν) represents the spectral overlap between the acceptor absorption and the donor emission, [88]. It is also assumed that the electronic transition moment does not vary upon molecular nuclear motions and that the thermalization of molecular vibrations and bath phonons occur on a much faster time scale than energy transfer. In the Förster theory, dipole-dipole coupling may be safely assumed when the electronic transitions of D and A are weakly coupled and the distance between them is significantly larger than the size of the molecules (i.e. there is no wavefunction overlap [88,94]. This often corresponds with a separation distance between the donor and the acceptor of ~ 1-10 nm.

When such requirements are met, higher order multipole terms along with electron exchange terms may be neglected and the electronic coupling matrix factor between D and A, in Eq. 4.1 is

$$\langle D^*A|V_{DA}|DA^*\rangle \equiv V_{DA} = \frac{k|\overrightarrow{\mu_D}||\overrightarrow{\mu_A}|}{R_{DA}^3} \tag{4.2}$$

where $\boldsymbol{\mu_D}$ and $\boldsymbol{\mu_A}$ are the electronic transition dipole moment vectors of D and A, respectively. V_{DA} depends only on the electronic wave functions since the Born-Oppenheimer approximation is used during the derivation of Eq. 4.1.

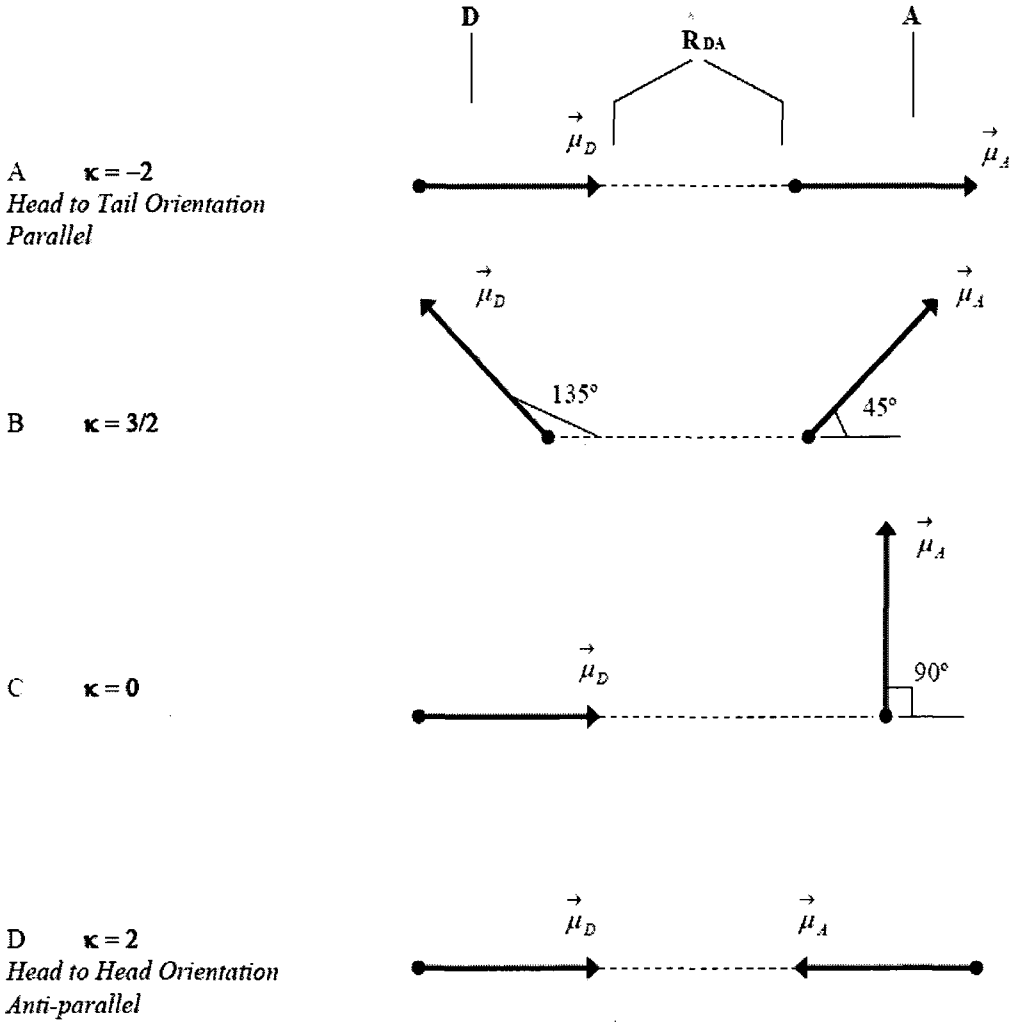

Figure 4.1: Examples of donor-acceptor dipole orientations with respective factors κ. The solid arrows represent the dipole vectors of the donor and acceptor molecules. The dashed line that connects the vectors represents the distance, between the two molecules. It is assumed here, for simplification, which both the donor and acceptor molecules are in the same plane. However, this cannot be assumed for real molecular systems.

R_{DA} represents the distance between the core of D and the core of A. κ represents the orientation factor and is defined as: $k = \widehat{\mu_D} \cdot \widehat{\mu_A} - 3\left(\widehat{\mu_D} \cdot \widehat{R_{AD}}\right)\left(\widehat{R_{AD}} \cdot \widehat{\mu_A}\right)$ where the circumflex symbol (^) represents the unit vector of the corresponding vector. Depending on the orientation, κ may range in value from –2 to 2 (see Fig.4.1). Fig. 4.1 shows κ to be the largest, when transition dipole moments of D and A are in either a head-to-head or head-to-tail orientation. For molecules with random orientations of dipole vectors, κ =2/3 [95].

The spectral overlap, ***J*(ν)** term in Eq. 4.1 also originates from the Born-Oppenheimer approximation. The Born-Oppenheimer approximation [93] allows for separation of the electronic and vibrational wavefunctions as the nuclear motions of the atoms may be on a much slower timescale compared to the motions of the electrons during the optical excitation of either D or A. The vibrational transitions of D and A are thus expressed in $\boldsymbol{J}(\nu) = \boldsymbol{\varepsilon_A}(\nu) \cdot \boldsymbol{F_D}(\nu) \cdot 1/\nu^4$, where **ε(ν)** represents the molar extinction coefficient of the acceptor in L/(mol·cm), $F_D(\nu)$ represents the normalized emission spectrum of D, and ν represents the wavenumber in cm^{-1}. $\varepsilon_A(\nu)$ and $F_D(\nu)$ are expressed as:

$$\varepsilon_A(\upsilon) = \frac{8\pi^3 N' \upsilon}{3hcnln(10)} \mu_A^2(\upsilon) \qquad (4.3)$$

$$F_D(\upsilon) = \frac{64\pi^3 n \upsilon^3 \tau}{3h} \mu_D^2(\upsilon) \qquad (4.4)$$

where N' represents Avogadro's constant divided by 1000, h represents Planck's constant, c represents the speed of light in vacuum and units of cm^2/s, n represents the refractive index of the solvent, and τ represents the excited state lifetime. $\mu_D^2(\upsilon)$ and

$\mu_A^2(\upsilon)$ (averaged over all thermal and vibrational levels, respectively) represent the vibronic transition dipole moments. *J(*(ν) is thus referred to as the Franck-Condon factor-weighted density of states [95]. The value of *J(*(ν) can range from 0 to 1; a value of 1 would indicate perfect spectral overlap.

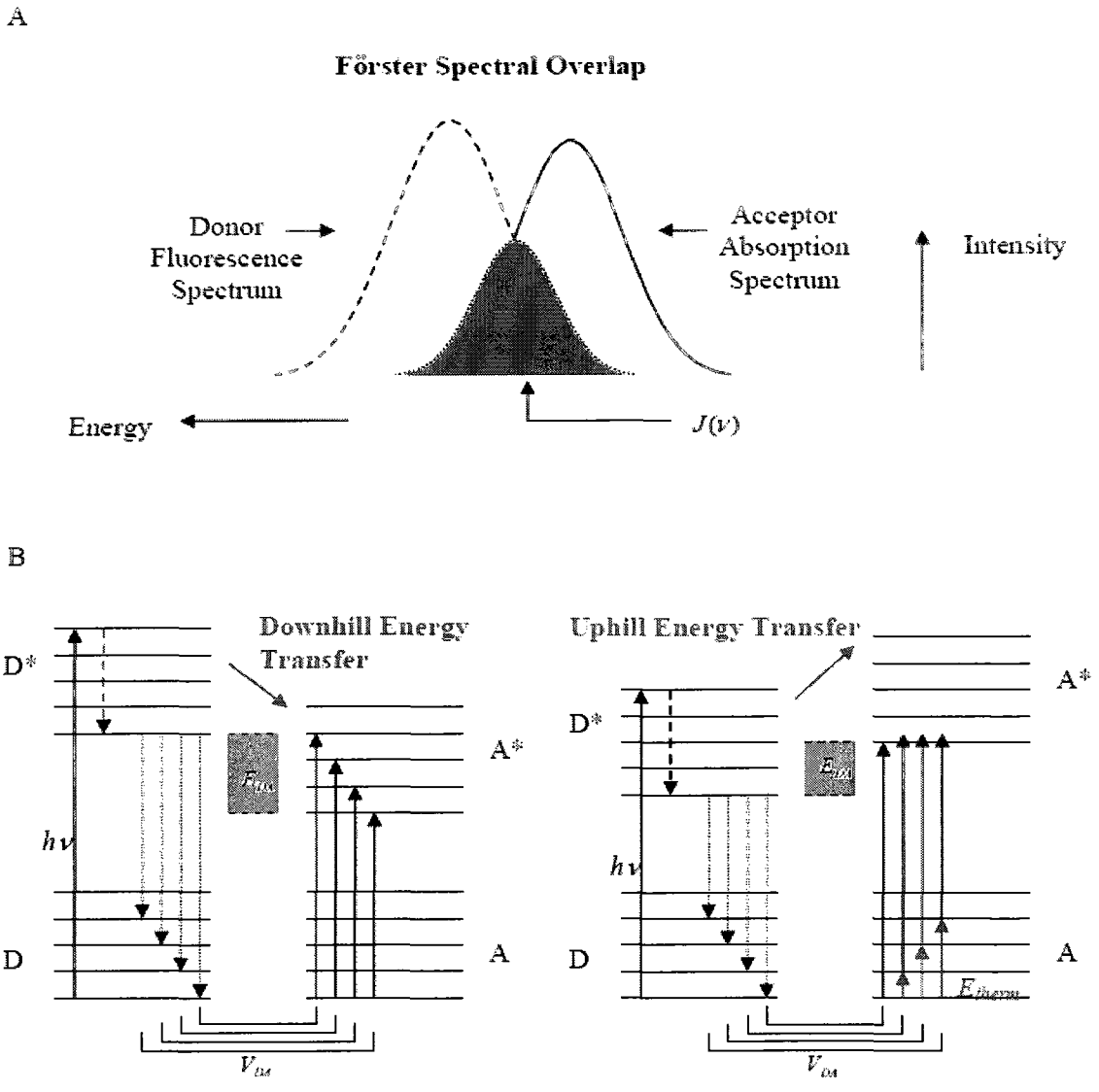

Figure 4.2: A*: A* conceptual of the spectral overlap, J(ν) [16]. B: The resonance energy transfer condition between the donor (D) and acceptor (A) molecule.

Considering the terms used (spectral overlap, donor fluorescence, and acceptor emission), one might be led to assume that energy transfer in Förster theory occurs radiatively, with D emitting a photon that is captured by A. This would be a false assumption. Energy transfer in Förster theory is a quantum mechanical non-radiative process occurring between two states which are energetically resonant [88, 94,96]. This condition of resonance is required by conservation of energy, so that the energy of the system may not change after energy transfer, due to this Förster energy transfer is often referred to as Förster resonance energy transfer (FRET) [97] (see Fig. 4.2B for an illustration of the resonance condition). The Förster rate equation (Eq. 4.1) may also be recast [88,98] this way

$$k_{DA} = \frac{1}{\tau}\left(\frac{R_0}{R}\right)^6 \tag{4.5}$$

Where R is the distance between the centers of molecules D and A, and R_0 is expressed as:

$$R_0^6 \equiv \frac{9\ln(10)}{128\pi^5 n^4 N'} k^2 \int dv * \frac{F_{D(v)}\varepsilon_{A(v)}}{v^4} \tag{4.6}$$

and defines the distance where energy transfer is 50% efficient. The energy transfer rate is inversely proportional to the distance between D and A to the sixth power and when $R_0 = R_{DA}$, the energy transfer rate equals the rate of other decay mechanisms of D (See Eq. 4.5).

Eqs. 4.1 and 4.5 are relatively straightforward but there are limits and implications with Förster theory that must be taken into consideration. Förster theory assumes that vibrational and phononic relaxation, occurs on a quicker timescale (< 1 ps) than energy transfer [88]. This cannot be assumed for sub-picosecond D-A energy transfer processes. Förster theory further considers D and A to be identical molecules and this is not always the case when studying photosynthetic pigments or other biological systems. Energy transfer is often at its peak efficiency when $E_{D\text{-}A}$ is positive and less than $h\nu_D$ ($h\nu$ is the 0-0 electron transition energy of D), allowing for increased spectral overlap [88]. This is known as "downhill" energy transfer (see Fig.4.2A). Energy transfer can still occur if E is negative however, if this is the case, there is usually not enough energy after the excited donor relaxes vibrationally to make a pure electronic transition in A. Rather, energy must come from the thermal processes and/or surroundings must be present for transfer to take place (referred to as "uphill" energy transfer) (see Fig. 4.2B).

Eqs. 4.1 and 4.5 are not always valid when the donor or acceptor line shapes are appreciably inhomogeneously broadened. When the inhomogeneous broadening of the lineshape is similar to the electronic coupling between D and A, then multiple $E_{D\text{-}A}$ may be present resulting in dispersive energy transfer (non-exponential) kinetics. Often, spectral lines are inhomogeneously broadened by ~100-300 cm and electronic couplings range from ~ 50-900 cm^{-1} for photosynthetic pigments. Thus, in studying energy transfer in photosynthetic pigments, Förster theory may need to be modified to take care of the inhomogeneous broadening [41]. Finally, since dipole-dipole coupling is valid only when the D-A distance is significantly larger than the size of the molecules, closely spaced molecules may not be modeled in this approximation. When the D-A distances are small

enough for wavefunction overlap, electron exchange interactions need to be taken into account for the electronic coupling (Dexter mechanism [92]). For intermediate couplings dipole-dipole approximation still may be broken and various other terms (monopole, quadrupole) have to be taken into account.

Various models have been developed to account for energy transfer between photosynthetic pigment molecules [43-44]. Kolaczkowski et al [99] developed the theory of dispersive kinetics of EET employing Förster model at low temperature. Some distributions of EET times in PS complexes were obtained as a by-product of some of the excitonic calculations [100-102]. However, the latter distributions may not have much practical use when comparing with frequency-domain experimental results since distributions for particular chlorophylls in the structure, not particular wavelengths have been calculated, and absorption wavelengths of same chlorophylls vary from complex to complex. From the latter perspective, the low temperature distributions of energy transfer times for particular ***wavelengths*** have more significant practical use.

4.2. Simulations of EET rate (homogeneous line width) distributions

The objective of this thesis is to obtain preliminary data on the qualitative and quantitative characteristics of the realistic wavelength dependences of the parameters of excited state lifetime (energy transfer time) distributions in simple model systems which can be probed by spectral hole modeling. A necessary preparation stage before advancing

to calculations on real, far more complicated systems, like PS I, is to perform a detailed treatment of the simple models.

To understand what can be expected from the distributions of homogeneous line widths in photosynthetic complexes at low temperatures, one might begin from the very simplest model involving two pigments with uncorrelated site distribution functions (SDF). One may also assume the relative weakness of electrostatic inter-pigment interactions (i.e. that EET is dominated by the Förster mechanism [88]). The applicability of such assumption is limited as discussed above. As an example, [103] expresses EET rate via parameters of single-molecule spectra :

$$k_{ET} = \Gamma_{\text{hom}} = \frac{2\pi V^2}{\hbar} \int E_D(E) A_A(E) dE \qquad (4.7)$$

where E_D and A_A are single-site donor emission and acceptor absorption spectra, including various vibronic contributions, normalized to unity on the energy scale and interaction energy V is in the units of circular frequency. The integral in the equation is the spectral overlap integral. Equation 5.7 shows that, the inter-pigment interaction energies, as well as the EET rates are dictated by the overlaps between donor emission and acceptor absorption spectra. Thus, any model that can make quantitative predictions regarding EET rates must include proper treatment of such overlaps. As mentioned above, in the simplest cases this problem was solved analytically by Kolaczkowski et al. [99], but some of the approximations made in [99] are actually invalid at low temperatures where single molecule spectroscopy and SHB experiments are normally performed. Further, for the sake of simplicity, Kolaczkowski et al. considered Gaussian distributions of either localized or delocalized phonons. These are not good reflections of the phonon-sidebands in the single-site spectra. The parameters of electron-phonon and electron-[intra-molecular

vibration] coupling (phonon sideband shape, frequencies and Huang-Rhys factors of intra-molecular vibrations) are now sufficiently well known from SHB [63, 104] and Fluorescence Line Narrowing experiments [105,106], and one can synthesize single site spectra and calculate relevant spectral overlaps numerically.

If the excitation wavelength is set somewhere within the energy range of the donor SDF (site distribution function, probability distribution of energies of purely electronic transition), and if both donor and acceptor SDF are Gaussian, the distribution of the energy gaps between donor emission zero-phonon line (ZPL) and acceptor absorption ZPLs must also be Gaussian. Therefore, to calculate the distribution of the energy transfer times, one must determine the dependence of the spectral overlap integral on the gap between donor and acceptor ZPL. The spectral overlap integral's dependence of the donor-acceptor energy gap is:

$$J(\omega_{ZPL,D} - \omega_{ZPL,A}) = \int E_D(\omega_{ZPL,D} - \omega) A_A(\omega_{ZPL,A} - \omega) d\omega \qquad (4.8)$$

Analytically, the single site absorption profile $A_A(\omega_{ZPL,A}\ \omega)$ is described by Equation 2.8 from Chapter 2. The single-site emission profile is a mirror image of the respective absorption single-site profile with respect to the ZPL.

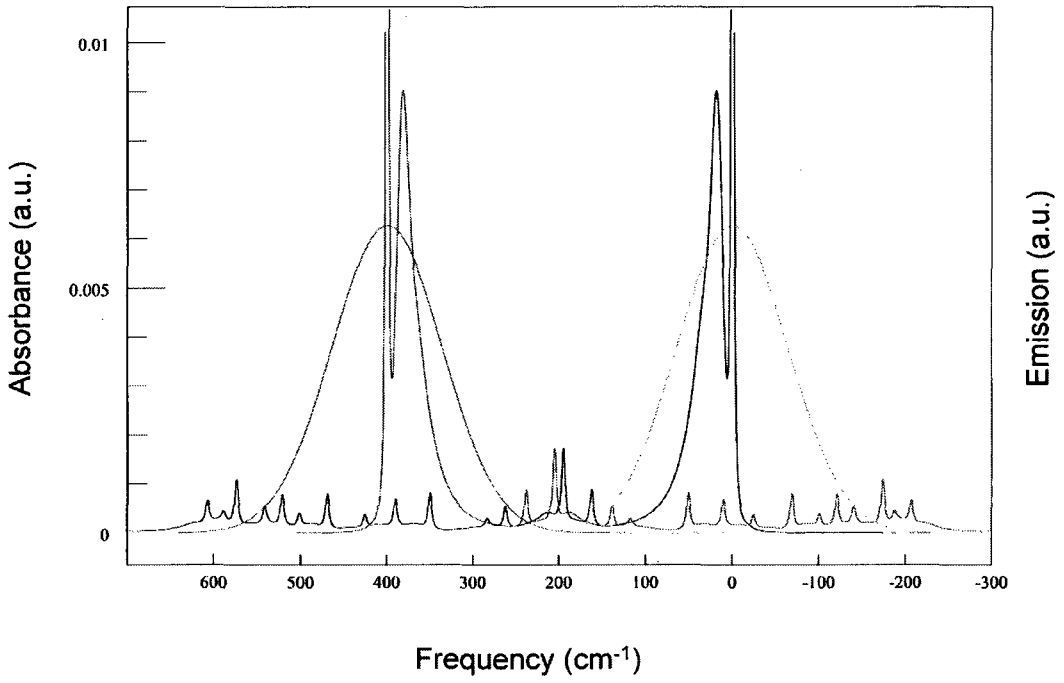

Figure 4.3 donor emission (blue) and acceptor absorption (black) spectra calculated numerically using HB simulator program, as well as respective site distribution functions of donor (red) and acceptor (green) pigments.

Figure 4.3 depicts these single site spectra as well as SDFs of donor and acceptor molecules. In this case, we employed electron-phonon coupling parameters of the A and B bands of CP43 core antenna complex of PS II. 1 cm^{-1} is used for the ZPL width of the purely electronic transition, and 4 cm^{-1} is used for the width of the zero-phonon component of the vibronic replicas. (It is mainly the shape of the phonon and vibration sidebands which determines the spectral overlap, and the knowledge of ZPL width (which cannot be determined before the EET rates are obtained, unless the ZPL of two pigments connected by energy transfer are almost iso-energetic in a given complex) is not critically significant. Note that complexes where donor and acceptor ZPL are isoenergetic contribute to the

fastest end of the EET rate distribution, which is not probed by SHB). We used the frequencies and Huang-Rhys factors of the Chl *a* intra-molecular modes as determined by Gillie et al by applying SHB to plant Photosystem I particles [104]. Zucchelli et al [107] demonstrated that the S factors received via SHB allow for a much better fit for the absorption spectra of Chl *a* in various solvents, than factors determined via FLN . Zucchelli et al further noticed that while the sum of the S-factors by Gillie et al is evidently close to correct one, some of the individual S-factors may have important differences which may be explained by inaccuracies in the experimental and data analysis procedures employed by Gillie et al. For example, HB action spectrum [91] and not the absorption spectrum should be used to rescale the areas of pseudo-vibronic holes (recently demonstrated for Bchl *a* by Tibe et al. [63]). It may not have been known to Gillie et al, but it is now well known to us that there are important differences between the shapes of the HB action and absorption spectra of PS I. Very recently, [109] the SHB and FLN S-factors were almost reconciled (both exhibiting magnitudes previously observed only in SHB).

Table 4.1: Simulation parameters for overlap function generation and for subsequent data fitting (CP43 [72])

CP43 [JL; 2000]	SDF peak and width (cm^{-1})	ω_B (cm^{-1})	S_{PSB}	ω_{ni}; Γ_{Gauss}; $\Gamma_{Lorentz}$ (cm^{-1})	λ_0	σ_λ
A	14643; 180	14705	0.30±0.05	17; 11; 70	11±0.1	1.0±0.1
B	14643, 65	14705	0.30±0.05	24, 15, 70	10.5±0.3	1.0±0.1

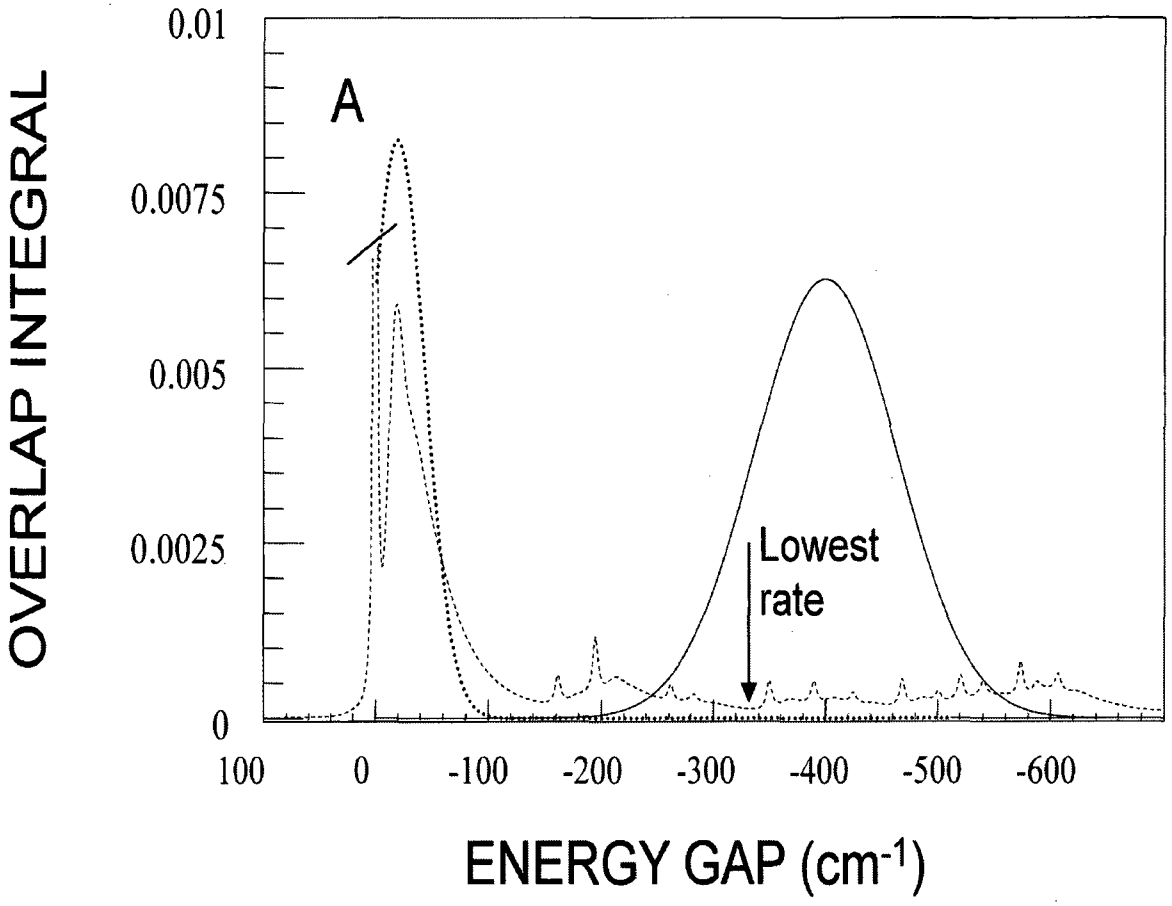

Figure 4.4 Overlap integral calculated numerically (dashed curve), acceptor SDF (solid curve) and the overlap integral according to Kolaczkowski et al (dotted surve).

Dashed curve in Figure 4.4 is the gap dependence of the overlap integral calculated numerically, and the solid curve is the distribution function for the gap between excitation energy and the center of the acceptor SDF. (ZPL-ZPL part of the overlap function is cut.) Dotted curve is the gap dependence of the overlap in Kolaczkowski approximation for delocalized phonons, e.g. the term in square brackets in the rate equation from [72]:

$$\Gamma_{hom} \sim k_{DA}(\omega_{D,ZPL} - \omega_{A,ZPL}) =$$

$$= 2\pi V^2 \left[(1 - e^S) \frac{1}{\sqrt{2\pi S(\sigma^2 + \omega_m{}^2)}} \exp \frac{-(\omega_{D,ZPL} - \omega_{A,ZPL} - S\omega_m)^2}{2S(\sigma^2 + \omega_m{}^2)} \right] \qquad (4.10)$$

The purely Gaussian phonon-sideband (dotted curve) had the same mean (not maximum) ω_m and width as half-Gaussian / half-Lorentzian one-phonon profiles employed in subsequent simulations, dashed curve. σ and S are the standard deviation (FWHM/ 2.354) and Huang-Rhys factor for the phonon sideband. It can easily be seen that at low temperatures Eq. 4.10 causes overestimation of the overlap integral for small donor-acceptor gaps and strong underestimation of that integral for large gaps. One can begin with the same logic as employed in [99], and obtain a much more accurate analytical expression for the low-temperature value of EET rate. Setting T=0 in the equations from [99] leading to above equation 4.10, one can come up with

$$k_{DA}(\omega_{D,ZPL} - \omega_{A,ZPL}) = 2\pi V^2 \left[e^S \sum_r \frac{S^r}{r!} \frac{1}{\sqrt{2\pi r\sigma^2}} \exp \frac{-(\omega_{D,ZPL} - \omega_{A,ZPL} - r\omega_m)^2}{2r\sigma^2} \right] \qquad (4.11)$$

where r refers to 0, 1, 2…-phonon processes. Note that this equation still does not take into account the intra-molecular vibration modes of chlorophyll.

Returning to the dashed curve, calculated taking into consideration contributions from both delocalized phonons and localized vibrations, it can be seen that for a large enough average donor-acceptor gap (≥150 cm^{-1}) the EET rate is determined by the intra-molecular modes, and must be subject to distribution. Further note that there is a certain

minimal rate (larger than zero) which is determined by two- and three-phonon processes (vertical arrow). That being said, the situation described so far is still much different from the case of CP43, where the two lowest-energy states are quasi-degenerate. While the gap between donor and acceptor SDF decreases, a fraction of the "donor on average" pigments become the lowest-energy pigments in our two-pigment system, and certain fraction of the "acceptor on average" pigments become capable of downhill EET. In the insert of Figure 4.5 solid curves represent the original SDF of acceptor (1) and donor (2) pigments.

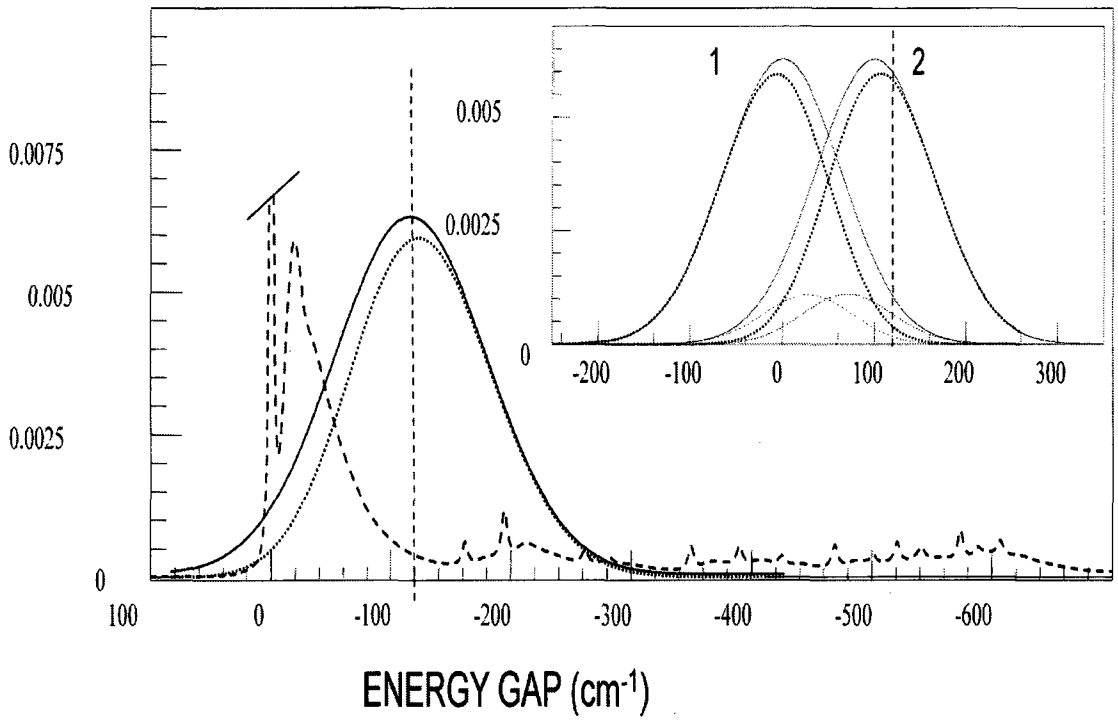

Figure 4.5 Main frame: spectral overlap function (dashed line, the ZPL-ZPL part is cut) as well as whole acceptor SDF (solid line) and part of that SDF which corresponds to acceptor pigments which are, indeed, the lowest-energy pigment molecules of the complex. The insert depicts donor and acceptor SDFs (solid lines labeled by 2 and 1, respectively) as well as the fractional SDFs of the pigments capable and incapable of energy transfer.

Dash-dotted curve represent the SDF of a fraction of pigment (2), "donor on average", becoming incapable of downhill EET. Dashed curve represents the SDF of a fraction of pigment (1) "acceptor on average", becoming capable of downhill EET. Dotted curves are corrected SDFs of pigments (1) and (2), still functioning as acceptor and donor respectively [73] demonstrates deriving these curves. It should be noted that, due to a much narrower gap between dashed and dash-dotted curves, the dashed→ dash-dotted EET may have (on average) higher rate than 2→1 rate (on average). Further note that dashed → dash-dotted EET is always downhill, no more corrections as above need be taken. Each ensemble of pigments is essentially separated into two sub-ensembles.

While correcting the overlap integral distribution in the two-pigment case one would do well to keep in mind that the correction to the original SDFs depends only on the parameters of the SDFs and not on the excitation energy. Dashed vertical lines in both main frame and insert of Figure 4.5 demonstrates the excitation energy which is shifted in relation to the peak of the donor SDF. Particularly in Figure 4.5 the gap between donor and acceptor SDF is 100 cm^{-1}, while the gap between the excitation energy and the center of the original acceptor SDF is 120 cm^{-1}. The latter gap must be used to calculate the (portion of) distribution of overlap integral values (described above). One must then calculate another part of the distribution, using the gap between the excitation energy and the parameters of the dash-dotted curve. Such contributions to the final distribution need to be weighted according to the magnitudes of dotted and dashed curves at the excitation energy and added together. It should also be taken into account that there may be contributions at the

excitation wavelength of both pigments being the lowest energy pigments in the particular two-pigment system. Therefore, EET rate for these contributions is zero, and the homogeneous line width is determined by the fluorescence lifetime (and/or pure dephasing [110] if T>0). The size of such contributions depends on the excitation energy and on SDF parameters. For example, in the case of the 200 cm^{-1} gap between donor and acceptor SDF and excitation at the peak of donor SDF (see previous paragraph), zero-EET-rate fraction is only 0.4%. In the case illustrated in Figure 4.5, this fraction goes up to 8%. For identical isoenergetic donor and acceptor and burning at the peak of the SDFs it is 50%. It should be noted that this fraction does not depend on the shape of the gap dependence of the overlap integral but solely on the SDF parameters and excitation energy. Such results, in terms of spectral hole burning, mean that a hole can be burned with the lifetime-limited width (at T=0) and with the fractional depth of several percent (e.g. easily observable) even at the energies which are much higher than the center of the lowest-energy pigment SDF, even if the electrostatic interaction between the pigments is appreciable. This is due to the SDFs of different pigments being uncorrelated. Therefore, ability to burn some shallow lifetime-limited holes cannot be treated as an evidence of weak inter-pigment interactions or of pigments being well-separated (spatially) from each other as was done in [72] for CP43. Such possibility was recently suggested in [111] but, in that case, spectral overlaps were not taken into account.

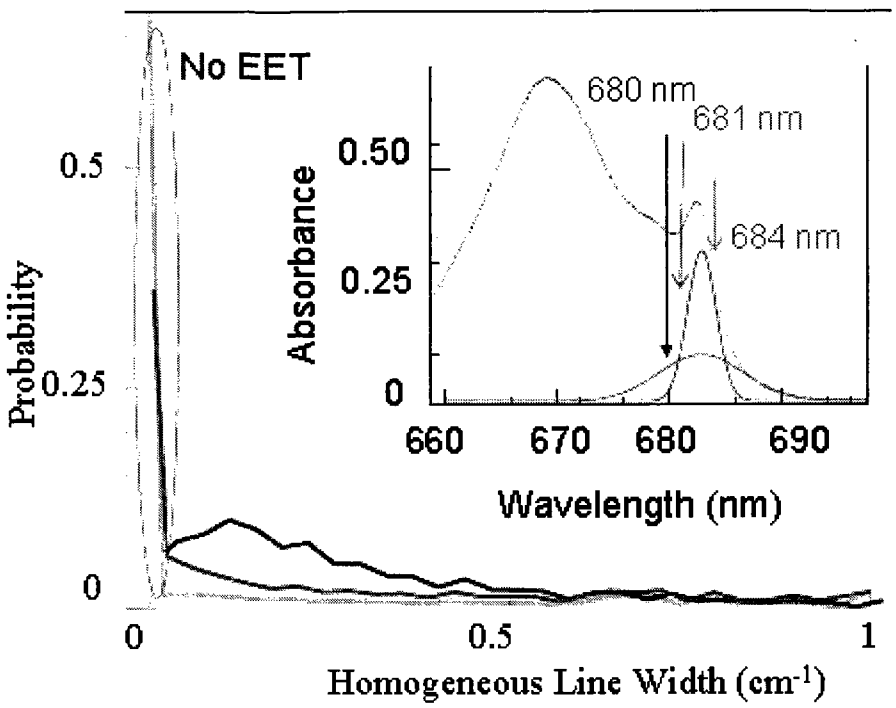

Figure 4.6. Theoretical homogeneous line width distributions calculated for V_{DA}=7.6 cm^{-1} at various wavelengths for the case of burning into two SDFs, both peaked at 683 nm, one 180 cm^{-1} wide and another 65 cm^{-1} wide. The insert contains the absorption spectrum of CP43 complex as well as the SDFs of the states A and B.

Theoretical line width distributions were calculated for different burn wavelengths assuming the presence of two bands, both peaked at 683 nm, one 65 cm^{-1} wide (B), another 180 cm^{-1} wide (A). We used 7.6 cm^{-1} inter-pigment coupling, corresponding to Chls 37/44. (After the distributions were generated by MathCad, the HB simulator was used to model the HGK for both bands.) The calculated line width distributions are demonstrated in Figure 4.6 (with pure dephasing not yet taken into account). It should be noted that owing to the quadratic dependence of the homogenous line width (or EET rate) on inter-pigment

coupling V, Eq. 4.7, the scaling of the horizontal axis has extreme sensitivity to V. Increasing V by a factor of 2 would shift the peak of the distribution by a factor of 4 to 0.5 cm^{-1}, and will increase the fraction of the molecules demonstrating very high EET rates (beyond right limit of the Figure 4.6) not effectively probed by hole burning. All distributions are clearly asymmetric and contain some fraction for which EET rate is zero. The non-zero part of the distribution for 680 nm (burning on the blue side of both bands) is broad (the width/peak ratio is large, comparable to those reported in the previous Chapter for Gaussian line width distributions). Also note that the peak of this distribution is significantly larger than the dephasing-limited width of of ~1GHz. Therefore, one would expect the line width distribution to have noticeable effect on the hole evolution, especially if burning is performed at the blue side of the SDF(s).

4.3 Experiment and fitting: CP43

4.3.1 Absorption spectra and Chlorophyll assignments of CP43

Along with the CP47, CP43 is one of the core antenna complexes of Photosystem II, responsible for both energy transfer and light-harvesting to the reaction center. Recent structure data suggests that *CP43* contains 13 chlorophyll *a* (Chl *a*) molecules (see Figure (4.7)

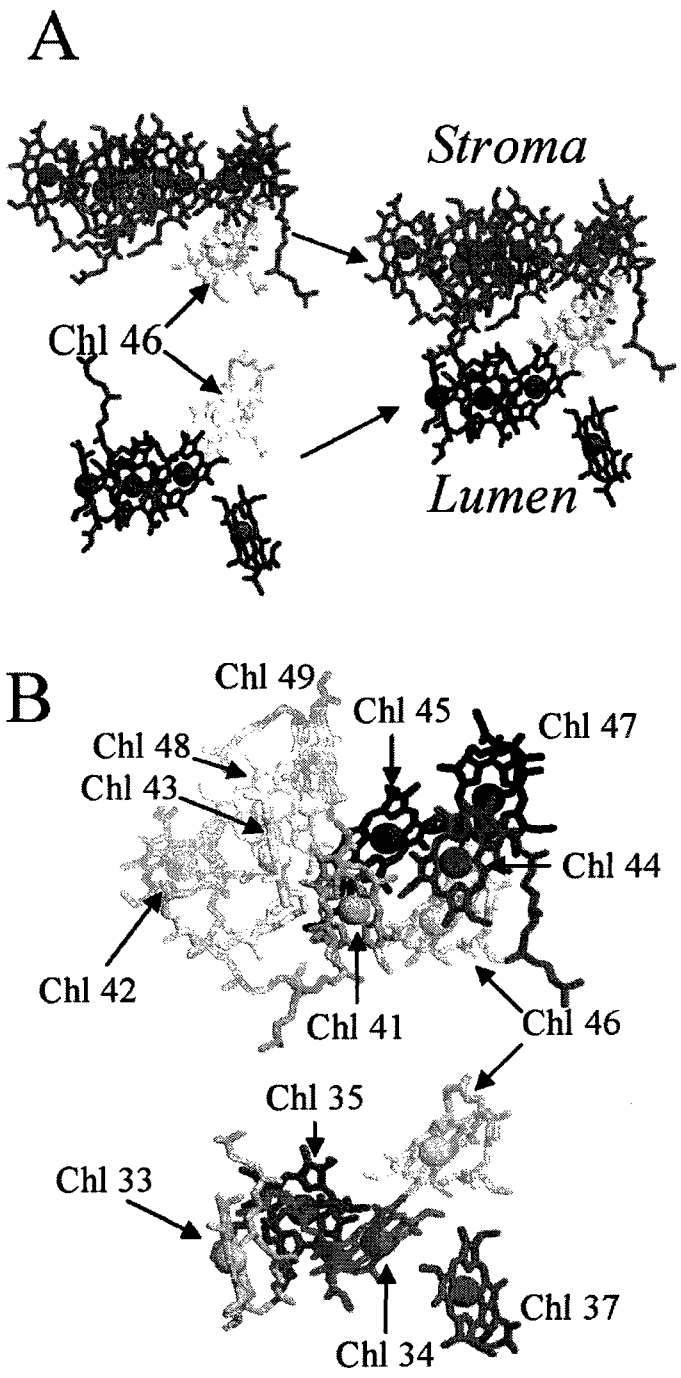

Figure 4.7. The Chls of the CP43 antenna protein. *Frame A*: Chls on the stromal side of the membrane are colored red, Chl 46 (which lies in the middle of the membrane) is colored pink, and lumenal Chls are colored blue. *Frame B*: CP43 chlorophylls separated into stromal and lumenal groupings and labeled according to Loll et al [8]. Note that Chl 46 is shown twice for clarity. From [112]

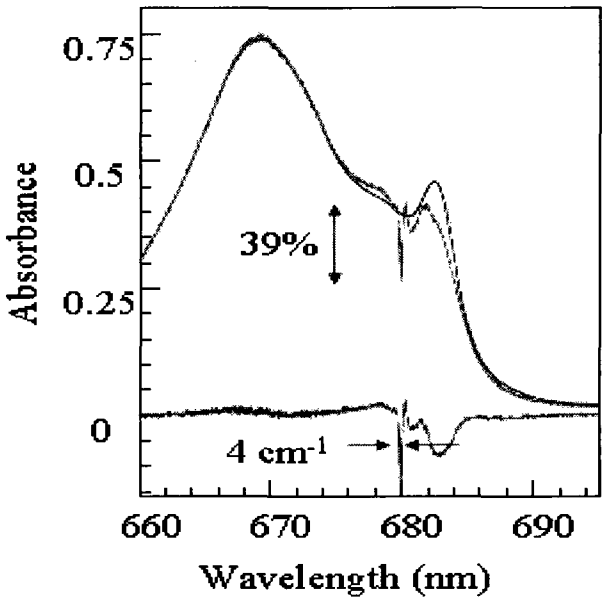

Figure 4.8: Absorption spectra of CP43 at 5 K and the hole burnt at 680 nm with 500 J/cm^2

Figure 4.8 shows absorption spectra of the purified CP43 complex that were recorded with a Varian Cary 5000 spectrophotometer with 0.05-nm resolution, before and after hole burning at 680 nm. The 5 K Q*y*-absorption spectrum of CP43 is very similar to that of Groot et al. [113] with sharper band at 682.6 nm, and broader peak at 670 nm. The ZPH is 39% deep, has a width of ~4 cm^{-1} and is accompanied by real and pseudo-PSB as well as a broad 683 nm hole due to burning following the downhill energy transfer from 680 nm to 683 nm chlorophylls.

It has been accepted that CP43 possesses two quasi degenerate lowest-energy states (*A* and *B* in the notation of Jankowiak et al. [72]), one of which (*state B*) has an unusually narrow inhomogeneous bandwidth. The exact origin of bands *A* and *B* is unclear. Early

excitonic calculations suggested that broader band *A* may belong to the group of strongly coupled chlorophylls, but such calculations were not able to reproduce narrow band B. State B is believed by some to owe its peak position and narrow bandwidth to the unusual protein environment of the respective chlorophyll(s). The absorption spectrum of CP43 along with the SDFs of A and B states is shown in Figure 4.9. (Explanation for B' and B" bands will be given later.)

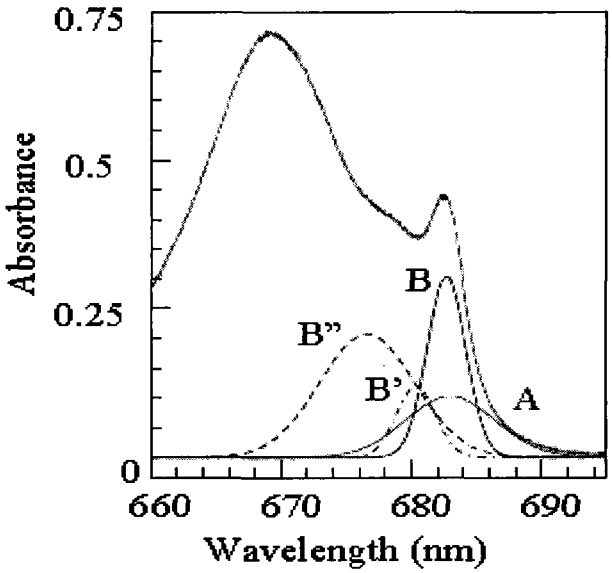

Figure 4.9. Absorption spectrum of CP43 at 5K and SDFs of A and B states. B' and B" bands are upper excitonic components of B according to Hughes et al [114].

It is not exactly known yet if chlorophylls responsible for the A and B bands are connected by fast energy transfer or how far they are located within the CP43 complex. Based on the ability to burn dephasing-limited holes anywhere within the wavelength range corresponding to the A and B bands, Jankowiak et al. [72] suggested that EET between the

two states is very slow and these pigments are situated on opposite sides of the complex. Riley et al [108] recently demonstrated that the CP43' complex of PS I grown under iron stress conditions (homologous to the CP43 of PS II) also has A and B states, and the results are better explained when allowance is made for EET between these two states on a ~10 ps timescale. Consequently, in a brief communication [111] a model involving EET between quasi-degenerate states with non-correlated site distribution functions is presented, which qualitatively explains the hole burning data for both CP43 and CP43'.

Fresh evidence has been recently introduced, based on results of time-domain RT experiments, suggesting that the chlorophyll responsible for the band B is weakly coupled to the other pigments in the CP43. The CD spectra [114] indicate that narrow band B has notable rotational strength, which probably makes it incompatible to being due to a monomeric chlorophyll. Hughes et al [114] suggested that band B is the lowest excitonic state of a strongly-coupled chlorophyll ensemble, with two other states of the same ensemble peaked at ~680 and 676.5 nm (B' and B" in Figure 4.9). This suggestion was based on an analysis of the changes in the CD spectra upon non-resonant higher-energy illumination at 4 K. A further suggestion was made that band A is due to a state well-localized on a single chlorophyll. This will be referred in the subsequent discussion as A1B3 model. On the other hand, analysis of HB experiments [19] suggests that B state is more or less localized on a single Chl *a* molecule (A1B1 model).

Table 4.2 Dipole-Dipole couplings between CP43 chlorophylls (in cm^{-1}).

chl	33	34	35	37	41	42	43	44	45	46	47	48	49
33		-12.2	-6.5	-2.4	-4.4	15.6	16.6	1.8	-10.4	3.3	-2.3	-1.0	-0.06
34			-33.3	109.9	1.2	-8.6	-11.2	6.3	30.0	87.4	14.2	-7.6	-1.2
35				-26.5	-2.4	-1.4	-5.9	-6.8	-7.3	-23.2	-7.6	20.6	5.7
37					2.0	4.3	2.2	**7.6**	-1.6	33.7	3.6	-3.2	4.45
41						-19.8	-86.7	-25.8	28.9	-4.0	-1.8	3.2	-5.0
42							58.8	13.2	-26.7	12.1	5.3	-6.8	9.7
43								-11.0	69.0	-0.9	-7.6	28.0	-21.4
44									42.8	65.6	64.9	-21.6	11.6
45										-48.4	127.1	17.5	-7.1
46											-74.1	-10.5	10.8
47												-22.6	13.0
48													-81.8
49													

Couplings between the Chl *a* molecules of CP43, calculated in dipole-dipole approximation, are presented in Table 4.2. The 7.6 cm^{-1} coupling, highlighted in red in the table, corresponds to interaction between Chls 37 and 44, which are responsible for states B and A, respectively, according to [112]. Half the table is not filled as the numbers there are symmetrical to existing numbers with respect to the diagonal.

Chapter 5

HOLE BURNING EXPERIMENTS AND FITTING

5.1 Experiments and set up

Measurements were performed in a model A240 helium bath cryostat (Ukrainian Academy of Sciences) at 5 K. Samples were diluted with glycerol 1:2 and placed in an Eppendorf Uvette featuring orthogonal optical paths of 10 mm and 2 mm. Use of Uvette allowed absorbance (moderate OD) and fluorescence excitation (small OD to avoid reabsorption effects) measurements with the same sample. The material of the Uvette does not exhibit noticeable birefringence, justifying its use in measurements involving polarized light. Quality of the samples was confirmed by measuring their absorption spectra with Varian Cary 5000 spectrophotometer at resolution of 0.5 nm. High-resolution SHB experiments were performed with Spectra-Physics/ Sirah Matisse-DS tunable dye laser (LDS688 dye) pumped with 6W 532 nm solid state laser. The Matisse-DS is actively stabilized and capable of seamless ~45 GHz scans even with passive stabilization. In case broader range had to be scanned at high resolution, the spectra were stitched together manually. High-resolution spectra and hole growth kinetics curves were detected in fluorescence excitation mode with Hamamatsu photon counter (with AELP-730 interference long-pass filter, Omega, and some neutral-density and conventional long-pass filters, LOMO), positioned at 90^{o} with respect to excitation beam. Polarization plane rotator was used to rotate horizontally polarized light emitted by the laser by 90^{0} in order to achieve situation when, given the geometry of the experiment, fluorescence from

preferentially excited molecules was effectively detected. Excitation intensity was stabilized by laser beam power stabilizer (BEOC) and adjusted with neutral density filters (ThorLabs). Some hole-burning experiments on CP43 were performed employing detection with Cary 5000 at the resolution of 0.05 nm (~1 cm^{-1}). Between the burns at different wavelengths the holes were erased by heating the samples up to ~150 K. Thus, possible mutual interference of different holes was excluded. The optical setups employed in fluorescence excitation and absorption modes, respectively, are shown in Figures 5.1 and 5.2.

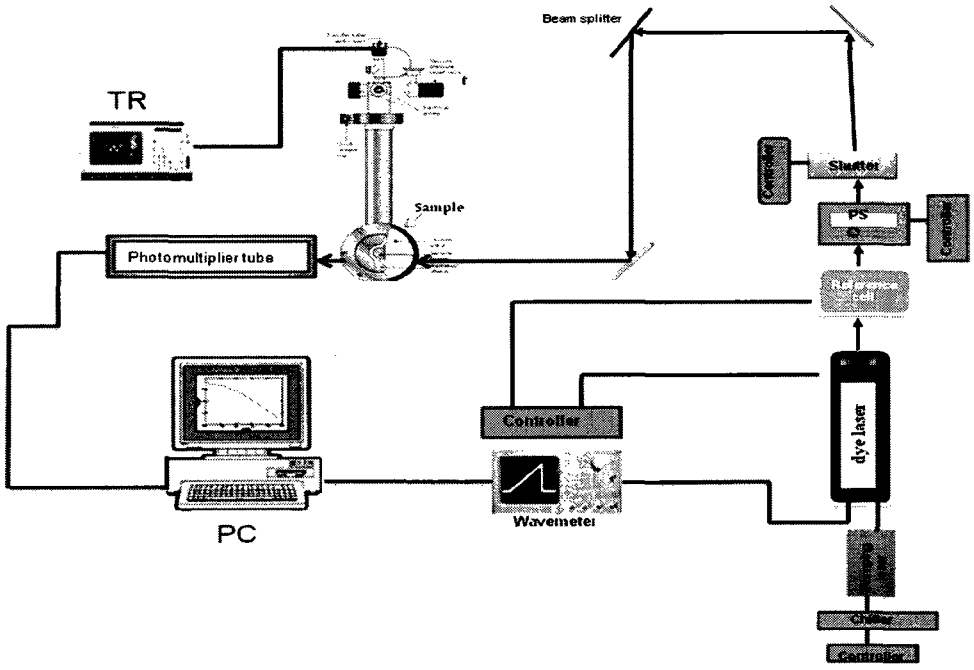

Figure 5.1. The experimental setup employed when measurements were performed in the fluorescence excitation mode.

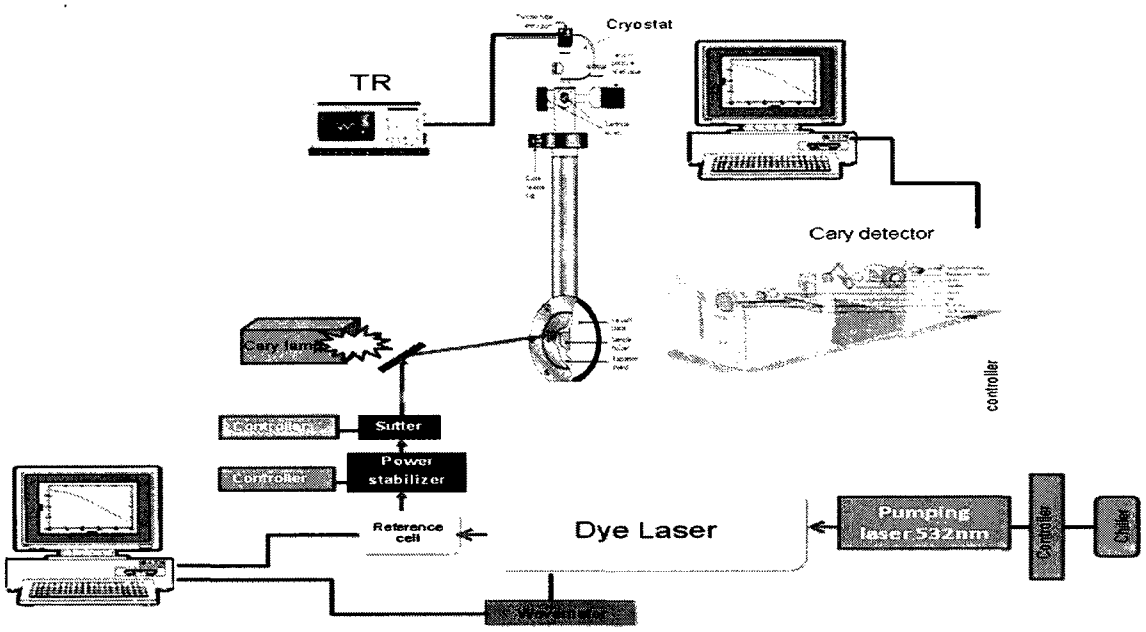

Figure 5.2. Experimental setup in absorption mode.

Figures 5.3 and 5.4 (Frames C) show spectral holes burnt at 680.15 nm in fluorescence excitation mode. The light intensity for burning was 46.8 $\mu W/cm^2$, the intensity for reading the spectra was 1000 times smaller (to prevent additional burning). Integrated cross-section of a Chl *a* molecule with transition dipole parallel to laser polarization was assumed to be $4.5 \cdot 10^{-13} cm^2 cm^{-1}$. The signal (fluorescence excitation) at burn wavelength was ~160,000 cps. Thus, the deepest holes depicted in Figures 5.3 and 5.4 are ~35% deep.

One should note that at this wavelength the absorption is not fully accounted for by A and B bands alone. Only 40% of absorption belong to the A and B bands for which we created distributions above. In A1B3 model of Krausz group [114], the rest of the

absorption at 680.15 nm belongs to the upper components of the B manifold (B' and B" in Figure 4.9). Therefore, EET from these components to the B band is very fast and the respective HB yield is very low. In the first approximation we ignore it and argue that only 40% of absorption is burnable. Thus, if, for example, the deepest experimental spectra exhibit 35% hole, this means that 87% of the burnable fraction has actually burnt. Consequently, the 35% deep experimental holes have to be compared to 87% deep theoretical holes. One has to choose 87% hole from the set which was calculated, superimpose it onto the deepest experimental hole, note by how much it had to be multiplied to do that, and then multiply other, smaller theoretical holes from that set by the same coefficient. And see if they match as well.

In A1B1 model we assume that there is no third excitonic component of B. We still acknowledge there is some small and narrow band at 680 nm, in agreement with CD results [114]. Thus, we assume that the little narrow band at 680 nm is the ONLY upper component of B. Again, using the logic from the previous paragraph – this band does not burn because it transfers energy to the lowest B-state at 683 nm. The 680 nm B' band seems to give ~25% of absorption at 680.15 nm. Thus, if the deepest experimental hole is 35% again, it means that 47% of the potentially burnable absorption is burnt. One is supposed to choose a 47%-deep hole from the calculated dataset, superimpose it on the deepest experimental hole, note by what number one had to multiply it to superimpose it, and multiply smaller calculated holes by the same number. And then look if the smaller holes match as well.

Figure 5.3 contains experimental and theoretical spectral holes produced at 680.15 nm. Multiple irradiation doses have been employed both in calculations and in

experiments. The simulated spectra have been obtained for homogeneous line width distribution based on inter-pigment coupling energy of 11 cm^{-1}. All other parameters are reported in Table 4.3.

Table 5.1 A/B Simulation parameters of Bands A and B of CP43

Parameters(*Band A*)	Value
Inhomogenous Width:	180 cm^{-1}
SDF peak position:	14641 cm^{-1}
Relative amplitude:	1
Dephasing-Limited ZPL Width:	0.033cm^{-1}
Lambda Distribution:	Included with peak and st.dev. of 10.5 and 1
Oscillator Strength	1
Phonon Sideband - Strength:	0.3cm^{-1}
Phonon sideband - Peak Frequency:	17cm^{-1}
Phonon - Gaussian Width:	15cm^{-1}
Phonon - Lorentzian Width:	70cm^{-1}
Radiative Lifetim	3ns

Parameters(*Band B*)	Value
Inhomogenous Width:	65 cm^{-1}
SDF peak position:	14641 cm^{-1}
Relative amplitude:	1
Dephasing-Limited ZPL Width:	0.033 cm^{-1}
Lambda Distribution:	Included with peak and std. dev. of 11 and 1
Oscillator Strength:	1
Phonon Sideband - Strength:	0.3 cm^{-1}
Phonon sideband - Peak Frequency:	24 cm^{-1}
Phonon - Gaussian Width:	15 cm^{-1}
Phonon - Lorentzian Width:	70 cm^{-1}
Radiative Lifetime:	3 ns

The left part of the figure was produced assuming A1B1 model, and the right part was produced assuming the A1B3 model. It is clear that in the first case the theoretical holes are too narrow, while in the second case they are too broad to explain the experimental results. Thus, in the case of A1B3 model, the inter-pigment coupling has to be lower than 11 cm^{-1}. At the first glance, the results seem to mean that in case A1B1 model is correct, the inter-pigment coupling must be significantly larger than 11 cm^{-1}. Therefore, our results appear to

be inconsistent with assignments of [112]. In other words, either the chlorophyll assignment of the A and B states is incorrect in [112], or, alternatively, there is evidence for two upper excitonic components of B, as

discussed by Hughes et al. We return to this discussion after exploring our results in more details.

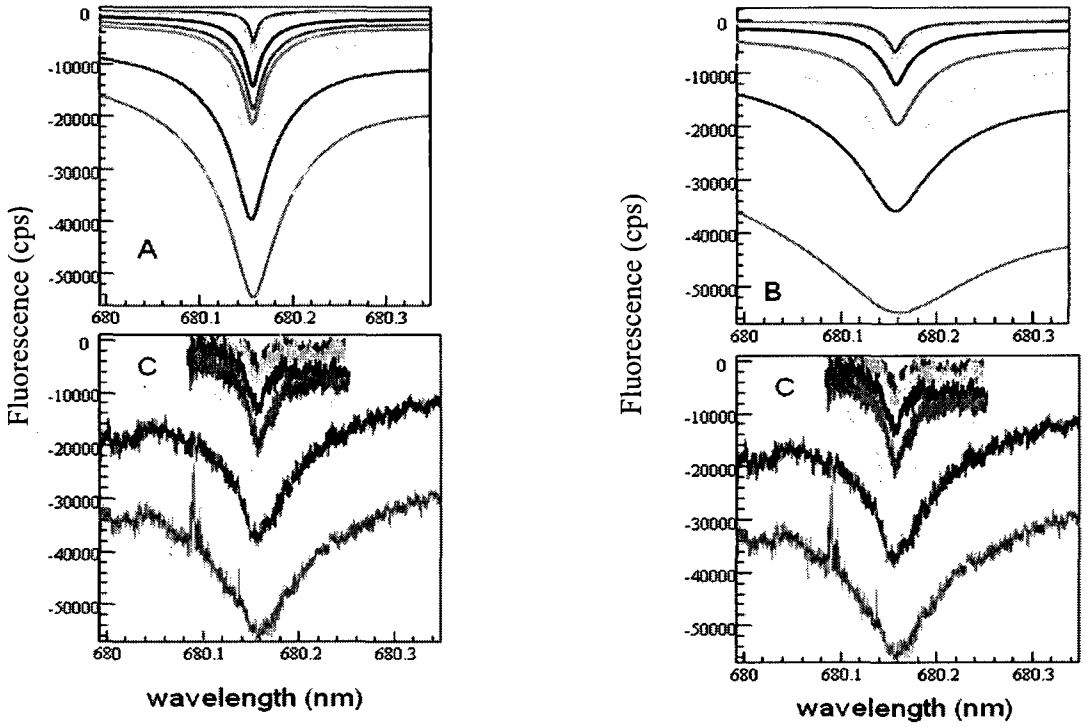

Figure 5.3 *Frame A and B*: Simulated burned holes spectrum of CP43 for A to B coupling of 11 cm^{-1} calculated using HB simulator, with A1B1 and A1B3 models, respectively. *Frame C*: The experimental holes burnt in the fluorescence excitation spectrum of CP43 of a spinach PSII core complex at 5K. Note that pre-burn absorption was ~160,000.

Next Figure 5.4, contains same experimental spectra, as well as theoretical hole spectra calculated with inter-pigment coupling of 7.6 cm^{-1}, exactly as predicted in [112]. Obviously, in case of A1B1 model the situation got worse than it was in the previous

figure. For A1B3 model, however, the fit is nearly perfect. There are several problems with the A1B3 model, though. The most important of them is that observed maximal hole width of ~40% is already incompatible with this model, if one takes into account electron-phonon coupling. The latter is S=0.3. Thus, approximately 48%, and not 40% as required by A1B3 model need to belong to potentially burnable states.

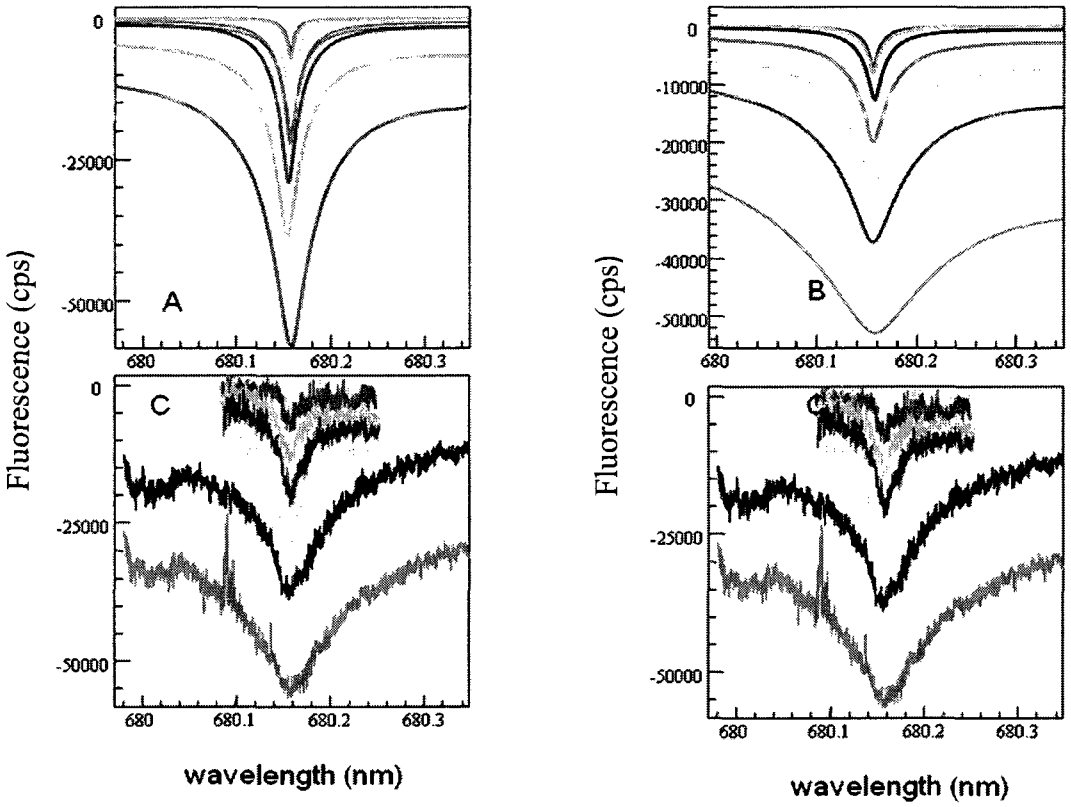

Figure 5.4 *Frames A and B*: Simulated burned hole spectrum of CP43 for inter-pigment coupling of 7.6 cm^{-1} and A1B1 model (left) and A1B3 model (right). *Frame C*: The experimental holes burnt in the fluorescence excitation spectrum of CP43 of spinach PSII core complex at 5 K.

It appears that the A1B1 model still could be used, if in this model most of the pigments other than A and B, when excited at 680 nm, will quickly transfer energy to either

A or B. Thus, even if those pigments do not represent the B", the upper excitonic component of the B-manifold, their excited state lifetime may be quite short, and the HB yield respectively low (but higher than for hypothetical B" of [112]). In other words, the behavior of the A1B1 model may not be significantly different from the behavior of the A1B3 model.

5.2 Discussion

We have demonstrated that modeling of the hole burning data in the presence of line width distributions can indeed be used to determine likely range of the inter-pigment couplings in photosynthetic complexes. Our results may still be in agreement with [112] (i..e that A is Chl 44 and B is Chl 37, see Figure 4.7 above), if one allows for relatively fast energy transfer to states A and B from other chlorophylls. In order to give a definite answer, though, our software has to be improved to allow for modeling of burning into three overlapping bands. Still, assuming lower hole burning yield for chlorophylls (other than A and B) absorbing at 680 nm, one has to require that their coupling to A and B is larger than 7.6 cm^{-1}. One could note that having two acceptors (A and B) rather than one will reduce the lifetime (and HB yield) for higher-energy pigments even if all inter-pigment couplings are the same. The rate of energy transfer out of those higher-energy pigments will be the sum of the rates of energy transfer to A and energy transfer to B. (And the distribution of line widths will be a convolution of distributions obtained for every acceptor separately.) According to [112], likely candidates for the third-lowest energy state are Chl

42 and/or Chl 45. It appears that both these chlorophylls exhibit significant coupling to Chl 44 (A), 13.2 and 42.8 cm^{-1}, respectively. Therefore the assignments of [112] still seem plausible. More work is needed to fully clarify the exact chlorophyll assignments.

Chapter 6

Conclusions

Effects of the Gaussian distributions of the excitation energy transfer rates (homogenous) line widths on the evolution of the spectral holes have been explored. It has been demonstrated that one can determine the parameters of the tunneling distribution just from the slope of the hole width dependence on dose, and it will not be very sensitive to the presence or absence of the line width distribution. Thus, protein dynamics can be disentangled from the line width distributions. Unfortunately, the reverse is not true. Without any additional independent knowledge, the homogeneous line width distributions cannot be extracted so easily. However, if the mean of the line width distribution is determined by independent measurements (from time-domain experiments, which are not preferentially sensitive to the longest EET times), one can determine the width of thedistribution by fitting the hole width dependence on the hole depth. The analysis of the whole hole shape evolution probably can be helpful in disentangling the effects of the lambda distribution and the line width distribution, but the procedure for that is not yet developed. More work needs to be done along these lines.

Theoretical distributions of EET rates and their wavelength dependence have been obtained in the case of Förster-type energy transfer between the donor and acceptor molecules. These distributions have been employed to fit the experimental hole spectra for CP43 core antenna complexes of Photosystem I. It has been demonstrated that the analysis of the hole evolution allows one to distinguish between different line width distributions, to

determine respective range of reasonable inter-pigment couplings and therefore to make, support or reject various assumptions about the correspondence between different chlorophyll molecules in the structure and various spectral bands.

Bibliography

[1] Blankenship, R. Molecular Mechanisms of Photosynthesis; Blackwell Science:Oxford, England, 2002.

[2] Kamen, M. D., Bartsch, R. G., Horio, T., and de Klerk, H., in Methods in Enzymology (edit. by Colowick, S. P., and Kaplan, N. O.), 6, 391 (Academic Press, New York, 1963).

[3] Danks, S. M.; Evans, E. H.; Whittaker, P. A. In Photosynthetic Systems: Structure, Function and Assembly; John Wiley and Sons: New York, 1983.

[4] Govindjee and R. Govindjee (1975) Introduction to Photosynthesis, In: Bioenergetics of Photosynthesis, (ed. Govindjee) Academic Press, NY, pp. 1-50

[5] Campbell, N.A. and Reece, J.B., Biology, 6th Ed; Benjamin Cummings, California,2001.

[6] Ben-Shem, A., F. Frolow, and N. Nelson. 2003. Nature. 426:630–635.

[7] Deisenhofer J., Michel, H., 1989, Science,. 245. pp. 1463 – 1473

[8] Loll, B., Kern, J., Zouni, A., Saenger, W., Biesiadka, J., Irrgang, K.-D., Photosynth. Res. 2005, 86, 175.

[9] K. N. Ferreira, T. M. Iverson, K. Maghlaoui, J. Barber, S. Iwata; Science (2004)303; pp. 1831-1838

[10] Shen, J.-R. & Kamiya, N. (2000) Biochemistry 39, 14739–14744.

[11] Guskov A., Kern J., Gabdulkhakov A., Broser M., Zouni, A., Saenger, W. 2009 Nature Struct. Mol. Biol. 16, 334-342.

[12] van Amerongen, H., and R. van Grondelle. 2001. J. Phys. Chem. B. 105:604–617.

[13] Pascal, A. A., Z. Liu, K. Broess, B. van Oort, H. van Amerongen, C. Wang, P. Horton, B. Robert, W. Chang, and A. Ruban. 2005. Nature. 436:134–137.

[14] J. R. Durrant, D. R. Klug, S. L. Kwa, R. van Grondelle, G. Porter, and J. P. Dekker, Proc Natl Acad Sci U S A. 1995; 92: 4798–4802.

[15] Jordan, P., P. Fromme, H. T. Witt, O. Klukas, W. Saenger, and N. Krauss. 2001. Nature. 411:909–917.

[16] Zouni, A., Jordan, R., Schlodder, E., Fromme, P. & Witt, H. T. (2000) Biochim.Biophys. Acta 1457, 103–105.

[17] Nelson, N., and A. Ben-Shem. 2004. Nat. Rev. Mol. Cell Biol. 5:971–982.

[18] Zouni, A., Witt, H. T., Kern, J., Fromme, P., Krauss, N., Saenger, W. & Orth, P. (2001) Nature 409, 739–743.

[19] Barber, J. (2002) Curr. Opin. Struct. Biol. 12, 523–530.

[20] M. K. Şener, C. Jolley, A. Ben-Shem, P. Fromme, N. Nelson, R. Croce, and K. Schulten. *Biophysical Journal*, 89:1630-1642. 2005

[21] Ganeteg, U., F. Klimmek, and S. Jansson. 2004. Plant Mol. Bio. 54:641–651.

[22] Hall, D.O. and Rao, K.K., Photosynthesis, 6th ed.; Cambridge University: Cambridge, England, 1999.

[23] Photovoltaic and Photoactive Materials - Properties, Technology and Applications, Nunzi, J.-M., Marshall, J.M. and Dimova-Malinovska, D., Eds.; Kluwer Academic: Dordrecht, The Netherlands, 2002;.

[24] Kodis, G., Liddell, P. A., de la Garza, L., Clausen, P. C., Lindsey, J. S., Moore, A. L., Moore, T. A.; Gust, D., J. Phys. Chem. A. 2002, 106, p. 2036.

[25] Gust, D., Moore, T. A., Moore, A. L., Kennis, J. T. M., J. Phys. Chem. B. 2004, 108, p. 414.

[26] Lee, J. W. Lee, E. Greenbaum, Phys. Rev. Lett. 1999, 79, p. 3294.

[27] R. Das, P. J. Kiley, M. Segal, J. Norville, A. A. Yu, L. Wang, S. A. Trammell, L. E. Reddick, R. Kumar, F. Stellacci, N. Lebedev, J. Schnur, B. D. Bruce, S. Zhang, M. Baldo, Nano Lett. 2004, 4, p. 1079.

[28] Moerner, W. E., Ed., In *Topics in Current Physics, Persistent Spectral HoleBurning: Science and Applications*; Springer-Verlag: New York, 1988.

[29] Jankowiak, R; Hayes, J. M; Small, G. J. *Chem.Rev. 1993, 93, 1471.*

[30] Jankowiak, R.; Small, G. J. in The Photosynthetic Reaction Center, Vol2, Deisenhofer, J.; Norris, J. Eds.; *Academic Press: New York, 1993*, p.133.

[31] Reddy, N. R. S.; Lyle, P. A.; Small, G. J. *Photosyn.Res. 1992,31, 167.*

[32] Hayes, J.M., Gillie, J.K., Tang, D., Small, G.J., *Biochim, Biophys, Acta* **1988**,932, 287.

[33] Hayes, J.M., Lyle, P.A., Small, G.J., *J. Phys. Chem.* **1994**, 98, 7337.

[34] Wu. H.-M., Ratsep, M., Jankowiak, R., Cogdell, R.J., Small, G.J., *J. Phys. Chem.B*

1997, 101, 7641.

[35] Reinot, T., Zazubovich, W., Hayes, J. M. and Small, G. J. *J. Phys. Chem. B***2001**,105, -5083.

[36] Jankowiak, R., Hayes, J.M., Small, G.J., *Chem. Rev.***1993**, 93, 1471.

[37] S. Volker, *Photosynth Res* 101:245–266, 2009

[38] Levine, Ira N. *Quantum Chemistry,* 5th ed.; Prentice Hall: New Jersey, 2000; p.96-97.

[39] Ingle, J.D. and Crouch, S.R., *Spectrochemical Analysis*; Prentice-Hall: New Jersey, 1988; p. 209.

[40] Jankowiak, R., In *Shpol'skii* , Gooijer, C., Ariese, F. and Hofstraat, J. W., Eds.; John Wiley & Sons: New York, 2000; p. 235.

[41] Jankowiak, R., Richert, R., Bässler, H., *J. Phys. Chem.* **1985**, 89, 4569-4574.

[42] Koedijk, J. M. A., Wannemacher, R., Silbey, R. J. and Völker, S., *J. Phys. Chem.* **1996**, 100, 19945.

[43] Sild, O. and Haller, K., Eds., *Zero-Phonon Lines and Spectral Hole Burning inSpectroscopy and Photochemistry*; Springer-Verlag: New York, 1988.

[44] Völker, S., In *Relaxation Processes in Molecular Excited States*, Fünfschilling, J.,Ed.; Kluwer: Dordrecht, The Netherlands, 1989; p.113.

[45] Creemers, T. M. H and Volker, S., In *Shpol'skii Spectroscopy and Other Site Selection Methods: Applications in Environmental Analysis, Bioanalytical Chemistry, and Chemical Physics*, Gooijer, C., Ariese, F. and Hofstraat, J. W.,Eds.;

John Wiley & Son: New York, 2000, Chapter 9, 273.

[46] Mukamel, S., *Principles of Nonlinear Optical Spectroscopy*, Oxford University:New York, 1995; Chapter 9 - 11, 261.

[47] Narasimhan, L. R., Littau, K. A., Pack, D. W., Bai, Y. S., Elschner, A, Fayer, M.D., *Chem. Rev.* **1990**, 90, 439.

[48] Basche, Th., Moerner, W. E., Orrit, M., Wild, U., Eds., In *Single Molecule Optical Detection, Imaging and Spectroscopy*; VCH: Weinheim, New York, 1996.

[49] Basche, Th., Orrit, M., Rigler, R., Eds., *Single Molecule Spectroscopy – Nobel Conference Lectures*; VCH: Weinheim, New York, 1996.

[50] Völker, S., MacFarlane, R. M., Genack, A. Z., Trommsdorff, H. P., and van der Waals, J. H., *J. Chem. Phys.* **1977**, 67, 1759.

[51] Hayes, J.M. and Small, G.J., *Chem. Phys.* **1978**, 21, 151.

[52] Anderson, P.W., Halperin, B.I., Varma, C.M., *Philos. Mag.* **1972**, 25, 1.

[53] Phillips, W.A., J. *Low Temp. Phys.* **1972**, 7, 351.

[54] Shu, L. and Small, G.J., *J. Opt. Soc. Am. B* **1992**, 9,724.

[55] Shu, L. and Small, G. J. *Chem. Phys.* **1990**, 141, 447.

[56] Hayes, J. M., Stout, R. P., Small, G. J. *J. Phys. Chem.* **1981**, 74, 4266.

[57] Cohen, M.H. and Grest, G.S., *Phys. Rev. Lett.* **1980**, 45, 271.

[58] Reinot, T. and Small, G.J., *J. Chem. Phys.* **2001**, 114, 9105.

[59] Friedrich, J.; Haarer,D. Angew.*Chem.Int.Ed. Engl. 1984, 23, 113.*

[60] Frauenfelder,H. et al. *J.Phys.Chem.1990, 94, 1024.*

[61] Psencki, J., Polivka, T., Nemec, P., Dian, J., Kudrna, J., Maly, P., Hala, J., *J.Phys. Chem. A* **1998**, 102, 4392.

[62] Jankowiak, R. and Small, G.J., In *Photosynthetic Reaction Centers*, Diesenhofer, J, Norris, J., Eds.; Academic Press: New York, 1993.

[63] Zazubovich, V., Tibe, I., Small, G.J., *J. Phys. Chem. B* **2001**, 105, 12410.

[64] Dick, B. *Chem. Phys.* **1989**, 136, 429.

[65] Rätsep, M., Johnson, T.W., Chitnis, P.R., Small, G.J., *J. Phys. Chem. B* **2000**,104, 836.

[66] Hsin, T.-M., Zazubovich, V., Hayes, J. M., Small, G. J. *J. Phys. Chem. B* **2004**,108, 10515.

[67] Reinot, T.; Dang, N. C.; Small, G. J, *J. Chem. Phys.* **2003**, 119, 10404.

[68] Matsuzaki, S., Zazubovich, V., Rätsep, M., Hayes, J.M., Small, G.J., *J. Phys.Chem. B* **2000**, 104, 9564.

[69] Kenney, M.J., Jankowiak, R., Small, G.J., *Chem. Phys.* **1990**, 46, 47.

[70] T. Reinot, G.J. Small, *J. Chem. Phys.* 113 (2000) 10207

[71] T. Reinot and G. J. Small, J. Chem. Phys., 114 (2001) 9105.

[72] R. Jankowiak, V. Zazubovich, M. Rätsep, S. Matsuzaki, M. Alfonso, R. Picorel, M. Seibert, and G. J. Small, *J. Phys. Chem. B* 2000, *104,* 11805-11815

[73] K. J. Riley, T. Reinot, R. Jankowiak, P. Fromme, V. Zazubovich *J. Phys. Chem. B* 2007, *111,* 286-292

[74] Zazubovich, V.; Matsuzaki, S.; Johnson, T. W.; Hayes, J. M.; Chitnis, P. R.; Small, G. J. *Chem. Phys.* 2002, *275*, 47.

[75] T. Reinot, V. Zazubovich, J. M. Hayes, G.J. Small, *J. Phys. Chem.* B 2001 105 5083.

[76] Rätsep, M.; Johnson, T. W.; Chitnis, P. R.; Small, G. J. *J. Phys. Chem. B* 2000, *104*, 836

[77] K. Riley, R. Jankowiak, M. Rätsep,G. J. Small,and V. Zazubovich, *J. Phys. Chem. B* 2004, *108,* 10346-10356.

[78] Prokhorenko, V. I.; Holzwarth, A. R. *J. Phys. Chem. B* 2000, *104*, 11563.

[79] Baier, J., Gabrielsen, M., Oellerich, S., Michel, H., van Heel, M., Cogdell, R. J., Köhler, J., *Biophys. J.* **2009**, 97, 2604.

[80] Baier, J., Richter, M. F., Cogdell, R. J., Oellerich, S., Köhler, J. *Phys. Rev. Lett.* **2008**, 100, 018108.

[81] Hofmann, C., Michel, H., van Heel, M., Köhler, J. *Phys. Rev. Lett.* 2005, 94, 195501.

[82] D. Grozdanov, N. Herascu, T. Reinot, R. Jankowiak, V. Zazubovich, *Journal of Physical Chemistry* B 114 (2010) 3426.

[83] Jang, S., Newton, M. D., Silbey, R. J., *Phys. Rev. Lett.* **2004**, 92, 218301.

[84] Scholes, G. D., Fleming, G. R., *J. Phys. Chem.* B **2000**, 104, 1854.

[85] Mukai, K., Abe, S., Sumi, H., *J. Phys. Chem.* B **1999**, 103, 6096.

[86] Sundstrom, V., Pullertis, T., van Grondelle, R., *J. Phys. Chem.* B 1999, 103, p.232.

[87] Brixner, T., Stenger, J., Vaswani, H. M., Cho, M., Blankenship, R. E., Fleming, G. R., *Nature* 2005, 434, 625.

[88] Förster, Th. *Discuss. Faraday Soc.* **1953**, *27*, 7

[89] Davydov, AS., *Theory of Molecular Excitons*; Plenum: New York, 1971.

[90] Rahman, T.S., Knox, R.S., Kenkre, V.M., Chem. Phys. 1979, 44, 197.

[91] Reddy, N.R.S., Picorel, R., Small, G. J., J. *Phys. Chem.* 1992, 96, 6458.

[92] Dexter, D.L., *J. Chem. Phys.* **1953**, 21, 836.

[93] Levine, Ira N. *Quantum Chemistry,* 5th ed.; Prentice Hall: New Jersey, 2000;96

[94] Scholes, G.D., Jordanides, X.J., Fleming, G.R., *J. Phys. Chem. B* **2001**, 105, 1640

[95] Wu. H.-M., Ph.D. Thesis, Iowa State University, 1998.

[96] Mukamel, S. *Principles of Nonlinear Optical Spectroscopy*; Oxford University Press: New York, 1995.

[97] Clegg, R.M., *Chemical Analysis* **1996**, 137, 179.

[98] Förster, Th., *Discuss. Faraday Soc.* **1959**, 27, 7.

[99] Kolaczkowski, S. V, Hayes, J. M., Small, G. J., *J. Phys. Chem*, 1994, 98, 13418.

[100] M. K. Sener, D. Lu, T. Ritz, S. Park, P. Fromme, K. Schulten, *J. Phys. Chem. B* 2002, *106,* 7948-7960.

[101] Damjanovic, A.; Vaswani, H. M.; Fromme, P.; Fleming, G. R. *J. Phys. Chem. B* 2002, *106*, 10251.

[102] Vasil'ev, S.; Orth, P.; Zouni, A.; Owens, T. G.; Bruce, D. *Proc. Natl. Acad. Sci. U.S.A.* 2001, *98*, 8602.

[103] T. Markvart, *Progress in Quantum Electronics* 24 (2000) 107, 186

[104] Gillie, J. K.; Small, G. J.; Golbeck, J. H. *J. Phys. Chem.* **1989**, *93*, 1620.

[105] Wendling, M.; Pullerits, T.; Przyjalowski, M. A.; Vulto, S. I. E.; Aartsma, T. J.; van Grondelle, R.; van Amerongen, H. *J. Phys. Chem. B* **2000**, *104*, 5825

[106] Peterman, E. J. G.; Pullerits, T.; van Grondelle, R.; van Amerongen, H. *J. Phys. Chem. B* **1997**, *101*, 4448

[107] G. Zucchelli, R. C. Jennings, F M. Garlaschi, G. Cinque, R. Bassi, O. Cremonesi *Biophys. J.* 82, 2002, 378.

[108] K. J. Riley, V. Zazubovich, R Jankowiak *J. Phys. Chem. B* 2006, *110,* 22436

[109] Rätsep, M., Pieper, J., Irrgang, K.-D., Freiberg, A., *J. Phys. Chem.* B **2008**, 112, 110.

[110] Rebane, K. K., *Impurity Spectra of Solids*, Plenum: New York, 1970.

[111] V. Zazubovich, R Jankowiak, *J. Lumin.* 127 (2007) 245.

[112] M. Reppert, V. Zazubovich, N. C. Dang, M. Seibert, R. Jankowiak, J. Phys. Chem. B 112 (2008) 9934.

[113] Groot, M.-L.; Frese, R. N.; Weerd, F. L.; Bromek, K.; Petterson,A.; Peterman, E. J. G.; van Stokkum, I. H. M.; van Grondelle, R.; Dekker,J. P. *Biophys. J.* **1999**, *77*, 3328.

[114] J. L. Hughes, R. Picorel, M. Seibert, and E. Krausz, *Biochemistry* **2006,** *45,* 12345-12357.

[115] A. N. Melkozernov, J. Barber, R. E. Blankenship, 2iochemistry, 2006, 45,331-345.